POLITECNICO DI TORINO

Master's Degree in Aerospace Engineering

Master's Degree Thesis

Analysis and simulation of nominal mission scenarios of suborbital vehicles

Supervisors

Prof. Nicole Viola
Prof. Roberta Fusaro
Ing. Oscar Gori

Candidate

Perricone Emanuela

July 2024

Abstract

In the recent years, the commercial space transportation has gained considerable attention. The inaugural suborbital launch with horizontal take-off and landing of Virgin Galactic's WhiteKnightTwo (WK2) / SpaceShipTwo (SS2)"Unity" system occurred in September 2016. Following this first flight test, a series of further tests were conducted until the first commercial suborbital launch occurred in June 2023 at Spaceport America in New Mexico (USA). This marks the advent of a new era in commercial space transportation in the context of the New Space Economy.

This thesis was conducted in collaboration with ENAC (Ente Nazionale per l'Aviazione Civile) with the aim of conducting preliminary investigations into the potential operations of future suborbital vehicles within the Italian territory. In particular, this work aims at identifying few feasible mission options from the representative environment of Grottaglie Airport, in southern Italy, during nominal conditions. Even though this thesis was conducted in collaboration with ENAC, however, it shall not be regarded as officially approved or endorsed by ENAC in any manner.

To achieve this goal, it is important to simulate the nominal situation within a proper mission analysis, characterising the aerodynamic and propulsive performance of a suborbital vehicle system. A multi-fidelity approach is adopted to allow a fast and agile assessment of these characteristics, followed by more accurate analyses.

In accordance with this rationale, a preliminary aerodynamic database is constructed, without having access to a three-dimensional computer-aided design (CAD) model of the vehicles, through the application of analytical semi-empirical models. These models, which are already available in the literature and specifically address high-speed vehicles, are compared and properly customised in order to more accurately capture the peculiarities of the specific case study. In particular, the preliminary aerodynamic model that were investigated included: a model that implemented Raymer's method; a model that implemented the Prandtl's Lifting-line Theory; the use of Digital DATCOM Software. These three models provided three outputs, which were suitably compared to each other, and finally only one of these models was adopted.

Four distinct aerodynamic databases are generated with the objective of capturing the full range of configurations of a vehicle's system, representative of the WhiteKnightTwo/SpaceShipTwo configuration: the mated configuration, where the carrier aircraft and suborbital spaceship are mechanically joined; the carrier aircraft standalone; the suborbital spaceship un-feathered; the suborbital spaceship feathered (to decelerate the aircraft during the re-entry phase).

In addition, the propulsion database for the carrier aircraft is generated using a propulsion model based on the Mattingly approach, which is specific to separate exhaust-stream turbofan engine. On the other hand, for the hybrid rocket motor of the suborbital spaceship, the data found in literature were sufficient for our simulations.

The final aerodynamics and propulsive databases capture the variation of aero-propulsive characteristics of the reference vehicles at different speeds, angles of attack and altitude conditions. These databases are then used to run multiple mission studies using the commercial software ASTOS.

In order to identify possible trajectories for the mission, it was necessary to conduct a survey of the area surrounding the airport. By studying the population density, it was possible to identify potential overland corridors for the take-off and re-entry of the suborbital vehicle system

Chapter 1

Introduction

This thesis was carried out in collaboration with ENAC (Ente Nazionale per l'Aviazione Civile) to conduct preliminary investigations into the potential operations of future suborbital vehicles within Italian territory. Previous evaluations have indicated that, with the necessary upgrades, Grottaglie Airport in Puglia is a suitable candidate for this type of mission among the existing airports in Italy.

The result of this work is the definition of a potential flight path for the A-to-A mission, which is to be performed by a suborbital aircraft departing from Grottaglie Airport.

In order to define a route and simulate it with specific instruments, it was necessary to carry out a characterisation of the area surrounding Grottaglie Airport. This included a study of the population density in this area. Furthermore, an aerodynamic and propulsive characterisation of the aircraft under consideration in this thesis was also required.

1.1 Suborbital flight

By definition, a Suborbital flight is a flight that follows the suborbital trajectory [1]. A suborbital trajectory is defined as "The intentional flight path of a vehicle or any portion thereof, whose vacuum Instantaneous Impact Point (IIP) does not leave the surface of the Earth, and that reaches high altitudes beyond the denser layer of the atmosphere, such that in a portion of it the vehicle is not able to develop sufficient aerodynamic forces to significantly affect the flight (attitude, control or flight performances) (ballistic flight)" [1].

Some suborbital flights have been conducted with the objective of testing spacecraft and launch vehicles for subsequent orbital flights. Another purpose of suborbital flight is space tourism, defined as human space travel for entertainment reasons. Tourists are interested in observing the Earth from space, experiencing microgravity, high speed and contributing to research.

Space tourism is classified as the highest level of adventure tourism, and as with other forms of adventure tourism, technology plays a pivotal role in enhancing its accessibility and quality. All suborbital tourism vehicles are designed to perform parabolic flights at apogee in order to simulate the sensation of weightlessness for passengers.

A-to-A vehicle systems, which are dedicated to suborbital space tourism, crew training or experimentation, have been successfully developed in the United States. At the present time, only concepts have been studied in Europe. Nevertheless, the recent achievements of American vehicles, such as the New Shepard suborbital space tourism vehicle developed by Blue Origin and the SpaceShipTwo spacecraft developed by Virgin Galactic, may facilitate the development of European solutions, including the adaptation of American vehicles, particularly the SpaceShipTwo, for use within the European territory.

1.2 Virgin Galactic

Virgin Galactic is a company founded by Richard Branson. Its activities include the development of commercial spacecraft and the provision of suborbital flights to space tourists. The company provides transportation services through its comparatively cheaper launching technologies, which are based on a revolutionary model, namely the company's suborbital spaceplane, such as the SpaceShipTwo, are launched by a carrier aircraft, the WhiteKnightTwo. The Virgin Galactic company offers three different categories of services:

- A suborbital flight experience for humans, which is classified as space tourism;
- Research and education: replacing astronauts' seats with racks for mounting payloads for experiments in microgravity conditions.

1.2.1 SpaceShipTwo

SpaceShipTwo was designed and constructed by Scaled Composites, LLC, with the intention of providing regular access to suborbital space for the general public. The aircraft received an experimental category Special Airworthiness Certificate. This certification was originally issued by FAA-AST on 23 July 2008 and subsequently reissued on 1 October 2014. It is an air-launched suborbital spaceplane designed for commercial space tourism purposes. [2]

SpaceShipTwo is a hybrid rocket-powered, multi-configuration vehicle constructed from composite materials and designed to accommodate eight passengers (six space flight participants and two pilots). The aircraft is configured with a low wing, twin tail booms, external horizontal tails and "extension-only" tricycle landing gear. The spaceplane is capable of generating thrust in the range of 222,411 to 378,098 kN and sustaining a burn time of approximately 60 seconds. SpaceShipTwo uses a feathered system to re-enter the Earth's atmosphere, with a higher drag configuration that allows the vehicle to slow down. This system was designed to raise a feather flap assembly from SS2's normal configuration (0°) to 60° to increase the vehicle's drag during the re-entry phase of flight. The feather system was also designed to retract the feather flap assembly at the end of the re-entry phase to aerodynamically configure SS2 for its glide to a landing. The flap assembly included the left and right tailbooms, left and right flaps, and a torque tube structure in the rear fuselage connecting the two sides of the flap assembly. The assembly was attached to the rear wing spar by two outboard and two inboard hinges (located in the wingtips and aft fuselage respectively). [2]

1.2.2 WhiteKnightTwo

The WhiteKnightTwo is a transport aircraft used to launch the SpaceShipTwo. Scaled Composites designed the aircraft. In addition to serving as the mothership for the SpaceShipTwo, the WhiteKnightTwo has been specifically designed with an 'open architecture' that allows the aircraft to be adapted for a variety of uses, including operating as a weightless aircraft to train personnel in microgravity or to carry out missions at very high altitudes.

The WhiteKnightTwo, a twin-fuselage aircraft, is propelled by four mighty Pratt and Whitney engines, each exuding a total thrust of approximately 122,7 kN. This aircraft, with a wingspan of approximately 43 m and a maximum gross take-off weight of around 1466 kg, is a testament to engineering prowess and power. [3]

1.2.3 WhiteKnightTwo and SpaceShipTwo mission profile

It is anticipated that the current Virgin Spaceplane will only be capable of suborbital flights, with no intention of reaching the Low Earth Orbit (LEO). It is, therefore, expected that the spaceplane will land at the departure spaceport. The take-off is carried out by a carrier, designated WhiteKnightTwo, to which the SpaceShipTwo is anchored on the bottom side (air-launch captive on the bottom). The carrier is capable of lifting SpaceShipTwo to an altitude of 15,200 meters. At this altitude, the spacecraft will separate from the carrier and, after a brief pause, ignite its hybrid rocket propulsion system. The ascent phase begins, during which the spacecraft's pitch angle is increased to 90 degrees, allowing it to climb almost vertically. The ignition phase lasts approximately 60 seconds, and the vehicle enters a coast phase. Following the completion of this phase, it is required that the vehicle attain and maintain an altitude of 100 km. However, to date, the vehicle has only reached heights of approximately 80/88 km. After a brief period of microgravity, the spacecraft assumes a particular attitude configuration, known as 'feathered', which involves lifting its aerodynamic tail surfaces in order to create a rapid descent. This configuration increases drag, allowing the vehicle to decelerate. Upon reaching an altitude of 21 km, the initial attitude is restored, allowing the spaceplane to glide towards the spaceport for a normal engine-off landing on a runway.

1.3 Grottaglie Airport

The airport of Taranto-Grottaglie is located in Puglia, it is partly used for military purposes and is home to the MARISTAER air base of the Marina Militare. In 2006, the Alenia Aeronautica Group became a partner of Boeing for the production of some components of the fuselage and the horizontal stabilizer of the new Boeing 787. The Foggia and Monteiasi-Grottaglie (Taranto) plants concentrate Alenia Aermacchi's activities in the field of composite materials. The Monteiasi-Grottaglie (Taranto) plant, inaugurated in 2006, is one of the most innovative aeronautical plants in the world, specifically designed to produce the composite sections of the Boeing 787 Dreamliner fuselage. Since 2004, the airport has undergone major upgrades to accommodate the Alenia plant. As the fuselages produced can only be transported by specially modified Boeing 747-400 LCF freighters, under an agreement with the Regione Puglia and ENAC, a complex of works was needed to extend the runway from 1,860 metres to 3,200 metres and to provide the necessary facilities. [4]

In May 2018, it was announced that the Taranto-Grottaglie Airport had been selected by the Ministry of Infrastructure and Transport for the construction of Italy's first operational spaceport for suborbital flights. The selection of the site for the Italian spaceport follows the agreement signed in December 2017 between Turin-based ALTEC (a company owned by ASI and Thales Alenia Space), Sitael (a company of the Angel Group) and Richard Branson's Virgin Galactic. According to the agreement between the companies, the operational possibilities of the Italian spaceport will be jointly evaluated for Virgin Galactic to carry out experimental suborbital flights, astronaut and pilot training, educational purposes and space tourism, also following the 2014 'Memorandum of cooperation in the development of commercial space transportation' agreement signed between ENAC (Ente Nazionale per l'Aviazione Civile) and FAA (Federal Aviation Administration), and renewed in 2016, and the cooperation agreement between the American FAA, ENAC and ASI (Agenzia Spaziale Italiana) on "Commercial Space Transportation" signed in June 2017 at the "Casa dell'Aviatore" of the Aeronautica Militare. In October 2020, ENAC's board of directors approved the regulations for the construction and operation of the airport, providing an official endorsement for the adaptation of the facility [5]. In addition, in November 2023, ENAC published the first edition of the "Suborbital and access to

space operations (SASO) regulation" [1], and, in December 2023, the third edition of the "Regolamento per la costruzione e l'esercizio degli spazioporti" [6]

Figure 1.1: SpaceShipTwo. [Credits: Scaled Composites]

Figure 1.2: WhiteKnightTwo with SpaceShipTwo mated. [Credits: Scaled Composites]

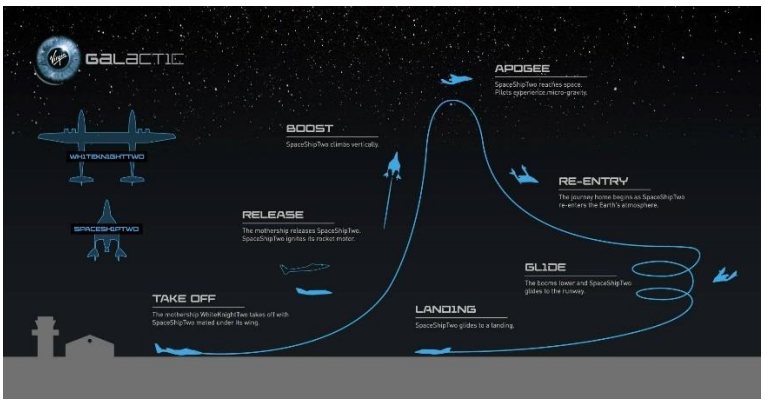

Figure 1.3: Flight path of SpaceShipTwo. [Credits: Virgin Galactic]

Chapter 2

Theoretical bases

In order to define and simulate a trajectory for the two aircraft that are the subject of this thesis, a comprehensive program of research was conducted that encompassed various fields of study. In particular, the work carried out can be divided into four macro-areas, namely: i) geometry; ii) aerodynamics; iii) propulsion; and iv) mission profile. This chapter illustrates the different mathematical models and tools used for each of these macro-areas.

2.1 Geometry

By analysing the tools to be used for the aerodynamic and propulsion characterisation of the two aircraft, the geometric parameters to be studied were identified. A reconstruction of the geometry of the two aircraft was achieved by utilizing data from the literature and a preliminary graphical reconstruction. The reconstruction started with an in-depth literature search, which yielded parameters for the carrier aircraft and the spaceplane.

2.2 Aerodynamic

Three models have been identified in literature for aerodynamic analysis: the Raymer Model; the Lifting-line Theory and the Digital DATCOM Software.

2.2.1 Raymer Model

This method has been derived from the book "Aircraft Design: A Conceptual Approach" by Daniel P. Raymer [7]. This comprehensive text addresses all critical aspects necessary for understanding aircraft design, ranging from preliminary sizing, aerodynamics, and structures to stability and control, propulsion, and performance. While the primary focus of the book is on the design of conventional aircraft, it also includes chapters detailing design procedures for unconventional aircraft. The book provides a preliminary method for aerodynamic analysis of an aircraft, applicable to generic high-speed configurations. This method facilitates the estimation of aerodynamic performance in subsonic, transonic and supersonic flight regimes. The inputs required for this method are detailed in the Table [2.1]. The model demands a comprehensive set of geometric inputs related to the wing, fuselage, engines, and tail surfaces of the aircraft.

A MATLAB script has been developed to implement this method. The script generates outputs for the lift and drag coefficient as a function of the Mach number, altitude and angle of attack.

Parameter	M.U	Parameter	M.U
Mach Number		Nacelle Diameter	[m]
Wing Surface	[m²]	Nacelle Length	[m]
Planform Surface	[m²]	Horizontal Tail Surface	[m²]
Wetter Surface	[m²]	Horizontal Tail Length	[m]
Exposed Surface	[m²]	Horizontal Tail Sweep	[deg]
Wingspan	[m]	Mean Aerodynamic chord (Horizontal Tail)	[m]
Leading Edge Sweep Angle (wing)	[deg]	Horizontal Tail thickness ratio	
Trailing Edge Sweep Angle (wing)	[deg]	Vertical Tail Surface	[m²]
Mean Aerodynamic chord (wing)	[m]	Vertical Tail Length	[m]
Maximum cross-sectional area	[m²]	Vertical Tail Sweep	[deg]
Wing Thickness ratio		Vertical Tail thickness ratio	
Fuselage Length	[m]	Mean Aerodynamic chord (Vertical Tail)	[m]
Fuselage Diameter	[m]		

Table 2.1: Inputs required by Raymer Model

2.2.1.1 Subsonic, Supersonic and Transonic Lift

This method provides formulas for estimating the lift coefficient based on the flight regime and speed. Specifically, the lift coefficient in subsonic flight conditions (Mach number < 0.8) is given from Equation (2.1):

$$C_L = C_{L0} + \left(\frac{\partial C_L}{\partial \alpha}\right)\alpha \tag{2.1}$$

where:

- C_{L0} is the zero-lift angle of attack. We set this parameter equal to zero, as we assumed the use of a symmetric airfoil;
- $\frac{\partial C_L}{\partial \alpha}$ is the lift curve slope of the wing;
- α is the angle of attack.

The lift curve slope of the wing is given by Equation (2.2):

$$C_{L\alpha} = \frac{2\pi A}{2+\sqrt{4+\frac{A^2\beta^2}{\eta^2}\left(1+\frac{tan^2\Lambda_{maxt}}{\beta^2}\right)}}\left(\frac{S_{exposed}}{S_{ref}}\right)(F) \tag{2.2}$$

where:

- A is the wing aspect ratio;
- β is a parameter that provides us with information about speed. In subsonic regime β is defined as:

$$\beta^2 = 1 - M^2 \tag{2.3}$$

- η is the airfoil efficiency, defined as:

$$\eta = \frac{C_{l\alpha}}{\frac{2\pi}{\beta}} \tag{2.4}$$

  Where $C_{l\alpha}$ is the lift curve slope of the wing airfoil. If $C_{l\alpha}$ is not known, Raymer's method suggests approximating η with the value 0.95;

- Λ_{maxt} is the leading edge sweep angle;
- $S_{exposed}$ is the wing reference area without the contribution of the fuselage;
- S_{ref} is the wing reference surface;
- F is the fuselage lift factor. It takes into account the fact that the fuselage generates lift due to the "spill-over" of the wing's lift. This parameter is given by:

$$F = 1.07\left(1 + \frac{d}{b}\right)^2 \tag{2.5}$$

  where:
  - "b" is the wingspan;
  - "d" is the fuselage diameter.

In regard to the supersonic flight regime, Mach > 1.2, the lift coefficient is calculated based on the slope of the wing lift curve given by Equation (2.6):

$$C_{L\alpha} = 4/\beta \tag{2.6}$$

where β is defined as:

$$\beta = \sqrt{M^2 - 1} \tag{2.7}$$

The wing lift coefficient is given by Equation (2.8):

$$C_L = C_{L\alpha}\,\alpha \tag{2.8}$$

Precisely, even in the supersonic flight regime, the lift coefficient of the wing will be obtained as a function of the flight velocity and the angle of attack.

In the transonic flight regime (0.8 < Mach < 1.2), a validated and rapid method for accurately estimating the wing's lift coefficient is currently unavailable. Instead, an initial and approximate approach is utilized. Specifically, the beta coefficient is computed for Mach numbers of 0.8 and 1.2, representing the lower and upper bounds of the transonic range. Subsequently, methodologies established for subsonic and supersonic regimes are applied to derive the slope of the lift coefficient curve at Mach 0.8 and 1.2, respectively. The lift coefficient is then determined across varying angles of attack under these conditions. Employing linear interpolation facilitates establishing a continuous relationship between the lift coefficient and Mach number. Although satisfactory for preliminary modelling, these methods yield results of limited accuracy.

To quantify the contribution made by the flaps to the maximum lift of the wing, Raymer's model proposes a first-order method that must be calibrated with test data on a real aircraft on which similar flaps are fitted. The Equations (2.9) and (2.10) provide a reasonable estimate of the increase in maximum lift and the change in the null lift angle for the various types of flaps used at the optimum angle to achieve high lift on landing.

$$\Delta C_{Lmax} = 0.9\Delta C_{lmax}\left(\frac{S_{flapped}}{S_{ref}}\right)cos\Lambda_{H.L} \tag{2.9}$$

$$\Delta\alpha_{OL} = (\Delta\alpha_{OL})_{airfoil}\left(\frac{S_{flapped}}{S_{ref}}\right)cos\Lambda_{H.L} \tag{2.10}$$

where:

- ΔC_{lmax} is the maximum lift coefficient increase of the airfoil can be obtained from the tests conducted for that specific airfoil;
- $S_{flapped}$ is the area of wing having flap;

- $\Lambda_{H.L}$ is the sweep referring to the hinge line of the high-lift surface.

2.2.1.2 Subsonic Drag

The model considers the following contributions to the drag coefficient:

- Parasite drag (C_{D0}) is a type of aerodynamic drag that is a combination of form drag and skin friction drag;
- Induced drag is the result of an airfoil generating lift.

In the subsonic case, parasite drag is calculated as the sum of the following contributions: i) total component drag; ii) the contribution of miscellaneous drag ($C_{D_{misc}}$) which is related to the presence of flap, non-retracted landing gear, upswept aft fuselage, and base area; iii) the contribution related to losses and protuberances ($C_{D_{L\&P}}$). The Equation (2.11) is employed for the calculation of parasite drag in Raymer Model.

$$(C_{D0})_{subsonic} = \frac{\sum(C_{fc}FF_cQ_cS_{wetc})}{S_{ref}} + C_{D_{misc}} + C_{D_{L\&P}} \quad (2.11)$$

where:

- C_{fc} is the calculated flat-plate skin-friction drag coefficient. This coefficient is linked to the value of the Reynolds number. In fact, above a certain value of the Reynolds number, the flow on the surfaces of the aircraft changes from laminar to turbulent, which increases the coefficient of friction (C_{fc}) and, consequently, an increase in the resistance. The Reynolds number is defined by the following formula:

$$R = \frac{\rho V l}{\mu} \quad (2.12)$$

  where:

  - l represents the characteristic length used in Reynolds number calculations, varying depending on the reference component. For instance, for the fuselage, l corresponds to its total length, whereas for the wing and tail, l approximates the length of the mean aerodynamic chord;
  - V is the aircraft speed;
  - ρ and μ are the density and dynamic viscosity of the fluid surrounding the body, respectively.

  The value of the Reynolds number determines whether the flow is laminar or turbulent. In the case of laminar flow, the value of C_{fc} is calculated as follows:

$$C_{fc} = \frac{1.328}{\sqrt{R}} \quad (2.13)$$

  In the case of turbulent flow, Raymer's model suggests calculating the "cutoff Reynolds number", which is defined as follows:

$$R_{cutoff} = 38.21\left(\frac{l}{k}\right)^{1.053} \quad (2.14)$$

  where l represents the characteristic length and k denotes the skin-roughness value, which is typically found in literature tables and varies based on the material coating of the component. If the calculated Reynolds number exceeds a specified cutoff value, the latter is utilized in the calculation

of the skin-friction coefficient C_f, accounting for increased drag due to surface roughness. Under these circumstances, the skin-friction coefficient for a flat plate is determined using the formula:

$$C_{fc} = \frac{0.455}{\log(Re)^{2.58}(1+0.144*M^2)^{0.65}} \quad (2.15)$$

This C_f estimate applies universally to all aircraft components, including the wing, fuselage, vertical and horizontal tail surfaces, nacelles, pylons, and other structures;

- FF is the form factor. This parameter takes into account the pressure drag due to flow separation. The FF value is estimated with empirical considerations. For wing, tail, strut and pylon the value of FF is calculated with the following formula:

$$FF = \left[1 + \frac{0.6}{\left(\frac{x}{c}\right)_m}\frac{t}{c} + 100\left(\frac{t}{c}\right)^4\right][1.34M^{0.18}(cos\Lambda_m)^{0.28}] \quad (2.16)$$

where:

  - $\left(\frac{x}{c}\right)_m$ is the chordwise location of the airfoil maximum thickness point;
  - $\left(\frac{t}{c}\right)$ is the thickness ratio of the airfoil;
  - Λ_m is the value of the sweep angle of the maximum-thickness line;
  - M is the Mach number.

While for fuselage the value of FF is calculated with the formula:

$$FF = \left[0.9 + \frac{5}{f^{1.5}} + \frac{f}{400}\right] \quad (2.17)$$

where f is given by the ratio between the characteristic length and the diameter of the components.

For nacelle and external store, FF is calculated with:

$$FF = 1 + \left(\frac{0.35}{f}\right) \quad (2.18)$$

The pressure drag contribution of an external boundary-layer diverter, mounted on the fuselage for a jet inlet, is estimated using Equation (2.19) for a double-wedge diverter and Equation (2.20) for a single-wedge diverter:

$$FF = 1 + \left(\frac{d}{l}\right) \quad (2.19)$$

$$FF = 1 + \left(\frac{2d}{l}\right) \quad (2\ 20)$$

where:

  - d is the jet inlet diameter;
  - l is the jet inlet length.

- Q is the interference factor. This parameter estimates the interference effect due to mutual interference between components. When components such as the wing and fuselage intersect, their boundary layers merge, resulting in the formation of a thicker boundary layer. This phenomenon increases the drag on the aircraft, as well as the likelihood of pressure-induced separation and flow reversal, which further contribute to the overall drag. The phenomenon of interference drag is also attributed to the phenomenon of "superspeed," whereby the airflow around a body, such as the fuselage, accelerates to a velocity exceeding that of the free stream. This accelerated flow exerts a

greater dynamic pressure, thereby increasing the drag on any component within the flow, contributing further to the phenomenon of interference drag. Tabulated values for the interference factor can be found in the relevant literature;

- $C_{D_{misc}}$ is the Miscellaneous drag component. It takes into account the various aircraft components that protrude into the flow, such as external fuel tanks that are not smooth. An empirical formula derived from test data is used to calculate this contribution. This allows us to derive the parameter *D/q*, which is resistance divided by dynamic pressure, also known as drag area. By dividing the *D/q* parameter by the reference area of the wing, it is possible to obtain the drag coefficient for that particular component. Typically, transport aircraft have a swept back fuselage which further increases the parasite drag of the fuselage. This drag component can be estimated using Equation (2.21):

$$D/q_{upsweep} = 3.83u^{2.5}A_{max} \tag{2.21}$$

where:

  - u is the upsweep angle of the fuselage centerline;
  - A_{max} is the maximum cross-sectional area of the fuselage.

The flat aft surfaces, known as "base", create significant "base drag". This can be estimated using specific equations and includes both flat surfaces and steeply angled regions which tend to separate the airflow, typically when the aft angle exceeds 20 degrees. Equation (2.22) and Equation (2.23) allow us to estimate this contribution in subsonic and supersonic flight regimes.

  - Subsonic:

$$D/q_{base} = [0.139 + 0.419(M - 0.161)^2]\, A_{base} \tag{2.22}$$

  - Supersonic:

$$D/q_{base} = [0.064 + 0.042(M - 3.84)^2]\, A_{base} \tag{2.23}$$

In calculating the aerodynamic drag for an aircraft, it is also necessary to keep track of the smallest components. The drag for these components is typically estimated from test data of similar aircraft. Raymer's model provides the Table (2.2) in which the values of the parameter *D/q* divided by the reference area of the wing are given, which allows us to obtain the parasite drag coefficient for these components. The drag coefficients referring to the frontal area of the component are called $C_{D\pi}$;

- $C_{D_{L\&P}}$ is the leakage and protuberances drag component. It can be observed that these two factors tend to increase aerodynamic drag. The term "protuberance" is used to describe a number of different components, including antennas, lights, door edges, fuel intakes, external control surface hinges, actuator fairings and manufacturing defects. It is not possible to calculate the contribution to aerodynamic drag due to these components at the conceptual design stage. In this instance, an estimation of the increase in drag is calculated as a percentage of the total parasite drag. Table [2.3] illustrates the percentages utilized for specific components.

The second contribution to the subsonic drag coefficient is the induced drag. The phenomenon of induced drag can be attributed to the generation of lift. Classical wing theory posits that the induced drag can be calculated using the following formula:

$$C_{Di} = KC_L^2 \tag{2.24}$$

where K is the drag-due-to-lift factor. In subsonic flight, K is given by the following equation:

$$K = \frac{1}{\pi eA} \tag{2.25}$$

Where:

- e is the Oswald efficiency factor. This factor considers the increase in induced drag resulting from the non-elliptical distribution of lift on the wing. The Oswald factor is a function of both the sweep angle of the wing and aspect ratio. The e factor can be calculated using two different formulas, depending on the sweep angle of the wing:
  - Straight-wing aircraft:
  $$e = 1.78(1 - 0.045A^{0.68}) - 0.64 \tag{2.26}$$
  - Swept-wing aircraft:
  $$e = 4.61(1 - 0.045A^{0.68})(cos\Lambda_{LE})^{0.15} - 3.1 \tag{2.27}$$

  The Equation (2.26) is applicable to values of sweep angle less than 2, whereas the Equation (2.27) is applicable to values of sweep angle greater than 30. In the case of sweeps between 2 and 30, it is necessary to interpolate linearly between the results obtained from the two Equations;
- A is the wing aspect ratio.

The presence of the flaps has an influence upon both parasite and induced drags. In the first case, the flow separation above the flaps causes an increase in parasite drag. This increase in drag can be accounted for by means of Equation (2.28):

$$\Delta C_{D0flap} = F_{flap}\left(\frac{C_f}{C}\right)\left(\frac{S_{flapped}}{S_{ref}}\right)(\delta_{flap} - 10) \tag{2.28}$$

Where:

- C_f is the flap chord length;
- δ_{flap} is the flap deflection;
- F_{flap} is the form factor, which is dependent on the specific type of flap in question.

In the second scenario, the presence of the flap induces higher lift in the region of the wing where the high-lift device is deployed, thereby altering the lift distribution across the wing. This modification results in an increase in the induced drag term. Equation (2.30) provides a preliminary estimation of the induced drag increment.

$$\Delta C_{Di} = k_{flap}^2\left(\Delta C_{Lflap}\right)^2 \cos\left(\Lambda_{c/4}\right) \tag{2.29}$$

	$C_{D_\pi} = \left[\frac{D/q}{\text{Frontal Area}}\right]$
Flat plate perpendicular to flow	1.28
Sphere alone—high R#	0.10
Sphere alone—low R#	0.3–0.5
Hollow sphere, open end forward	1.40
Hollow sphere, open end to rear	0.40
Bullet shape, blunt back	0.30
Exposed water—cooled radiator	1.00
Cowled water—cooled radiator	0.3–0.5
Air scoops	1.2–2.0
Control horn	0.3–0.8
Speed brake—fuselage mounted	1.00
Speed brake—wing mounted	1.60
Windshield smoothly faired into fuselage	0.07
Windshield—sharp edged, poorly faired	0.15
Open cockpit (ref. windscreen A-frontal)	0.50
Parachute or drogue chute	1.40
Regular wheel and tire	0.25
Second wheel and tire in tandem	0.15
Streamlined wheel and tire	0.18
Wheel and tire with fairing	0.13
Streamlined strut $(1/6 < t/c < 1/3)$	0.05
Round strut or wire (R# $> 3 \times 10^5$)	0.30
Round strut or wire (R# $< 3 \times 10^5$)	1.17
Flat spring gear leg	1.40
Fork, bogey, irregular fitting	1.0–1.4

Table 2.2: Miscellaneous and Landing-Gear Component Drags [7]

Aircraft Type	Drag, %
Propeller aircraft	5–10
Jet transports or bombers	2–5
Non-stealth fighters	10–15
Stealth fighters	3–5

Table 2.3: Typical factor for Leakage and Protuberance Drag

2.2.1.3 Supersonic Drag

In the supersonic flight regime, the parasite drag term is calculated using the Equation (2.30). In contrast to the subsonic case, the wave drag term incorporates all pressure drags within it. Furthermore, the skin friction drag is not subject to adjustments for form factors or interference effects. These are both forms of pressure drag.

$$(C_{D0})_{supersonic} = \frac{\sum(C_{fc}S_{wetc})}{S_{ref}} + C_{D_{misc}} + C_{D_{L\&P}} + C_{D_{wave}} \tag{2.30}$$

where:

- C_{fc} is the supersonic turbulent skin-friction coefficient. In order to calculate the C_{fc}, the same formulas are employed as are used for the estimation of C_{fc} in the subsonic flight regime, both in the laminar and turbulent cases, as a function of the Reynolds number and the cutoff Reynolds number. The distinction in this case lies in the calculation of the cutoff Reynolds number, which is calculated using a formula that is applicable in the supersonic and transonic regime:

$$R_{cutoff} = 44.62\left(\frac{l}{k}\right)^{1.053} M^{1.16} \tag{2.31}$$

- $C_{D_{misc}}$ is the miscellaneous drag. The $C_{D_{misc}}$ calculation has already been described in detail above;
- $C_{D_{L\&P}}$ is the drag due to leaks and protuberances. In supersonic flight, this drag contribution exhibits a similar percentage distribution as seen in subsonic flight;
- $C_{D_{wave}}$ is the wave drag. The additional drag that occurs during supersonic flight is a function of pressure resistance due to shock formation. This phenomenon can be attributed to the distribution of the aircraft's volume from its nose to its tail.
  The Equation (2.32) allows for the preliminary calculation of the wave drag:

$$(D/q)_{wave} = E_{WD}[1 - 0.386(M - 1.2)^{0.57}\left(1 - \frac{\pi\Lambda_{LE-deg}^{0.77}}{100}\right)](D/q)_{Sears-Haack} \tag{2.32}$$

  where:
  - E_{WD} is an empirical wave drag efficiency factor. It is given by the ratio between actual wave drag and the Sears-Haack value;
  - $(D/q)_{Sears-Haack}$ is the Sears-Haack body wave drag. The Sears-Haack body is defined by the following equation:

$$\frac{r}{r_{max}} = \left[1 - \left(\frac{x}{\frac{l}{2}}\right)^2\right]^{0.75} \tag{2.33}$$

    where:
    - r is the cross-section radius;
    - l is the longitudinal dimension.

    This body is capable of producing an optimal volume distribution, resulting in the lowest possible wave drag for any closed body with a circular cross-section of the same length and total volume. The wave drag of this body can be calculated using the following formula:

$$(D/q)_{wave} = \frac{9\pi}{2}\left(\frac{A_{max}}{l}\right)^2 \tag{2.34}$$

    where:
    - A_{max} is the maximum cross-sectional area. It can be estimated from the aircraft volume-distribution plot;
    - l is the aircraft length except for any portion of the aircraft with a constant cross-sectional area, which should be subtracted from the length.

In the context of supersonic flight, the contribution of induced drag can be calculated using the Equation (2.24). The value of the drag-due-to-lift factor, designated as K, is observed to be higher. In this flight regime, the value of K is also a function of the Mach number. The K factor is determined by the following equation:

$$K = \frac{A(M^2-1)cos\Lambda_{LE}}{\left(4A\sqrt{M^2-1}\right)-2} \tag{2.35}$$

2.2.1.4 Transonic Drag

Raymer's theory [7] does not provide an accurate method for evaluating the drag coefficient in transonic flight. In this regime, the drag coefficient is calculated by interpolation. Specifically, a curve is drawn from certain characteristic points, such as A) the point for Mach 1.2, for which the drag is calculated using equation (2.33); B) the point for Mach 1.05, for which the drag is generally the same as for the previous point at Mach 1.2; C) the point for Mach 1, for which there is a value of wave drag approximately half that calculated for the previous point at Mach 1. 05; D) the point for Mach corresponding to the divergence Mach, which by definition has a drag value of 0.002; E) the point for Mach corresponding to the critical Mach, i.e., the point at which an increase in drag occurs. Once these points have been identified, three curves can be drawn: a straight-line connecting points B and C; a curve from point E to point D; and a curve connecting point B to point A. The result is shown in Figure (2.3).

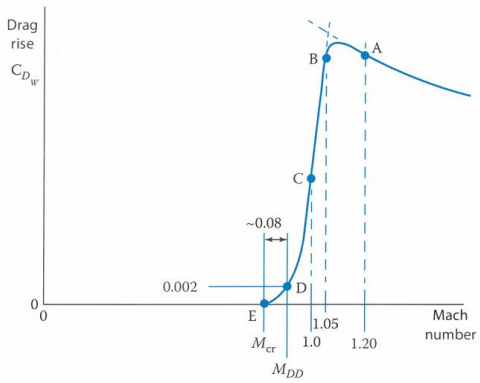

Figure 2.3 Transonic Drag Rise estimation *[7]*

2.2.2 Lifting-line theory

The Lifting-line theory [8] is a mathematical formulation developed by Ludwig Prandtl that allows the calculation of the lift distribution along a finite aspect ratio wing, thereby enabling the analysis of aerodynamic performance under different flight conditions. This theory is fundamental to aircraft wing design, as it optimizes the wing shape for maximum aerodynamic efficiency. However, this mathematical model does not take compressible effects into account, which results in reduced accuracy in transonic and supersonic regimes. Prandtl's scheme applies to wings with a high aspect ratio and minimal deflection. The underlying assumption of this theory is that, although the flow around the wing is three-dimensional, it can be approximated by a linear summation of the two-dimensional flows around the airfoils that comprise the wing. In this scheme, the airfoil can be represented by a vorticity distribution, by the theory of thin profiles, or by an equivalent vortex when considering Kutta-Joukowski transformations. In the initial scenario, the vortex surface is represented by a linear distribution of vortices with a width equal to the chord and an infinite extension. In the subsequent case, the equivalent vortex is an infinite rectilinear thread. In light of the finite extension of the wing, it is not feasible to consider truncating the fillet or the vortex surface at the wingtips, as this would conflict with Helmholtz's first theorem for vortex motion. A potential solution would be to have the vortical fillets converge toward the wing's center. However, this would create a net flow of vorticity through each section of the null area, thereby cancelling out the lift force.

Moreover, as one progresses along the y-axis, the circuitry must undergo a corresponding alteration, exhibiting a symmetrical distribution concerning the centreline and a null state at the wingtips. This final observation implies a change in the net vorticity flow through the airfoils. This is only possible if the vorticity system, which represents the wing, is permitted to exit the wing. Consequently, a vorticity system of a finite aspect ratio wing that adheres to the tenets of vorticity dynamics must comprise two distinct surfaces:

- A surface of swirling motion adhering to the wing, with lines of swirling motion aligned along the wingspan;
- A surface of free motion, originating at the trailing edge of the wing and continuing infinitely downstream, along which the swirling lines are essentially aligned with the uniform current.

The second surface, designated as the free surface, represents the wing wake. The vortex threads on the free surface, as a result of mutual induction, tend to translate towards the extremities of the surface itself, which therefore tends to roll up.

In order to study the characteristics of the wake, it is necessary to take this aspect into account. To achieve this, Prandtl introduced a vortex model in which the wing is replaced by a swirling surface. In his model, the German scholar Prandtl considered an infinite number of stirrup vortices, each with a different length of the adhering vortex. However, all of the adhering vortices were aligned along a single line, called the leading line, which replaced the adhering vortex surface. This line was positioned along the line of the fires. This results in the creation of multiple end vortex threads along the wingspan. The intensity of each end vortex is equal to the change in circuitry along the carrier line. If we consider the case where an infinite number of stirrup vortex threads are superimposed along the carrier line, it can be shown that each of them will have an intensity of $d\Gamma$. Consequently, a continuous distribution $\Gamma(y)$ will be obtained along the wingspan.

Consider the value of the circuitry at the origin, designated as $\Gamma 0$. If we consider an infinitesimal segment of the lifting line, dy, placed at coordinate y, the circuitry at y is $\Gamma(y)$ and the change in circuitry is $d\Gamma = (d\Gamma/dy)dy$.

Consider now an arbitrary point on the lifting line, designated as y_0. Each segment dx of the threads aligned along the direction of the undisturbed current will induce in y_0 a velocity with intensity and direction given

by Biot-Savart's law. Consequently, the velocity induced in y_0 by the portion of the free swirling surface present in y can be expressed by the following equation:

$$dw = -\frac{(d\Gamma/dy)/dy}{4\pi(y_0-y)} \tag{2.36}$$

In accordance with the reference system that has been adopted, it is imperative to incorporate a negative value into the aforementioned formula. This is to ensure that there is a positive dw component when the circuitry undergoes a decrease along the wingspan. Consequently, $d\Gamma/dy$ must be expressed as a negative value. The total velocity w induced in y_0 by the entire free swirling surface is given by the following equation:

$$w(y_0) = -\frac{1}{4\pi}\int_{\frac{-b}{2}}^{\frac{b}{2}} \frac{(d\Gamma/dy)/dy}{(y_0-y)} \tag{2.37}$$

A generic profile at position y_0 can be used as a reference point to determine the induced incidence α_i. This is calculated using the following formula:

$$\alpha_i(y_0) = tan^{-1}(\frac{-w(y_0)}{V_\infty}) \tag{2.38}$$

Given that w is considerably smaller than V_∞, it can be written as follows:

$$\alpha_i(y_0) = \frac{-w(y_0)}{V_\infty} \tag{2.39}$$

By making appropriate substitutions, we obtain the following equation, used to calculate the induced incidence at point y_0:

$$\alpha_i(y_0) = \frac{1}{4\pi V_\infty}\int_{\frac{-b}{2}}^{\frac{b}{2}} \frac{(d\Gamma/dy)/dy}{(y_0-y)} \tag{2.40}$$

Let us now consider the effective incidence, α_{eff}. The effective incidence will vary along the wingspan as the downwash varies along the y-axis. Therefore, the effective incidence can be expressed as a function of the y-axis coordinate, namely $\alpha_{eff} = \alpha_{eff}(y_0)$. The lift coefficient for each individual section located at $y = y_0$ is given by:

$$c_l = 2\pi k(\alpha_{eff} - \alpha_0) \tag{2.41}$$

In accordance with the Kutta-Joukowski theorem, the lift for the single section situated at $y = y0$ can be calculated as follows:

$$L' = \frac{1}{2}\rho_\infty V_\infty c_l c(y_0) = \rho_\infty V_\infty \Gamma(y_0) \tag{2.42}$$

From the above equation, it can be deduced that:

$$c_l = \frac{2\Gamma(y_0)}{V_\infty c(y_0)} \tag{2.43}$$

Substituting the c_l formula just found into the (2.41) gives:

$$\frac{\Gamma(y_0)}{V_\infty c(y_0)} = \pi k(\alpha_{eff} - \alpha_0) \tag{2.44}$$

$$\alpha_{eff} = \frac{\Gamma(y_0)}{\pi k V_\infty c(y_0)} + \alpha_0 \tag{2.45}$$

Consequently, the formula for the geometric incidence, $\alpha(y_0)$, is finally obtained:

$$\alpha(y_0) = \frac{\Gamma(y_0)}{\pi k V_\infty c(y_0)} + \alpha_0 + \frac{1}{4\pi V_\infty} \int_{\frac{-b}{2}}^{\frac{b}{2}} \frac{(d\Gamma/dy)/dy}{(y_0 - y)} \tag{2.46}$$

The equation presented above is the Prandtl integro-differential equation in which the sole unknown is $\Gamma(y0)$. The solution thus allows us to calculate $\Gamma(y_0)$, which, in turn, enables the aerodynamic characteristics of the wing at finite elongation to be calculated. For each individual section, once the value of $\Gamma(y_0)$has been calculated, it will be possible to determine the lift generated by that section, L', using the previously written formula. The total lift is obtained by integrating along the entire wingspan, L'.

$$L = \int_{\frac{-b}{2}}^{\frac{b}{2}} L'(y)dy = \rho_\infty V_\infty \int_{\frac{-b}{2}}^{\frac{b}{2}} \Gamma(y)dy \tag{2.47}$$

The lift coefficient of the entire wing will be as follows:

$$C_L = \frac{2}{V_\infty S} \int_{\frac{-b}{2}}^{\frac{b}{2}} \Gamma(y)dy \tag{2.48}$$

With regard to induced drag, an analysis of a single section will yield the following results:

$$D_i' = L' \sin(\alpha_i) \tag{2.49}$$

Given that the angle α_i is to be considered small, it can be written as:

$$D_i' = L'\alpha_i \tag{2.50}$$

The total induced drag will then be calculated as follows:

$$D_i = \rho_\infty V_\infty \int_{\frac{-b}{2}}^{\frac{b}{2}} \Gamma(y)\alpha_i(y)dy \tag{2.51}$$

The induced drag coefficient will be calculated as follows:

$$C_{Di} = \frac{2}{V_\infty S} \int_{\frac{-b}{2}}^{\frac{b}{2}} \Gamma(y)\alpha_i(y)dy \tag{2.52}$$

2.2.3 Digital DATCOM Software

The Digital DATCOM software [9] employs semi-empirical calculation methods to estimate aircraft aerodynamic characteristics. The methods implemented in the code are largely derived from wind tunnel tests, which are conducted under varying configurations to account for interference between components, viscosity, and compressibility.

Digital DATCOM can be utilized in the preliminary stages of aircraft design, as it offers rapid assessments with acceptable precision.

The software requires the input of a file containing the following information:

- Aircraft geometry and component parameters;
- Profile for the wing, profile for the horizontal tailplane, profile for the vertical tailplane;
- Flight conditions;
- Global parameters (wing position relative to the fuselage, center of gravity, etc.);
- Data relating to symmetrical (flaps, rudder, balancer) and asymmetrical (ailerons) control surfaces;
- Propulsion data (number of engines, engine area, positioning, etc.).

Intervals are established for Mach, altitude and angle of attack. Subsequently, the software is capable of conducting three distinct types of analysis, including:

1. Mach and elevation vary together;
2. Mach varies at set altitude;
3. Quota varies at fixed Mach.

2.2.4 Comparison of methods and limitations

This section will highlight the differences and commonalities between these three distinct methods that permit the preliminary estimation of an aircraft's aerodynamic performance. It is crucial to emphasize that none of the aforementioned methods is capable of analyzing an aircraft with a twin-fuselage configuration. Consequently, the contribution of this innovative configuration to lift and drag coefficients cannot be fully appreciated.

Regarding propulsion, it should be noted that the Digital DATCOM software does not permit the importation of aircraft with more than two engines. In contrast, the other two models permit the entry of an arbitrary number of engines.

The MATLAB script that implements the Lifting-line theory requires as input the lift and drag coefficients both with respect to the angle of attack for the airfoils of wing, horizontal tail, and vertical tail. In order to obtain the required data, it is necessary to perform an aerodynamic analysis of the two-dimensional airfoils using secondary software at a given Reynolds number value, with known altitude and speed conditions, at a specific angle of attack. Once the airfoils data has been obtained, it is fed into the script implementing the Prandtl model, which outputs the aircraft's lift and drag coefficients at a specific flight condition. In order to obtain an aerodynamic database of lift and drag characteristics as a function of the angle of attack, flight Mach and altitude, it is necessary to commence with the 2D profile analysis and then repeat all the calculations for a different Reynolds number value. Obtaining an aerodynamic characterization of the aircraft is a time-consuming process, as it is linked to the 2D airfoils of the aircraft that have been assumed to be missing from the literature.

Prandtl's Lifting-line theory is only applicable to subsonic flight regimes. Nevertheless, it can be employed for the aerodynamic analysis of the carrier's mated and standalone configurations, provided that the flight Mach number is less than 0.65.

Conversely, the script that implements Raymer's model is not contingent on the two-dimensional analysis of the airfoils, thus enabling it to furnish the aerodynamic databases with lift coefficient and drag coefficient data for the entire aircraft as a function of the angle of attack, Mach number and altitude in a single iteration. This method considers two-dimensional profiles via the t/c parameter value of the three airfoils of the wing, horizontal tailplane and vertical tailplane, respectively. One significant drawback of this model is its inability to accurately predict transonic flight conditions. In this instance, the data were obtained by linear interpolation between the last data obtained in the subsonic regime (for Mach 0.8) and the first data obtained in the supersonic regime (Mach 1.2). Consequently, it is necessary to conduct CFD simulations to obtain more realistic values for the transonic flight regime.

The Digital DATCOM software only applies in the subsonic flight regime; therefore, it has only been used for mated and carrier standalone configurations. Similarly, the software allows the user to select the airfoil for the wing and the horizontal and vertical tail. In this instance, the analyses are conducted directly within the software, obviating the necessity to import 2D analyses. The principal limitation of this approach is the reliance on strong approximations regarding the aircraft geometry, which is partly attributable to the paucity of data and the inherent limitations of the software.

2.3 Propulsion

The WhiteKnightTwo is equipped with four turbofan engines with separate flows, each capable of providing a maximum thrust of 30.69 kN.

In order to characterize the propulsive performance of the carrier, a database is required including thrust and mass flow as a function of flight altitude, Mach number and throttle. A code implementing Mattingly's method was employed to calculate the engine performance. This model enables the estimation of turbofan performance in terms of thrust and specific consumption, given the requisite parameters for trajectory simulation software. This simplified procedure is sufficiently accurate for preliminary analyses. The output of the MATLAB script that implements this model is the two databases, one for thrust ($Thrust = f(Altitude,\ Mach,\ Throttle)$) and one for mass flow ($Mass\ Flow = f(Altitude,\ Mach,\ Throttle)$), both of which refer to the single engine.

The SpaceShipTwo is equipped with a hybrid rocket motor, for which the specific impulse and thrust parameters, crucial for trajectory simulation on ASTOS software, are readily available in the literature.

2.4 Mission Profile

The suborbital mission performed by the WhiteKnightTwo and SpaceShipTwo can be broken down into a series of distinct phases. At each stage of the mission, a different configuration of the aircraft system is observed. Specific software enables the definition and simulation of a trajectory for the vehicles performing the suborbital mission.

2.4.1 ASTOS Software

ASTOS is a computer software designed to simulate, analyse, and optimize the trajectory of an aircraft. It is primarily employed in the field of space applications [10].

In ASTOS, the inputs required for the simulation of a mission profile for an aircraft are:

- The aerodynamic database: it must contain the values of the lift coefficient and drag coefficient, both as a function of angle of attack and as a function of flight Mach, respectively;
- The propulsive database: it must contain the value of thrust and specific consumption as a function of throttle, Mach number, and altitude;
- The masses: the software requires knowledge of the structural mass of the aircraft and the mass of fuel on board the aircraft.

The ASTOS software enables the user to input the precise date and time of the mission, as well as the coordinates of the departure airport. In order to simulate the trajectory, it will be necessary to define the various phases of the mission profile. This will require the specification of phase time, engine performance in terms of throttle required in that particular flight condition, and attitude control in the various phases. The attitude control can be defined in terms of pitch angle and yaw angle, or in terms of angle of attack and bank angle. The output of the program is the performance of the aircraft in terms of flight Mach, altitude, angle of attack, fuel consumption, thrust performance (etc.) of the aircraft at any given instant during the mission. A limitation of this software in the context of this study is its inability to simulate the take-off and landing phases with sufficient accuracy. This is due to its design for space applications, which involve vertical take-off using a launcher.

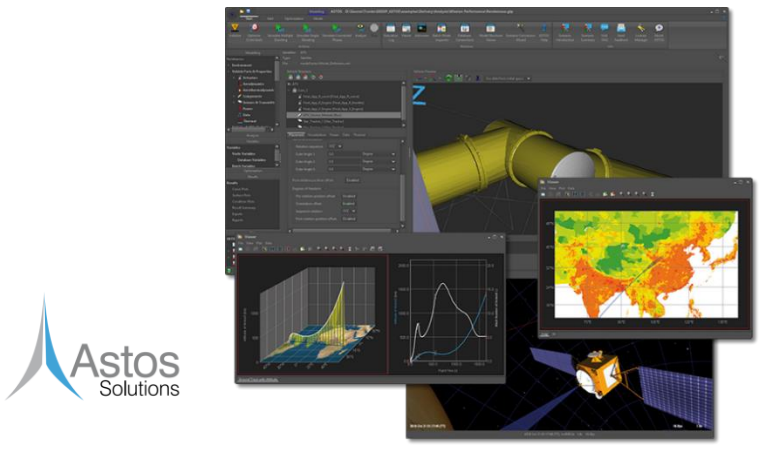

Figure 2.5: Example of ASTOS graphical interface and output [Credits *[10]*]

2.4.1.1 Input for ASTOS simulation

The inputs required by the ASTOS software to simulate the trajectory of our aircraft system are distinct. The initial inputs required are the setting of the reference celestial body, the Earth, and the reference atmosphere, which for the purposes of this case study will be US Standard (US Std 76).

The following inputs are required for the WhiteKnightTwo (WK2) and SpaceShipTwo (SS2) models:

- Structural mass, propellant type and propellant mass for WK2;
- Structural mass, propellant type and propellant mass for SS2;
- Reference area for WK2;
- Reference diameter for SS2 in boost phase, coast un-feathered and feathered phases and re-entry feathered phase;
- Reference area for SS2 in re-entry un-feathered phase and glide.

In terms of aerodynamics, the software requires the input of the following data:

- An aerodynamic database ($C_L = f(Mach,\ alpha)$, $C_D = f(Mach,\ alpha)$) for the mated configuration;
- An aerodynamic database ($C_L = f(Mach,\ alpha)$, $C_D = f(Mach,\ alpha)$) for the standalone carrier configuration;
- An aerodynamic database ($C_L = f(Mach,\ alpha)$, $C_D = f(Mach,\ alpha)$) for the SpaceShipTwo feathered configuration;
- An aerodynamic database ($C_L = f(Mach,\ alpha)$, $C_D = f(Mach,\ alpha)$) for the SpaceShipTwo un-feathered configuration.

From the standpoint of propulsion, ASTOS necessitates as inputs:

- The engine type of the WhiteKnightTwo;
- The engine type of the WhiteKnightTwo the SpaceShipTwo;
- A propulsive database ($T = f(Altitude,\ Mach,\ Throttle)$) for the thrust of the single engine of the WhiteKnightTwo;
- A propulsive database ($Mass\ Flow = f(Altitude,\ Mach,\ Throttle)$) for the Mass Flow of the single engine of the WhiteKnightTwo;
- The number of engines on the carrier aircraft is required in order to scale the databases for the single engine;
- The nozzle area of the SpaceShipTwo's rocket engine is also necessary;
- The vacuum thrust of the SpaceShipTwo must be provided;
- The vacuum Isp of the SpaceShipTwo must also be supplied.

The following data is required for the simulation of a mission profile with a georeferenced route:

- The geographical coordinates of the runway of the departure airport;
- All the flight phases, including the duration and altitude constraints pertaining to the WhiteKnightTwo and SpaceShipTwo mission;
- The airspace areas in which the mission can be carried out, defined by polygons;
- The waypoints in terms of geographical coordinates defining the flight corridor for the post-take-off phase and the pre-landing phase.

2.4.2 QGIS Software

QGIS is a free and Open-Source Geographic Information System released under the GNU General Public License (GPL) [11]. The QGIS software enables the visualisation, organisation, analysis and representation of spatial data. This software is used for:

- Day-to-day GIS data visualization;
- Data acquisition;
- Advanced GIS analyses;
- Presentations in form of maps, atlases and report.

QGIS facilitates the integration of data from various sources into a unified spatial analysis project. The data is partitioned into layers, which can be analysed individually or collectively on a single map. The map can be customised by the user according to the analysis to be performed. It can also be enhanced with icons and labels that are dependent on the attributes of the map elements. A scripting system can be invoked to automate repetitive operations on the data.

2.4.3 ISTAT data

ISTAT (Istituto nazionale di statistica) is a public research institute [12]. The objective of the ISTAT is to provide statistical information, analyses and forecasts in the economic, social and environmental fields. The ISTAT website offers content in open formats, including graphics, information, and data that can be reused by users on other sites. The section on 'territorial bases' within the ISTAT portal contains mosaicked geographical data at the national level in geographical projection, covering the census sections for the years 1991-2011. The aforementioned data can be accessed via the QGIS software.

The ISTAT website offers access to the results of the 2021 Italian census, which includes data on the permanent population of all municipalities and first-level administrative sub-municipal areas. The file on the census sections by region contains the following information:

- A numeric code that uniquely identifies the region within the national territory;
- The name of the region;
- A numeric code that uniquely identifies the province within the national territory;
- The name of the province;
- A numeric code that uniquely identifies the municipality within the territory of the province;
- The name of the municipality;
- A numeric code that uniquely identifies the municipality within the national territory;
- A numeric code that uniquely identifies the 2011 census section within the national territory;
- The resident population, total;
- The resident population, by category.

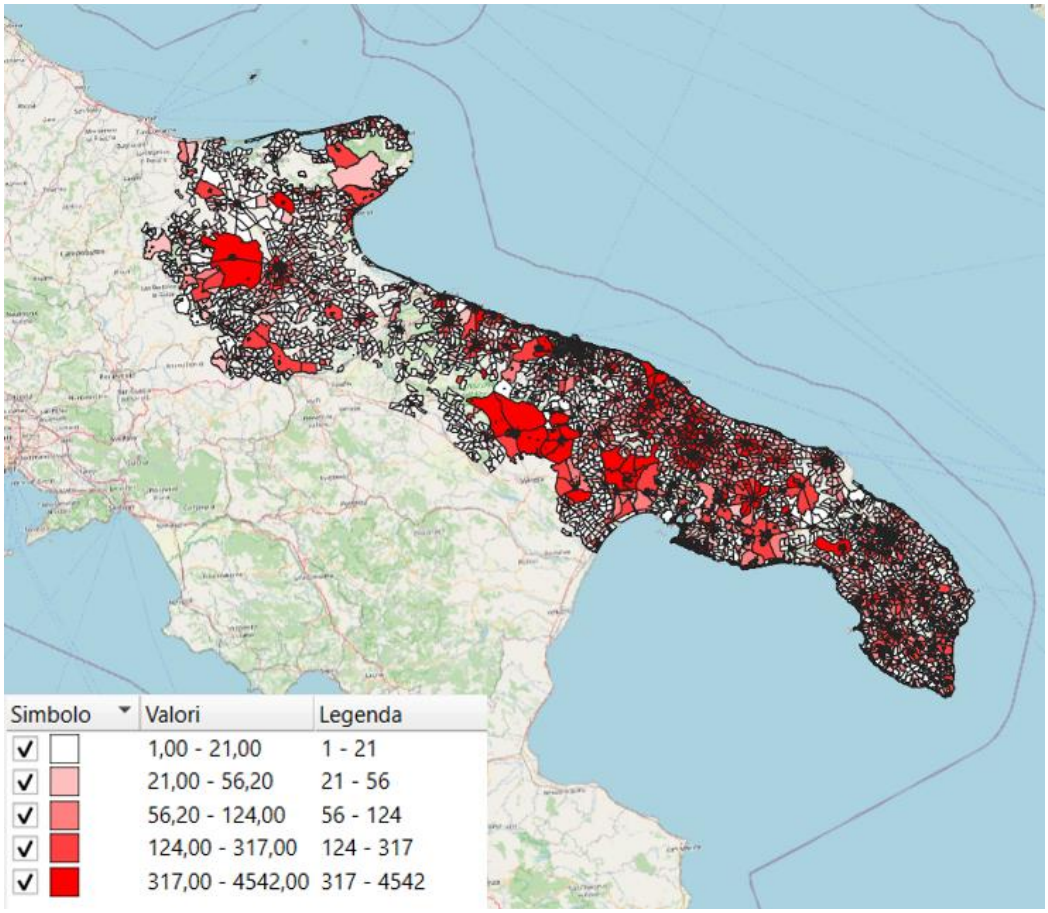

Figure 2.4 Example of an analysis carried out on QGIS by importing statistical data to visualise the distribution of the population on the territory of Puglia.

Chapter 3

Methodology

This chapter outlines the methodology employed for the various macro-areas into which the work was divided. In the initial phase, a comprehensive bibliographic search was conducted to identify the geometric parameters and masses associated with the two aircraft in question, WhiteKnightTwo and SpaceShipTwo. This was done to create a preliminary database containing the values of the characteristic parameters of the two aircraft. In parallel, the flight phases that compose the mission of the two aircraft were identified. Once the mission profile was derived, it was possible to attribute a geometric configuration of the vehicle to each mission phase. The obtained database was provided as input to the various methods used to analyze the aerodynamics of the two aircraft. The comparison between the obtained results enabled the choice of the most performing method. Parallel to this work, the definition of a propulsive database was also carried out. In conjunction with the aircraft geometric database, the engine data was employed as input for the mathematical model utilized to calculate engine performance. This approach enabled the aerodynamic and propulsive characterization of the system to be obtained. Subsequently, through a study of the Puglia territory and its population density, a potential flight trajectory was delineated using waypoints. Finally, this route was simulated on the trajectory simulation software, resulting in the nominal flight scenario for the two vehicles.

3.1 Geometry methodology

Access to the geometric data of the two aircraft in question is necessary to conduct aerodynamic and propulsive analyses and trajectory simulations with the models mentioned in Chapter 2. Therefore, the initial step was to define the geometric parameters to be determined, distinguishing between the two aircraft. Tables [3.1] and [3.2] present a list of parameters to be identified for both the WhiteKnightTwo and the SpaceShipTwo.

To reconstruct the geometry of the two aircraft, a series of literature searches were conducted initially. The results enabled the identification of the first characteristics for the WhiteKnightTwo and SpaceShipTwo in terms of masses and maximum dimensions.

For WhiteKnightTwo, mass values were identified in literature, including mass at take-off, mass of fuel on board, and mass relative to the payload [13]. These data represent a necessary input for the ASTOS simulations. Furthermore, the bibliography provides information regarding geometric parameters such as the wingspan [3], the length of the fuselage [14] and the geometric parameters of the engine with which the carrier aircraft is equipped, such as the diameter of the nacelle and the length of the nacelle [15].

Data were also found for SpaceShipTwo's maximum mass at launch, empty mass and fuel mass [3]. In terms of geometry, the values for the wingspan and fuselage length of the spacecraft were found [3].

The remaining geometric parameters were identified through an approximate graphical method deemed appropriate for the preliminary analyses in question, since the triptychs of the two aircraft are available in the literature [16] and are shown in Figures (3.1) and (3.2). This method involved hypothesising (such as airfoils) or deriving the parameters using formulae found in the literature.

The airfoils for the wing and the horizontal and vertical tail planes of the two aircraft have been assumed as a first approximation, as this information is not available in the public domain. In particular, symmetrical NACA airfoils were assumed for all surfaces, which facilitates aerodynamic analyses and offers the advantage that the results of experimental analyses carried out on these profiles are available in the literature and can be used to improve the outcomes.

Using this approach, geometric databases were produced for both aircraft, as illustrated in Chapter 4.1.

Parameter	Unit	Parameter	Unit	Parameter	Unit
Wing span	m	Engine number	/	Wing wetted area	m^2
t/c (wing airfoil)	-	Engine overall Length	m	Horizontal tail wetted area	m^2
Wing Ytap(From end of fuselage)	m	Engine fan Diameter	m	Total wetted area	m^2
Wing central span (without fuselage)	m	Engine overall Diameter	m	Mean aerodynamic chord Wing	m
Wing lateral span (without fuselage)	m	Horizontal tail surface	m^2	Mean aerodynamic chord Horizontal tail	m
Wing surface exposed (without fuselage)	m^2	Horizontal tail span	m	Mean aerodynamic chord Vertical tail	m
Wing central span (with fuselage)	m	Horizontal tail sweep angle	deg	MTOW (with SS2)	Kg
Wing lateral span (with fuselage)	m	Horizontal tail root chord	m	Payload weight	kg
wing surface (with fuselage)	m^2	Horizontal tail tip chord	m	Max fuel capacity	kg
Wing Root Chord	m	t/c (Horizontal tail airfoil)	-	Max cruise Mach	/
Wing Tip Chord	m	t/c (Vertical tail airfoil)	/	Structural mass WK2	kg
Wing leading edge sweep angle	deg	Vertical tail root chord	m	Engine Identification	/
Wing trailing edge sweep angle	deg	Vertical tail tip chord	m	Engine TAKE-OFF Thrust	kN
Fuselage length	m	Vertical tail span	m	Engine MAXIMUM CONTINUOUS Thrust	kN
Fuselage diameter	m	Planform area	m^2	Engine BYPASS RATIO	/
Nose length	m	Fuselage wetted area	m^2	Engine Pressure Ratio	/

Table 3.1: Geometric parameters to be identified for WhiteKnightTwo

Parameter	Unit	Parameter	Unit	Parameter	Unit
Wing span	m	Fuselage length	m	Vertical tail length	m
Wing surface	m^2	Nose length	m	Vertical tail sweep	deg
Wing leading edge sweep angle	deg	Fuselage wetted area	m^2	Rocket thrust	pounds
Wing trailing edge sweep angle	deg	Wing wetted area	m^2	Specific impulse	s
Wing root chord	m	Total wetted area	m^2	Burn time	s
Wing tip chord	m	Horizontal tail surface	m^2	Max Launch weight	Kg
t/c (wing airfoil)	/	Horizontal tail length	m	Dry weight	kg
Wing aspect ratio	/	Horizontal tail root chord	m	Max fuel capacity	kg
Fuselage diameter	m	Horizontal tail tip chord	m	Mach Number	

Table 3.2: Geometric parameters to be identified for SpaceShipTwo

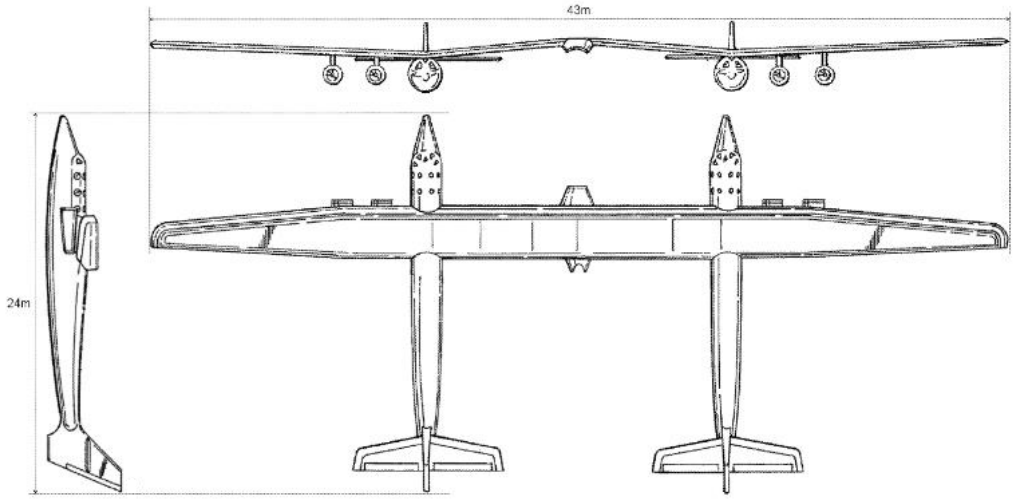

Figure 3.1: Three View Drawing of WhiteKnightTwo. [credits: *[16]*]

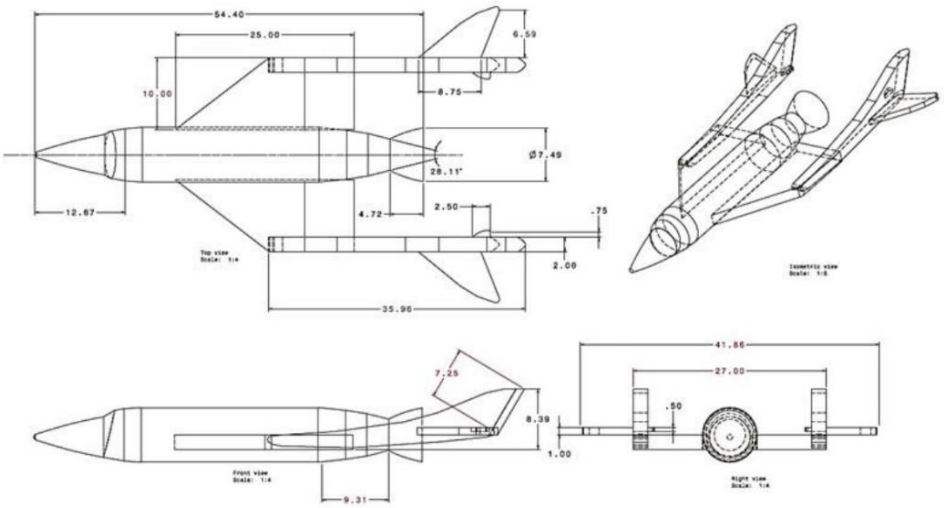

Figure 3.2: Three View Drawing of SpaceShipTwo. [credits: *[16]*]

3.2 Aerodynamic methodology

It is crucial to clarify and identify the configurations adopted by the two aircraft throughout the mission due to establish aerodynamic databases for input into the trajectory simulation software. Specifically, four configurations have been identified:

- Mated Configuration: This configuration involves both the carrier aircraft and the spaceplane together. During the phases preceding release—namely take-off, ascent, and cruise—the two aircraft are in this "mated" configuration. To develop an aerodynamic database for these phases, the additional drag due to the presence of SpaceShipTwo beneath the wing of WhiteKnightTwo must be accounted for. In this configuration, the spaceplane consistently has its landing gear retracted;
- Carrier Standalone Configuration: This configuration involves only the WhiteKnightTwo. Following the release of SpaceShipTwo, the carrier aircraft continues its mission, performing a descent phase followed by an approach phase;
- SpaceshipTwo un-feathered Configuration: In this initial configuration, which encompasses the majority of the mission phases, SpaceShipTwo maintains the feather system at a 0° position;
- SpaceshipTwo feathered Configuration: During the coast feathered and re-entry feathered phases, SpaceShipTwo rotates the feather system to a 60° position. This modification in the aircraft's geometry reduces its speed during re-entry, resulting in a higher drag coefficient for this configuration.

After defining the various configurations that the two aircraft assume during the trajectory, several methods were identified and analysed to construct the corresponding aerodynamic databases.

To obtain a comprehensive understanding of the two aircraft's aerodynamic characteristics in all four configurations, it was first necessary to assess the applicability of the two aerodynamic models proposed by Raymer and Prandtl.

Raymer's method is a valid approach for rapid and preliminary analyses in the subsonic and supersonic flight regimes. It also permits the calculation of aircraft performance in the transonic regime, although with a considerably reduced level of accuracy. It is possible to utilise this model to calculate the performance of all four configurations. In this instance, the drag and lift coefficient values can be determined as a function of altitude, Mach number and angle of attack. For the purpose of the aerodynamic analyses, the contributions to lift and drag due to the presence of flaps and the contributions to drag due to leakage and protuberances, $C_{D_{L\&P}}$, and miscellaneous drag, $C_{D_{misc}}$, have not been considered within the code implementing the Raymer model presented in Chapter 2.2.1, due to a lack of data.

Prandtl's Lifting-line Theory is only valid in the subsonic flight regime. Consequently, it only applies to the mated configuration and in the standalone configuration of WhiteKnightTwo. In both cases, the maximum flight Mach is 0.65. In this case, preliminary analyses are slightly more accurate, but considerably less rapid than with the Raymer model. This is because several two-dimensional analyses of the same airfoil at different flight conditions are required.

The first aircraft configuration to be examined was the coupled configuration, for which both models were applicable. To enhance the reliability of the analysis, a third tool was employed to provide a preliminary assessment of the drag and lift coefficients of the aircraft. The software selected for this purpose is Digital DATCOM.

The software, which is suitable for preliminary and rapid analysis in a subsonic flight regime, necessitates the formulation of several assumptions about the geometry of the fuselage and engines, as it is unable to simulate the twin-fuselage configuration with four engines relative to the WhiteKnightTwo aircraft. In fact, the following assumptions were made: a single fuselage with a diameter twice that of the carrier aircraft fuselage and two engines, each with a diameter twice that of the single engine.

The initial analyses for the three models were conducted for a single case with a flight Mach of 0.64 and an altitude of 13,000 m. The results obtained were then compared, and following appropriate considerations, only one of the three methods was chosen for the aerodynamic analyses, as detailed in Chapter 4.2.

Subsequently, aerodynamic analyses were conducted for a range of Mach number values (0.1 to 0.65), flight altitudes (0 to 15 km) and angle of attack values (-5° to 18°), resulting in the first aerodynamic database for the mated configuration, which was subsequently imported into the ASTOS software.

Subsequently, aerodynamic characterisations were conducted for the SpaceShipTwo in both un-feathered and feathered configurations. In this particular case, only the Raymer model was utilized for the analyses, as it was the only model that was capable of simulating transonic and supersonic flight regimes with an acceptable level of accuracy for preliminary analyses. Moreover, the model enables the rapid generation of multiple analyses as a function of the variation in flight Mach and altitude. In order to further verify the results obtained for the SpaceShipTwo in un-feathered configuration, an aircraft with geometrical characteristics and a mission profile similar to that of the case study was identified in literature. The HOPE-X (Japan) [17] aircraft is an appropriate reference for this specific case study, as it exhibits all required characteristics.

The HOPE-X is an unmanned cargo vehicle designed to reach the International Space Station (ISS). Its aerodynamic configuration features a double delta-type wing. The results of aerodynamic analyses conducted for Mach number values spanning from 0.2 up to Mach 3.5 in conjunction with a range of angles of attack extending from -5° to 30° are available in literature [17], and are shown in Figures (3.4) and (3.5). The graphs enabled us to corroborate the findings of Raymer's model for the SpaceShipTwo un-feathered in the subsonic, transonic and supersonic flight regimes. The results obtained for the spaceplane in the un-feathered configuration were used to verify the drag and lift coefficients for the feathered configuration.

Furthermore, the analyses were conducted for Mach number and altitude values consistent with the mission profile defined in Chapter 3.4. In fact, for the aircraft in the un-feathered configuration, a range of Mach number values from 0.2 to 3.5 was considered, representing the aircraft's maximum speed as reported in the literature. For the feathered configuration, a Mach number range from 0.1 to 2.6 was considered, and an altitude range from 14 km up to 90 km.

Finally, the standalone configuration of the carrier aircraft was subjected to analysis. In this instance, the Raymer model was employed to derive the aerodynamic databases pertaining to the drag and lift coefficient of the aircraft. For the purposes of these analyses, the ranges of Mach number, altitude and angle of attack values considered are identical to those employed in the mated configuration.

The methodology employed involved the acquisition of aerodynamic databases for all four configurations, which assumed the two aircraft throughout the mission. These databases expressed the lift coefficient and drag coefficient as a function of flight Mach, altitude and angle of attack.

Chapter 4.2 presents the graphs of the coefficients for the four configurations.

Figure 3.3: HOPE-X shape: synthetic image [credits: *[17]*]

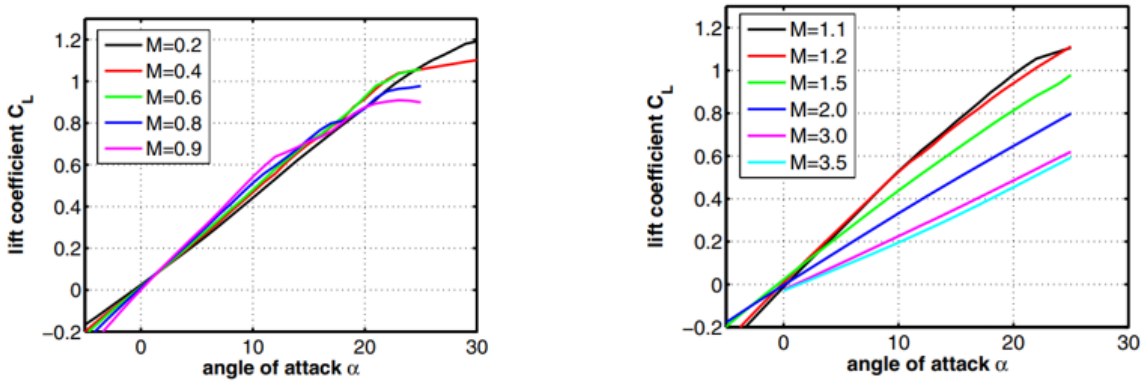

Figure 3.4: Lift coefficient for HOPE-X aircraft as function of the angle of attack for subsonic, transonic and supersonic Mach numbers *[17]*

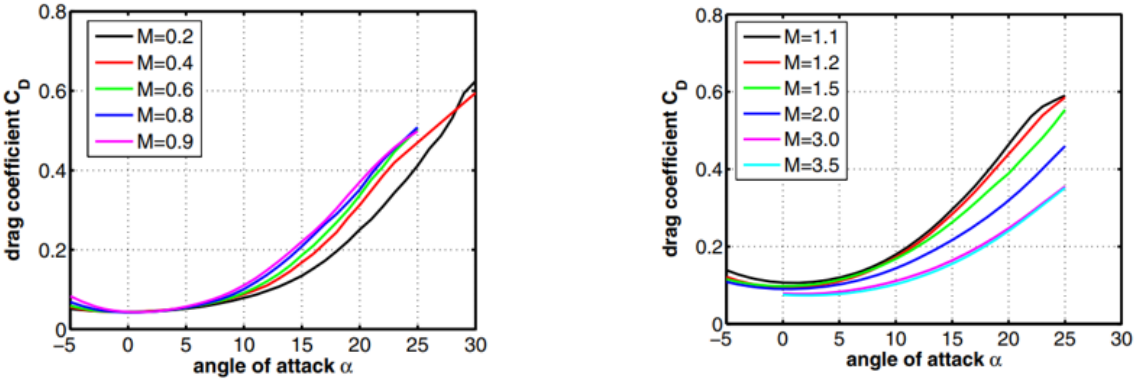

Figure 3.5: Drag coefficient for HOPE-X aircraft as function of the angle of attack for subsonic, transonic and supersonic Mach numbers *[17]*

3.3 Propulsive methodology

To derive the propulsive characterisation, information was initially sought in the literature on the type of engine, the PW308A, mounted on the WhiteKnightTwo aircraft. This data was then provided as input by the code that implements Mattingly's model and which allows us to output the thrust and specific consumption as a function of altitude, flight Mach and throttle. Table [3.3] illustrates the values input to the model for the purpose of calculating the performance of the carrier aircraft engine.

The on-design condition data were provided in accordance with the aircraft mission profile, while the engine characteristics were sourced from the relevant literature [15], [18].

Subsequently, research was conducted into the hybrid rocket engine of the SpaceShipTwo. The RocketMotorTwo is a rocket engine manufactured by Virgin Galactic. The fuel utilised is a hydroxyl-terminated polybutadiene, while the oxidiser is a liquid nitrous oxide [3]. Table [3.4] illustrates the inputs required by the rocket motor trajectory simulation program, as documented in the literature.

Chapter 4.3 presents a graphical representation of the results obtained for the separate-flow turbofan at varying flight Mach numbers, altitudes, and throttle settings.

Input	Value	M.U
Mach Number	0.1 to 0.65	
Flight Altitude	0 to 15000	[m]
Fan Diameter	0.93	[m]
Rated Thrust	30710	[N]
B/P Ratio	4.1	
Pressure Ratio	20.4	

Table 3.3: Input data to calculate Turbofan engine performance *[15], [18]*

Input	Value	M.U
Rocket Motor Thrust	222.4 to 355.8	[kN]
Specific Impulse	250	[sec]
Burn Time	60	[sec]
Propellant Mass	7031	[kg]

Table 3.4: RocketMotorTwo available data

3.4 Mission profile methodology

A comprehensive literature search was conducted to identify the mission profile and thus distinguish the flight phases. Upon the initial discovery of pertinent data, it was possible to distinguish the flight phases and the principal characteristics associated with each of them, as illustrated in Table [3.5].

PHASE	Features	Configuration
Take-off	4 x turbofan engine	WK2+SS2
Climb	4 x turbofan engine; Final altitude: 15km	WK2+SS2
Release	Unpowered; Duration: 8sec	WK2+SS2
Boost	1 x hybrid rocket engine; Final altitude 45 km	SS2
Apogee	Unpowered; Final altitude: 110 km	SS2
Re-entry	Unpowered	SS2
Glide	Unpowered	SS2
Landing SS2	Unpowered	SS2
Descent WK2	4 x turbofan engine	WK2
Landing WK2	4 x turbofan engine	WK2

Table 3.5: Preliminary characterisation of flight phases for the two aircraft

Subsequently, data from previous missions flown by the WhiteKnightTwo and SpaceShipTwo were discovered on the FlightAware flight monitoring platform [19]. This platform provides real-time, historical and predictive flight tracking data and products. FlightAware is an American technology company that can provide flight tracking data through its large network of ADS-B (Automatic Dependent Surveillance-Broadcast) ground stations.

This surveillance technology allows aircraft to determine their position using satellite navigation or other sensors, and periodically transmit their position and other data so that they can be tracked. ADS-B is automatic and does not require any input from the pilot to activate the transmissions. In addition, this surveillance system uses data from the aircraft's navigation system to provide the transmitted data.

The tracking data on FlightAware for the mission carried out on 26 January 2024 by WhiteKnightTwo and SpaceShipTwo from Spaceport America in New Mexico (USA) provided information in terms of altitude and speed as a function of flight time, and the trajectories followed by the aircraft system as shown in Figures (3.6) and (3.7).

This graphical mission representation is the starting point for developing mission analyses and simulations.

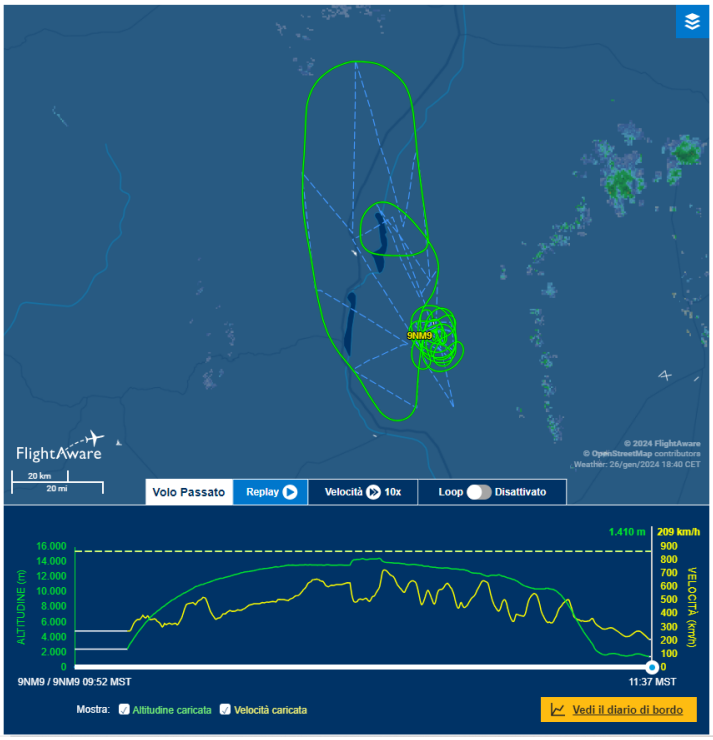

Figure 3.6: Trajectory, altitude and speed profile for WhiteKnightTwo's VGX2 flight *[20]*

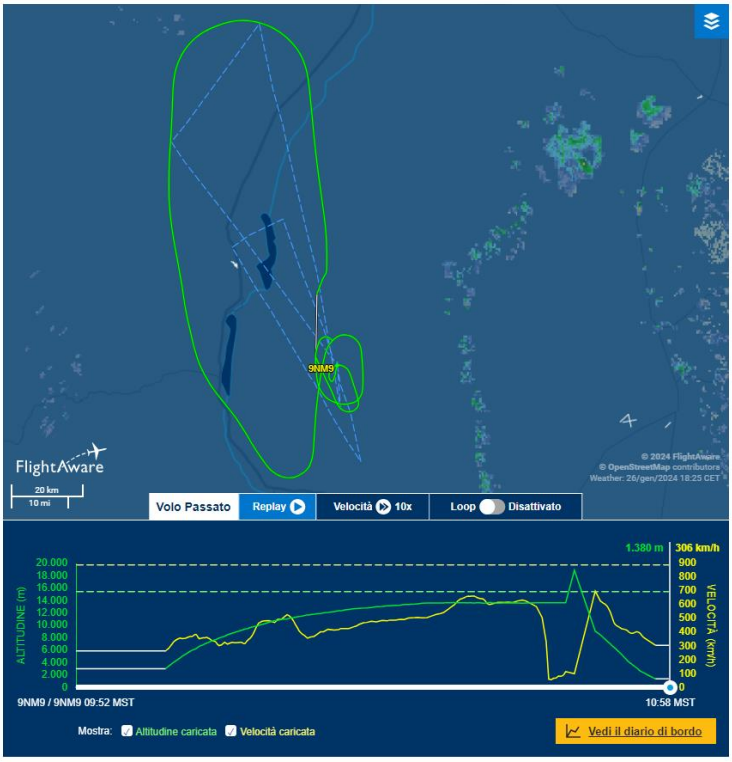

Figure 3.7: Trajectory, altitude and speed profile for SpaceShipTwo VGX3 flight *[21]*

A graphical reconstruction of the trend of speed and altitude over time was possible by starting from the mission data for the VGX2 flight of WK2 and VGX3 of SS2, [20] [21]. This will be used to compare the results of the simulations carried out with ASTOS and to obtain, through successive iterations, a mission profile in terms of speed and altitude as faithful as possible to that realised during the cited mission.

Figures (3.8), (3.9) and (3.10) illustrate the altitude, speed and flight Mach trends as a function of flight time for the VGX2 mission relative to the WhiteKnightTwo aircraft.

Figure (3.8) illustrates the trend of altitude as a function of flight time. The initial phase of the mission comprises the take-off, climb and cruise phases, during which both aircraft, WK2 and SS2, are in the mated configuration. Following approximately 40 minutes of flight, the spaceplane is released. At this point, there is a sudden increase in flight altitude due to the release of the payload, which causes the carrier aircraft to become lighter. Subsequently, the curve follows the descent phase of the carrier aircraft until landing, which will occur at the airport of departure. Figure (3.8) shows that the first value that the flight altitude assumes is distinct from the altitude at which the departure airport is situated, which is 1401 m. This discrepancy is attributable to the absence of data acquisition during the initial minutes of flight, during which the aircraft performs the taxi and take-off phases.

Figure (3.9) illustrates the speed profile as observed during the VGX2 mission. The data pertaining to altitude and flight speed over time was employed to calculate the trend of flight Mach over time, as illustrated in Figure (3.10). The graph allows for the straightforward verification of the maximum Mach number value that can be attained by the aircraft in both the mated configuration and the standalone carrier configuration. This value, which is 0.65, is consistent with the findings presented in the literature. In the initial phase of the mission, the flight Mach number never exceeds 0.6. Following the release of SpaceShipTwo, the speed of the carrier reaches a peak of 0.69, likely due to the instantaneous weight loss caused by the payload release. The velocities during the descent phase exhibit greater fluctuations than those observed during the ascent phase. This is due to the non-straight flight path followed by the aircraft.

Figures (3.11), (3.12) and (3.13) show the trends in altitude, speed and flight Mach as a function of flight time for the SpaceShipTwo VGX3 mission, respectively. Once more, the flight Mach trend was calculated for the entirety of the mission. These data represent the mated configuration of the two aircraft and the subsequent phases of glide and landing, where the SpaceShipTwo has un-feathered configuration. The data available on FlightAware did not permit the coverage of the subsequent phases of the mission, following the release of the SS2 and prior to the glide, due to the high speeds and altitudes reached by the aircraft, which precluded the real-time transmission of the acquired data to the ground via the ADS-B system, which is employed for all other flight phases.

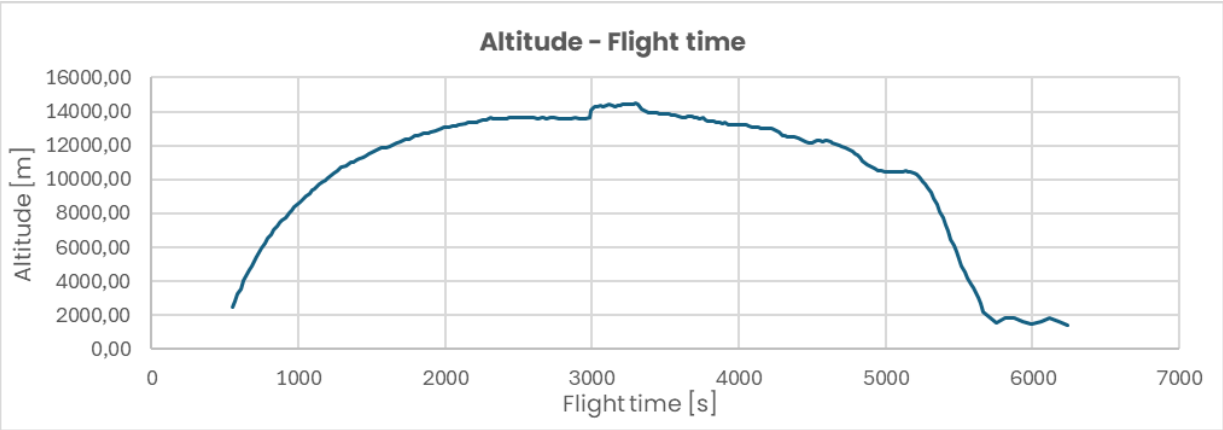

Figure 3.8: Altitude profile as a function of flight time for the VGX2 mission *[20]*

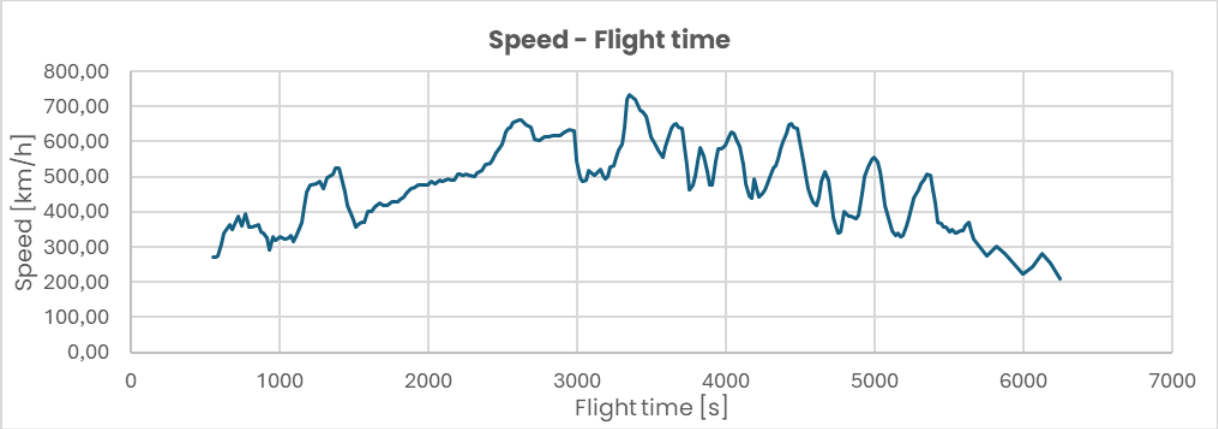

Figure 3.9: Speed profile as a function of flight time for the VGX2 mission *[20]*

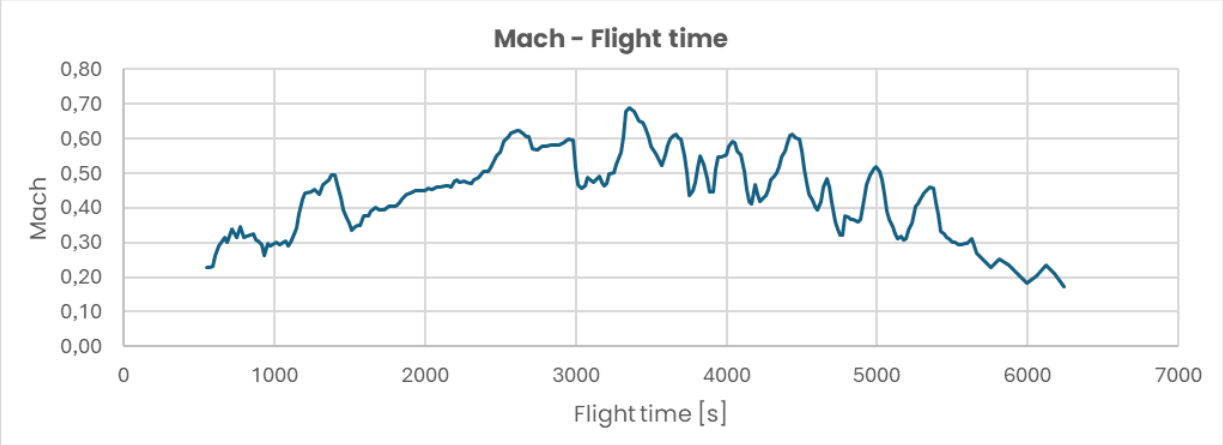

Figure 3.10: Mach profile as a function of flight time for the VGX2 mission *[20]*

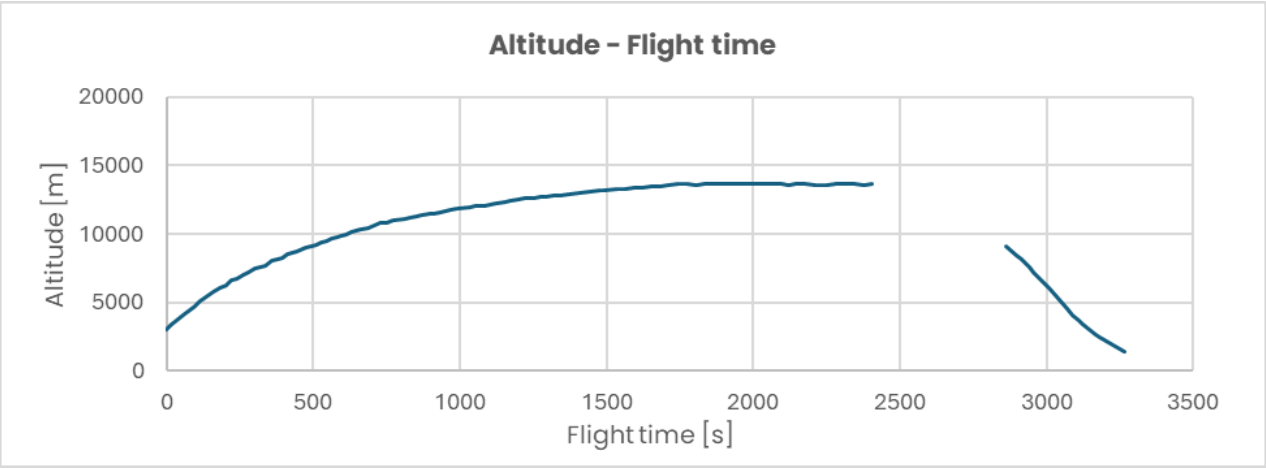

Figure 3.11: Altitude profile as a function of flight time for the VGX2 mission *[21]*

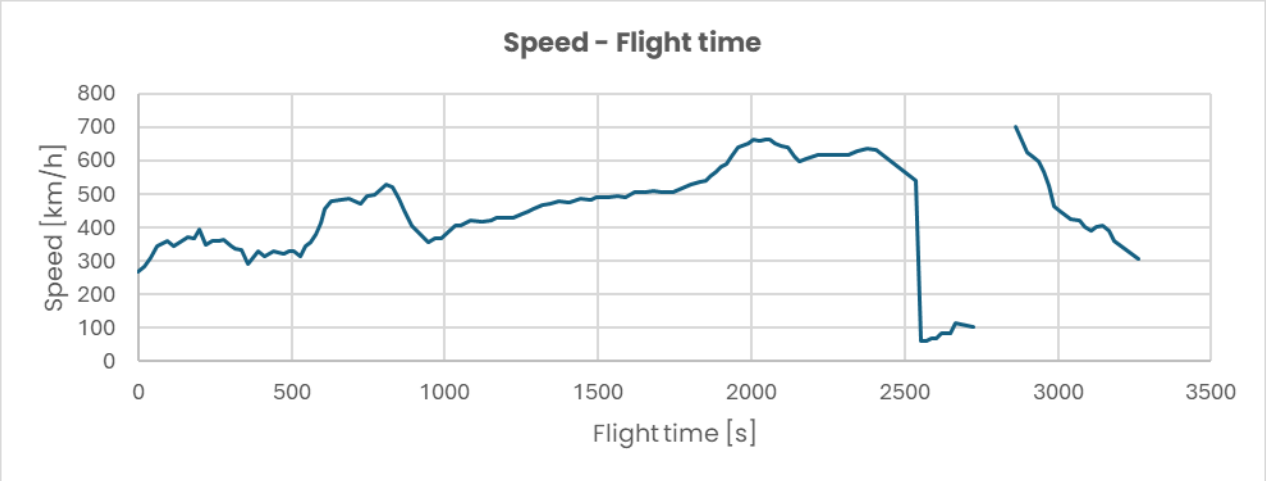

Figure 3.12 Speed profile as a function of flight time for the VGX2 mission *[21]*

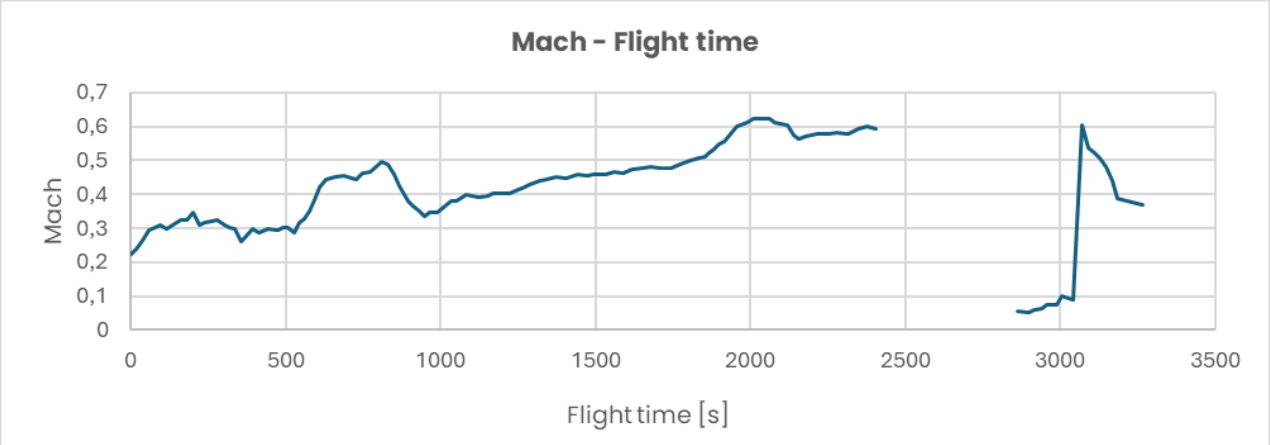

Figure 3.13 Mach profile as a function of flight time for the VGX2 mission *[21]*

Further information was sought and subsequently obtained to address the deficit of data pertaining to the flight phases in which the spaceplane performs its suborbital mission. In particular, a video of the second commercial space flight, Galactic02, performed by the VSS Unity on 10 August 2023 from Spaceport America in New Mexico (USA) was published on Virgin Galactic's YouTube channel [22].

As illustrated in Figure (3.14), this video provides data on the cruise phase in mated configuration and all subsequent post-release phases involving the spaceplane. In particular, the data set comprises the following information:

- Flight time;
- Altitude;
- Flight speed;
- Flight Mach.

Figure 3.14: Example of data shown in the video released by Virgin Galactic for the Spaceplane mission *[22]*

It is crucial to highlight this video's contribution to improving the definition of flight phases. Figures (3.15) and (3.16) illustrate the data obtained for the spaceplane. In particular, these graphs demonstrate the trend of altitude and flight Mach as a function of time for the different flight phases of the SpaceShipTwo mission. In these graphs, the zero-time instant was aligned with the moment of SpaceShipTwo's release from the carrier aircraft. The video images were useful in breaking down the mission accomplished by SpaceShipTwo into more detailed phases. As can be seen from the Figures (3.15) and (3.16), the phases that characterise the mission profile of SpaceShipTwo are:

- Release phase (SS2 in un-feathered configuration);
- Boost phase (SS2 in un-feathered configuration);
- Coast phase (SS2 in un-feathered configuration);
- Coast phase (SS2 in feathered configuration);
- Re-entry phase (SS2 in feathered configuration);
- Re-entry phase (SS2 in un-feathered configuration);
- Glide phase (SS2 in un-feathered configuration);
- Landing phase (SS2 in un-feathered configuration).

The data presented in the Figures (3.15) and (3.16) do not fully encompass the glide phase of the mission. This is due to the absence of information about this phase. By integrating the data from the various sources, the complete flight profile in terms of altitude and Mach as a function of time was reconstructed for the SpaceShipTwo aircraft, as illustrated in Figures (3.17) and (3.18). The graphs were constructed using data from FlightAware (in blue) for the initial phases and data extrapolated from the video content published by Virgin Galactic (in orange) for the subsequent phases involving the SpaceShipTwo. About the portion of the graph about the glide phase of spaceplane, which extends from an altitude of 10,000 m up to approximately 3,000 m, the absence of data within the video was compensated for by the data present on FlightAware, given that the ADS-B surveillance system resumes sending data to the ground station from an altitude of 9,000 m. Table [3.6] provides a comprehensive overview of all flight phases, including the respective aircraft competing in each phase. Additionally, the table presents the initial and final flight conditions, a brief description, and the total duration of each mission phase.

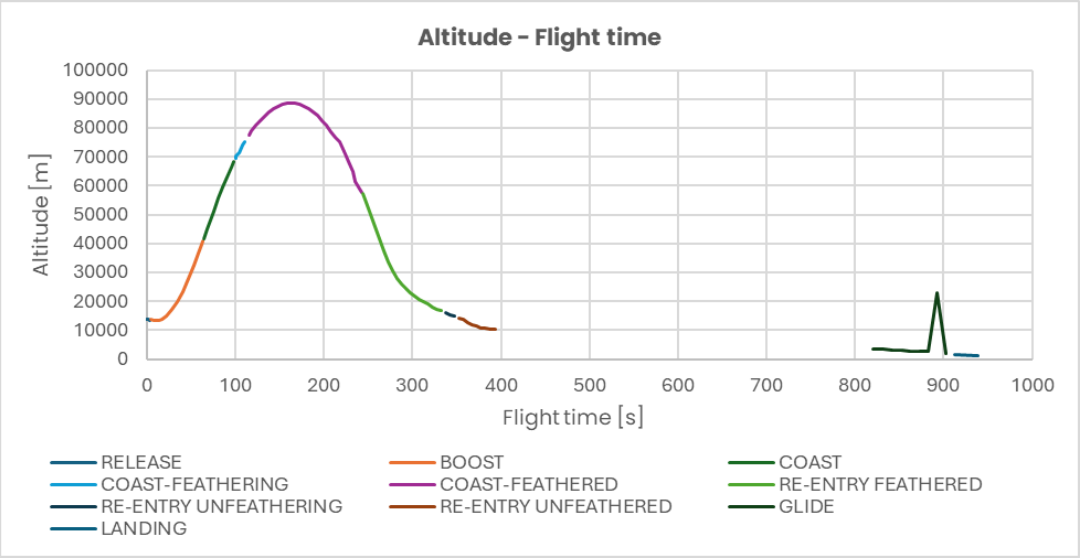

Figure 3.15: Altitude profile derived from the Virgin Galactic video *[22]*

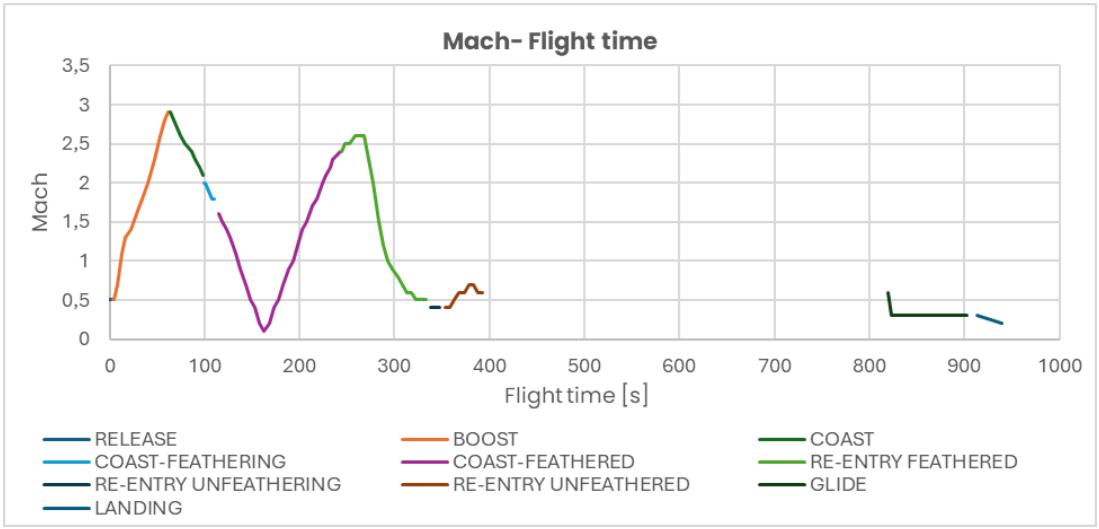

Figure 3.16 Mach profile derived from the Virgin Galactic video *[22]*

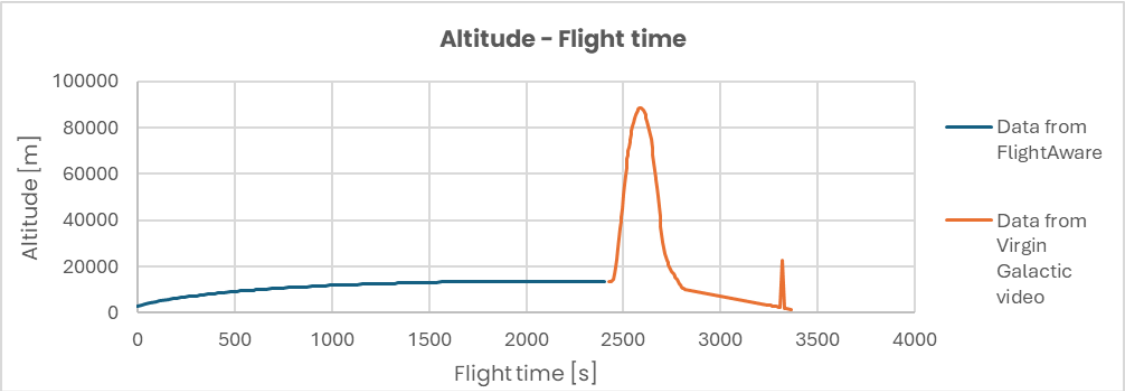

Figure 3.17: Altitude profile derived from both FlightAware data (VGX3) *[21]* and Virgin Galactic video *[22]*

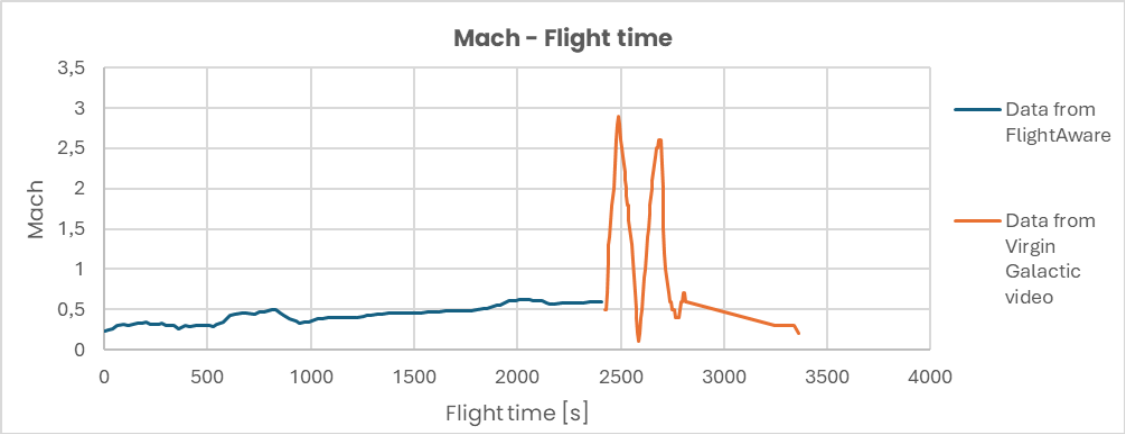

Figure 3.18: Mach profile derived from both FlightAware data (VGX3) *[21]* and Virgin Galactic video *[22]*

Phase	Vehicles	Initial condition	Final condition	Description	Duration
PRE-FLIGHT	WK2+SS2	Mission plan, boarding, check list..	Ready to departure		Hours to days
TAXI	WK2+SS2	Ready to departure	Ready to take-off	From gate to take-off runway	5/10 minutes
TAKE-OFF	WK2+SS2	Runway entry	Detachment from runway	Accelerate from 0 to take-off speed	1 minute
CLIMB	WK2+SS2	Detachment from runway	Altitude of around 15 km	With spiral trajectory it reaches the final altitude	40 minutes
CRUISE	WK2+SS2	Reached 15 km of altitude with Mach number of around 0.6	Level flight at 15 km	It performs a cruise phase to reach optimal conditions for release	5 minutes
RELEASE	SS2	Level flight at 15 km	Complete separation from WK2	SS2 separates from WK2	3 seconds
BOOST	SS2	Free flight of SS2	Mach 2.9 at an altitude of around 40 km.	SS2 rocket engine is activate to perform the ascent	1 minute
COAST UNFEATHERED	SS2	Mach 2.9 at an altitude of around 40 km.	Altitude of around 70 km	SS2 rocket engine is turned off and the vehicle continues to climb in free flight condition	0,5 minutes
COAST FEATHERED	SS2	SS2 feathering	Altitude of around 57 km	SS2 reached apogee at 88 km and then starts the re-entry manouvre	2/3 minutes
RE-ENTRY FEATHERED	SS2	Altitude of around 57 km	Altitude of around 16 km	SS2 decelerates	1/2 minutes
RE-ENTRY UNFEATHERED	SS2	SS2 unfeathering	Altitude of around 10 km	SS2 decelerates with high angle of attack to increase drag	0,5 minutes
GLIDE	SS2	Altitude of around 10 km	Reaches landing runway	Subsonic descent towards the landing airport	8/9 minutes
LANDING SS2	SS2	Reaches landing runway	SS2 speed at 0 km/h	SS2 touches the runway and decelerates to a complete stop	1 minute
DESCENT WK2	WK2	Complete separation from SS2	Reaches landing runway	Subsonic descent towards the landing airport	40 minutes
LANDING WK2	WK2	Reaches landing runway	WK2 speed at 0 km/h	WK2 touches the runway and decelerates to a complete stop	1 minute

Table 3.6: Final characterisation of flight phases for the two aircraft

Following the study of the mission's flight phases and the analysis of the altitude and speed profiles for each phase, the aircraft's trajectory was analysed. Firstly, the Grottaglie Airport was subjected to analysis, with particular attention paid to its position in terms of coordinates and altitude. These parameters were deemed necessary to simulate a georeferenced route on ASTOS. Table [3.7] presents the parameter values for the two runways at the airport.

RUNWAY	LATITUDE	LONGITUDE	ALTITUDE [m]	LENGTH [m]
17	40°31'23.19''	17°24'06,54''	64.66	3200
35	40°29'56,42''	17°24'29,38''	61,83	3200

Table 3.7 Grottaglie Airport runways information *[23]*

Subsequently, the VFR area map for Brindisi, as depicted in Figure (3.19), was obtained from the AIP (Aeronautical Information Publication) section of the portal of ENAV (Ente Nazionale per Assistenza al Volo), a company responsible for the navigation of aircraft in Italian airspace. Preliminary selections were made about the designated airspace zones for the mission. Figures (3.20) and (3.21) illustrate the areas affected by the suborbital mission. In light of these preliminary considerations, it was thus resolved to examine the following areas: R315, R316, R317, R405/B, R405/D, TSA455A and TSA455B.

Zones R315, R316, R317, R405/B and R405/D are designated as 'Restricted Areas'. These are defined as portions of airspace within which flight is subject to compliance with specific conditions, such as circumstances, periods or authorisations. In order to ascertain the conditions governing operations in these areas, the AIP was consulted, where the requisite information can be found. The table [3.8] presents the data extracted from the AIP portal in the section "ENR 5.1.2 ZONE REGOLAMENTATE".

TSA455A and TSA455B are designated as 'Temporary Reserved Areas'. As defined in ENAC's "Regole dell'aria Italia" [24], a TSA is "Airspace of defined dimensions, normally under the jurisdiction of an aeronautical authority, temporarily segregated by common agreement for the specific use by another aeronautical authority, and through which the transit of other traffic is not permitted". Table [3.9] presents the data obtained from the AIP portal in the section "ENR 5.1.4 ZONE TEMPORANEAMENTE RISERVATE".

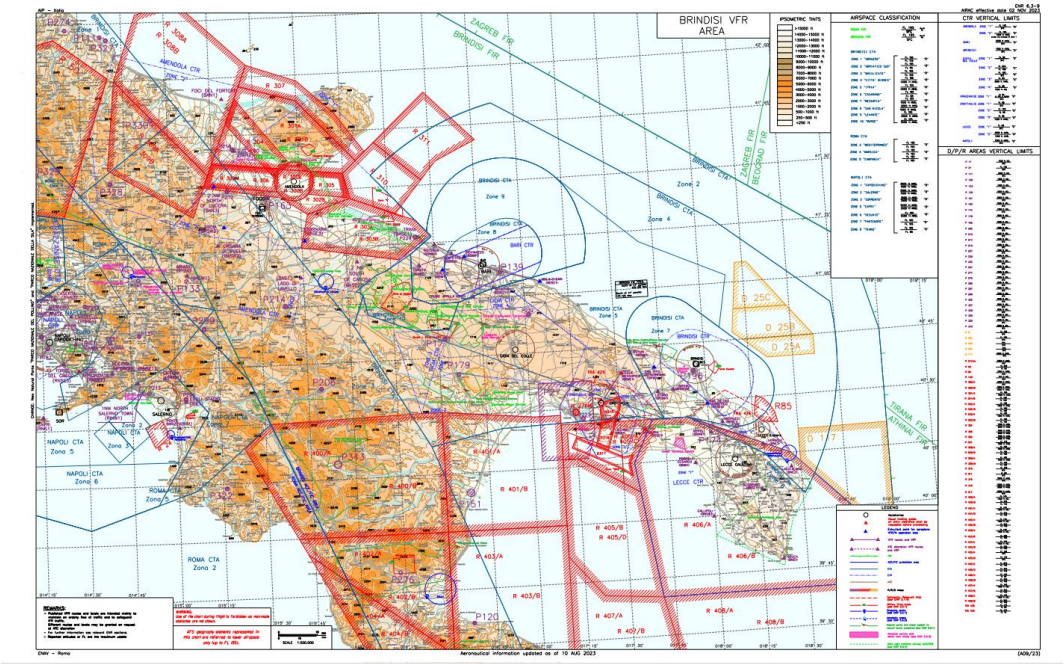

Figure 3.19: Brindisi VFR area from ENAV portal

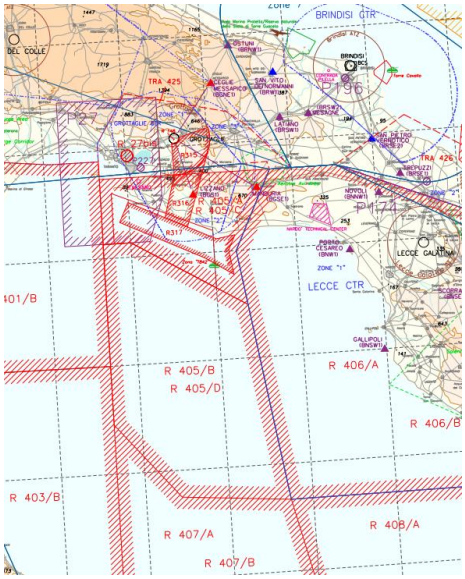

Figure 3.20: Magnified view Brindisi VFR area

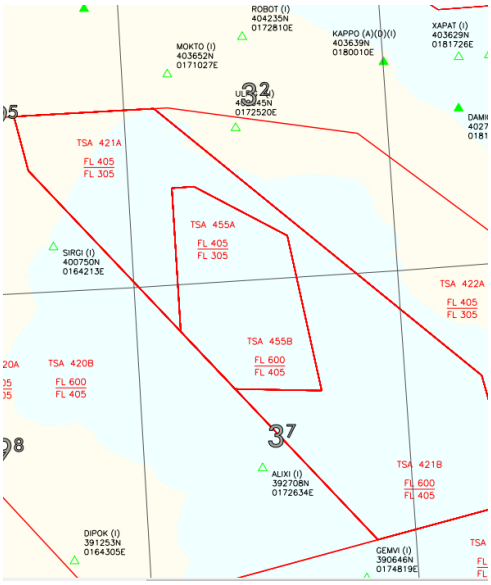

Figure 3.21: Free route airspace chart

Identification,name and Lateral Limits	Upper Limit Lower Limit	Type of activity	Remarks
LI R315 – Grottaglie Area 1B 40°26'00"N 017°23'39"E; 40°30'25"N 017°23'32"E; 40°30'33"N 017°24'27"E; then arc of circle in anti-clockwise direction radius 1.5 NM centred on 40°31'40"N 017°23'08"E till point 40°31'14"N 017°25'01"E; 40°32'20"N 017°30'18"E then arc of circle in clockwise direction radius 5.0 NM centred on 40°31'00"N 017°23'59"E till point of origin.	5000ft AMSL --- SFC	Civil unmanned aircraft testing activity	1) HR: Active upon notice by NOTAM 2) Other air traffic prohibited during periods of effective occupation, except for aircraft previously authorized by ENAC 3) Information on effective occupation may be requested to Grottaglie APP/TWR and Brindisi ACC/FIC.
LI R316 - Grottaglie Corridoio B 40°20'11"N 017°21'29"E; 40°26'00"N 017°23'39"E then arc of circle in anti-clockwise direction radius 5.0 NM centred on 40°31'00"N 017°23'59"E till point 40°29'24"N 017°30'12"E; 40°18'43"N 017°25'28"E; to point of origin.	5000ft AMSL --- 2000ft AMSL	Civil unmanned aircraft testing activity	1) HR: Active upon notice by NOTAM 2) Other air traffic prohibited during periods of effective occupation 3) Information on effective occupation may be requested to Grottaglie APP/TWR and Brindisi ACC/FIC.
LI R317 - Grottaglie Area 2B 40°22'37"N 017°14'56"E; 40°16'49"N 017°30'34"E; 40°17'12"N 017°33'57"E; 40°15'09"N 017°32'39"E; 40°11'43"N 017°33'20"E; 40°14'14"N 017°28'18"E; 40°19'55"N 017°13'13"E; to point of origin.	5000ft AMSL --- SFC	Civil unmanned aircraft testing activity	1) HR: Active upon notice by NOTAM 2) Other air traffic prohibited during periods of effective occupation 3) Information on effective occupation may be requested to Grottaglie APP/TWR and Brindisi ACC/FIC.
LI R405/B - Taranto 40°16'57"N 017°09'56"E; 40°17'00"N 017°15'00"E; 40°07'25"N 017°35'31"E; 39°40'00"N 017°41'00"E; 39°41'16"N 017°21'27"E; 39°51'50"N 017°10'00"E; to point of origin.	FL145 --- SFC	Firing exercises (Military air activity)	1) HR: H24; HOL excluded 2) Responsible ATS Unit: Brindisi SCCAM 3) Procedures for crossing see ENR 5.1
LI R405/D - Taranto 40°16'57"N 017°09'56"E; 40°17'00"N 017°15'00"E; 40°07'25"N 017°35'31"E; 39°40'00"N 017°41'00"E; 39°41'16"N 017°21'27"E; 39°51'50"N 017°10'00"E; to point of origin.	FL245 --- FI145	Firing exercises (Military air activity)	1) HR: H24; HOL excluded 2) Responsible ATS Unit: Brindisi SCCAM 3) Procedures for crossing see ENR 5.1

Table 3.8: data from the AIP portal section "ENR 5.1.2 ZONE REGOLAMENTATE"

Identification,name and Lateral Limits	Upper Limit Lower Limit	Type of activity	Remarks
LI TSA455A - Grottaglie 2 40°16'57"N 017°09'56"E; 40°17'00"N 017°15'00"E; 40°07'25"N 017°35'31"E; 39°40'00"N 017°41'00"E; 39°41'16"N 017°21'27"E; 39°51'50"N 017°10'00"E; to point of origin.	FL405 --- fl305	Firing exercises	1) 'AMC manageable' zone 2) HR: MON-FRI 0500-2200 (0400-2100); SAT 0500-1300 (0400-1200); HOL excluded 3) Responsible ATS Unit: Brindisi SCCAM 4) Entry to all air traffic not directly participating in the activities is prohibited 5) When the zone is active, LI TSA421A zone can not be planned and used 6) Reservation of the area with at least two days in advance 7) Tactical coordination via cable with Brindisi SCCAM is required, to confirm or cancel the activity
LI TSA455B - Grottaglie 2 High 40°16'57"N 017°09'56"E; 40°17'00"N 017°15'00"E; 40°07'25"N 017°35'31"E; 39°40'00"N 017°41'00"E; 39°41'16"N 017°21'27"E; 39°51'50"N 017°10'00"E; to point of origin.	FL600 --- FL405	Firing exercises	1) 'AMC manageable' zone 2) HR: MON-FRI 0500-2200 (0400-2100); SAT 0500-1300 (0400-1200); HOL excluded 3) Responsible ATS Unit: Brindisi SCCAM 4) Entry to all air traffic not directly participating in the activities is prohibited 5) When the zone is active, LI TSA421B zone can not be planned and used 6) Reservation of the area with at least two days in advance 7) Tactical coordination via cable with Brindisi SCCAM is required, to confirm or cancel the activity

Table 3.9: data from the AIP portal section "ENR 5.1.4 ZONE TEMPORANEAMENTE RISERVATE"

In order to identify a flight corridor for the phases in which the two aircraft fly over the land, namely those following take-off and those preceding landing, a survey of the Puglia territory was carried out using QGIS software and ISTAT data relating to the territorial bases and census for the Puglia region. Subsequently, by combining knowledge of each area's shape, area and resident population, it became possible to calculate the population density per km² over the entirety of Puglia region. Figure (3.22) illustrates the distribution of population density across the Puglia territory. Figure (3.23) provides a magnified view of the same parameter near the Grottaglie Airport.

The distribution of the population density parameter was taken into account when defining a flight corridor via waypoints using Google's MyMaps tool, as illustrated in Figure (3.24). The resulting corridor was subsequently integrated as a layer on the map with population density indicators on QGIS software (see

Figure (3.25)). This validated the hypothesis that the proposed route would avoid overflight of densely populated centres.

Once the route that the two aircraft in the mated configuration must follow after take-off was identified, and the zones in which the two aircraft can fly were established, simulations were initiated for the flight phases in which the two aircraft are in the mated configuration, assuming that the aircraft performs a climb following a spiral profile. The results were subjected to analysis and improvement through successive iterations, to identify any discrepancies between the altitude and speed trends as a function of time and those found in the literature. Two distinct trajectories were simulated for the initial stages of the mission. The first envisages the SpaceShipTwo's release in the direction of the Taranto, while the second is oriented towards the Ionian Sea. These trajectories can be observed in Chapter 4.4. The decision to simulate these two trajectories was based on the rationale that the trajectory in the direction of the Ionian Sea is the one that is expected to better meet the safety criteria. The trajectory in the direction of Taranto was simulated to validate the results, given that in terms of distances covered and flight time, it is more similar to the mission used to verify the results.

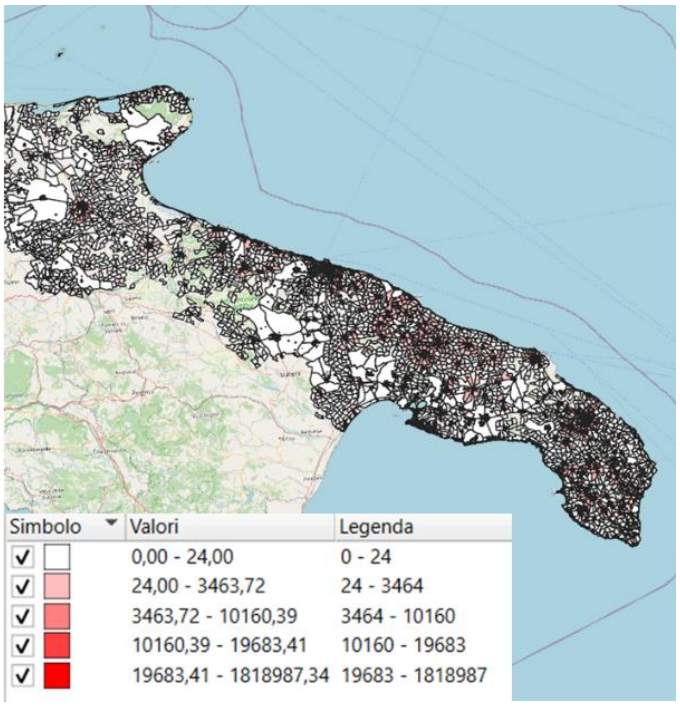

Figure 3.22: Distribution of population density across the Puglia territory from QGIS

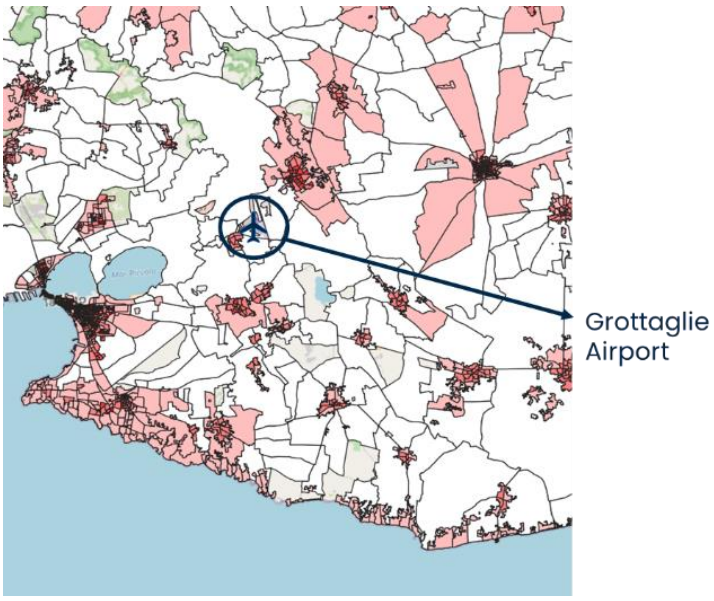

Figure 3.23: Magnified view of distribution of population density near the airport

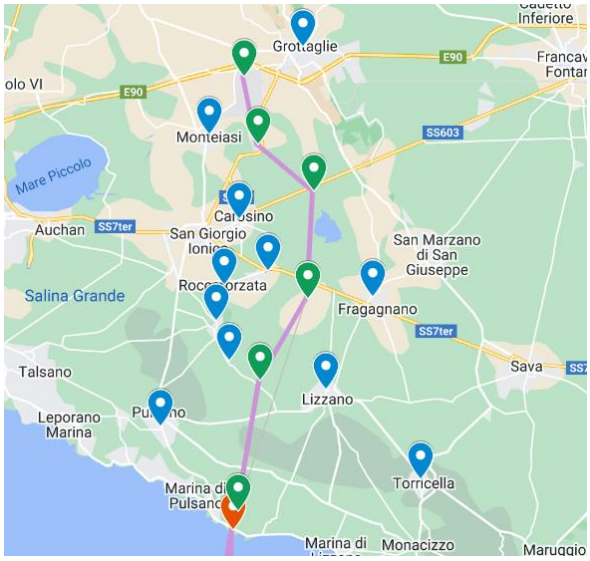

Figure 3.24: Preliminary flight corridor defined by waypoints

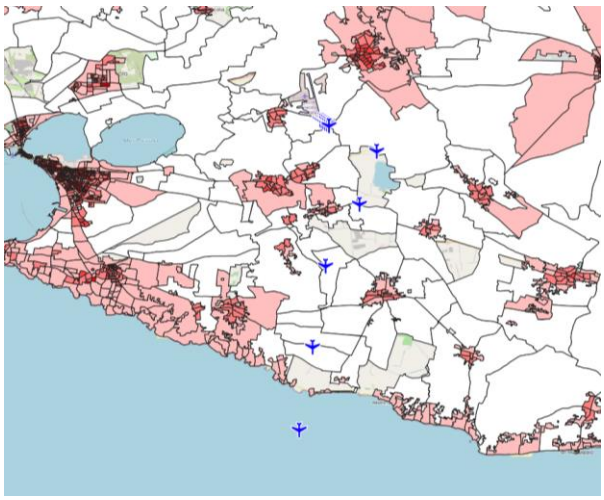

Figure 3.25: QGIS analysis for the preliminary flight corridor

Chapter 4

Results

This chapter aims to present and analyse the results obtained. In particular, the geometric databases for the WhiteKnightTwo and SpaceShipTwo are presented, along with the aerodynamic databases obtained using the three different methods for the mated configuration. Additionally, the aerodynamic database is provided for the Standalone, SpaceShipTwo un-feathered, and SpaceShipTwo feathered configurations respectively, along with the propulsion database for the carrier aircraft's turbofan engine, the data from the spaceplane's hybrid rocket motor and the results of simulations performed on ASTOS, together with a comparison with data from the literature.

4.1 Geometry results

The Tables [4.1] and [4.2] present the parameters for WhiteKnightTwo and SpaceShipTwo, respectively. These have been derived as explained in Chapter 3.1, from existing literature, with the use of mathematical formulae or using of assumptions.

Parameter		Unit	Parameter		Unit	Parameter		Unit
Wing span	43	m	Engine number	4	/	Wing wetted area	269.21	m^2
t/c (wing airfoil)	0.15	-	Engine overall Length	2.183	m	Horizontal tail wetted area	29.39	m^2
Wing Ytap(From end of fuselage)	2.71	m	Engine fan Diameter	0.93	m	Total wetted area	528.02	m^2
Wing central span (without fuselage)	13.33	m	Engine overall Diameter	1.229	m	Mean aerodynamic chord Wing	2.63	m
Wing lateral span (without fuselage)	13.09	m	Horizontal tail surface	14.16	m^2	Mean aerodynamic chord Horizontal tail	1.364	m
Wing surface exposed (without fuselage)	117.54	m^2	Horizontal tail span	7.55	m	Mean aerodynamic chord Vertical tail	1.24	m
Wing central span (with fuselage)	16.81	m	Horizontal tail sweep angle	11	deg	MTOW (with SS2)	31840	Kg
Wing lateral span (with fuselage)	13.09	m	Horizontal tail root chord	1.759	m	Payload weight	13600	kg
wing surface (with fuselage)	129.74	m^2	Horizontal tail tip chord	0.969	m	Max fuel capacity	9700	kg
Wing Root Chord	3.149	m	t/c (Horizontal tail airfoil)	0.12	-	Max cruise Mach	0.65	/
Wing Tip Chord	1.5	m	t/c (Vertical tail airfoil)	0.12	/	Structural mass WK2	8986	kg
Wing leading edge sweep angle	3	deg	Vertical tail root chord	1.088	m	Engine Identification	PW308A	/
Wing trailing edge sweep angle	10	deg	Vertical tail tip chord	1.4	m	Engine TAKE-OFF Thrust	30.71	kN
Fuselage length	24	m	Vertical tail span	3.68	m	Engine MAXIMUM CONTINUOUS Thrust	30.71	kN
Fuselage diameter	2.28	m	Planform area	129.74	m^2	Engine BYPASS RATIO	4.1	/
Nose length	3	m	Fuselage wetted area	229.42	m^2	Engine Pressure Ratio	20.4	/

Table 4.1: Preliminary Geometric Database for WhiteKnightTwo

Parameter		Unit	Parameter		Unit	Parameter		Unit
Wing span	8.3	m	Fuselage length	14.32	m	Vertical tail length	2.55	m
Wing surface	47.1	m^2	Nose length	3	m	Vertical tail sweep	22	deg
Wing leading edge sweep angle	34	deg	Fuselage wetted area	115.414	m^2	Rocket thrust	50000 to 85000	pound s
Wing trailing edge sweep angle	0	deg	Wing wetted area	42.524	m^2	Specific impulse	250	s
Wing root chord	7.62	m	Total wetted area	157.94	m^2	Burn time	60	s
Wing tip chord	3.7359	m	Horizontal tail surface	5.93	m^2	Max Launch weight	13154	Kg
t/c (wing airfoil)	0.12	/	Horizontal tail length	2.00	m	Dry weight	6123	kg
Wing aspect ratio	1.62	/	Horizontal tail root chord	2.66	m	Max fuel capacity	7031	kg
Fuselage diameter	2.28	m	Horizontal tail tip chord	0.3	m	Mach Number	0.2 to 3.5	

Table 4.2: Preliminary Geometric Database for SpaceShipTwo

4.2 Aerodynamic results

4.2.1 Mated Configuration results

The initial findings pertain to the mated configuration. As previously outlined in Chapter 3.2, the outcomes of the three aerodynamic models discussed above were examined for this configuration. These were Raymer's Method, Prandtl's Lifting-line Theory and Digital DATCOM software.

The results obtained using the Raymer model for aerodynamic characterisation are illustrated in Figures (4.1) and (4.2). The graphs were generated by introducing the following variations in flight conditions:

- Mach number between 0.04 and 0.64;
- Altitude between 0 and 15000m;
- Angle of attack between -8° and 24°.

On this basis, it becomes possible to obtain lift and drag coefficients as a function of angle of attack, flight Mach, and altitude.

Figures (4.3) and (4.4) show the results obtained using Prandtl's Lifting-line Theory, once more expressed in terms of lift and drag coefficient. In these figures, only one curve is presented for flight conditions with Mach 0.64 and an altitude of 13000 metres.

Figures (4.5) and (4.6) represent the results obtained using the Digital DATCOM Software. The analyses were carried out for the same flight condition used in Prandtl model.

Figures (4.7) and (4.8) show the comparison between the aerodynamic results obtained with the three different methods. The comparison was made considering the same flight conditions of Mach 0.64 and flight altitude of 15000m for each method.

Due to the assumptions made about the geometry of the aircraft within Digital DATCOM, expressed in Chapter 3.1, the results obtained with this method differ from those obtained with the Raymer and Prandtl models.

The results obtained with the two semi-empirical mathematical models show a similar trend. However, as can be seen from the Figures (4.7) and (4.8), Raymer's model tends to overestimate the lift coefficient and underestimate the drag coefficient concerning Prandtl's drag line theory. In particular, for an angle of attack of 24°, the differences in the values of the lift and drag coefficients are the greatest. Since we do not have enough information to know which of the two estimates is more accurate, and since the results obtained with these two methods are sufficiently similar for small values of the angle of attack, the choice of model to be used to derive the aerodynamic databases for the mated configuration was made taking into account the computational cost. In fact, the Lifting-line Theory has a much higher computational cost than the Raymer model; this is due to the strong dependence of this method on the two-dimensional analyses that must be carried out on the aerodynamic airfoils of the wing, the horizontal stabilizer and the vertical stabilizer, depending on the flight condition in which the aircraft is operating.

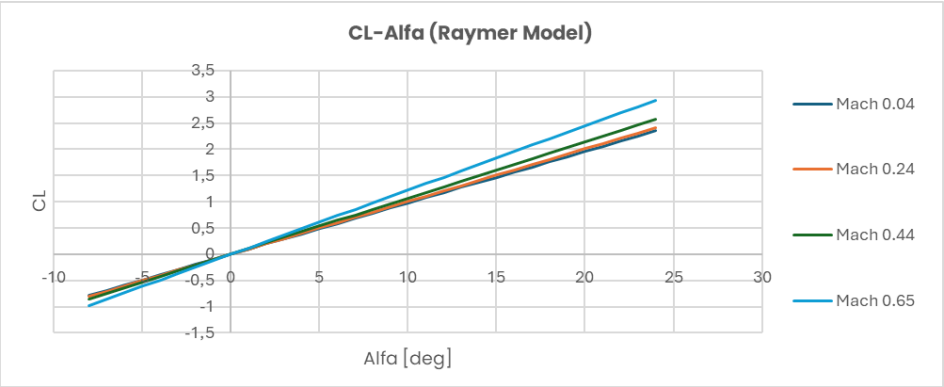

Figure 4.1: Result for lift coefficient as a function of Mach number and angle of attack from Raymer Model

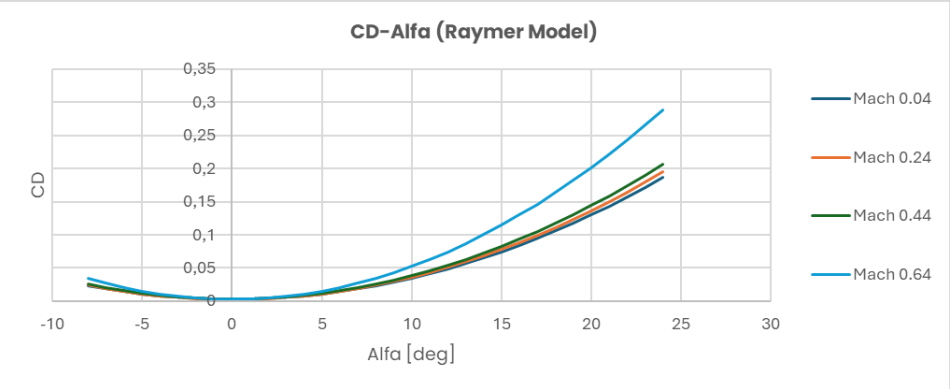

Figure 4.2: Result for drag coefficient as a function of Mach number and angle of attack from Raymer Model

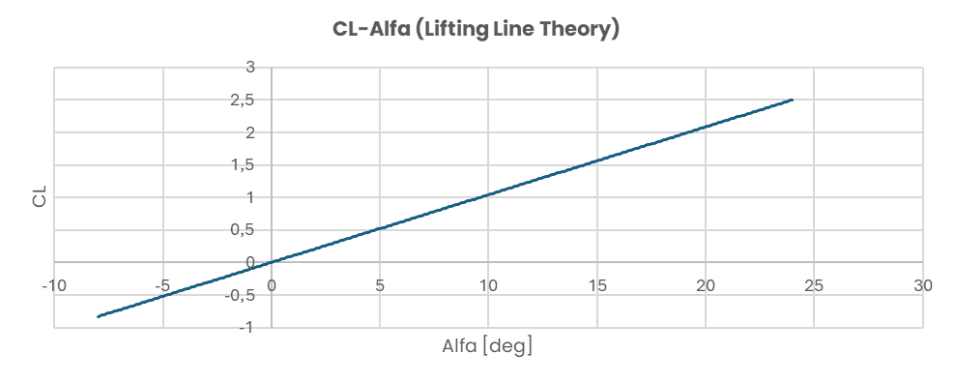

Figure 4.3: Result for lift coefficient as a function of angle of attack from Lifting-line Theory

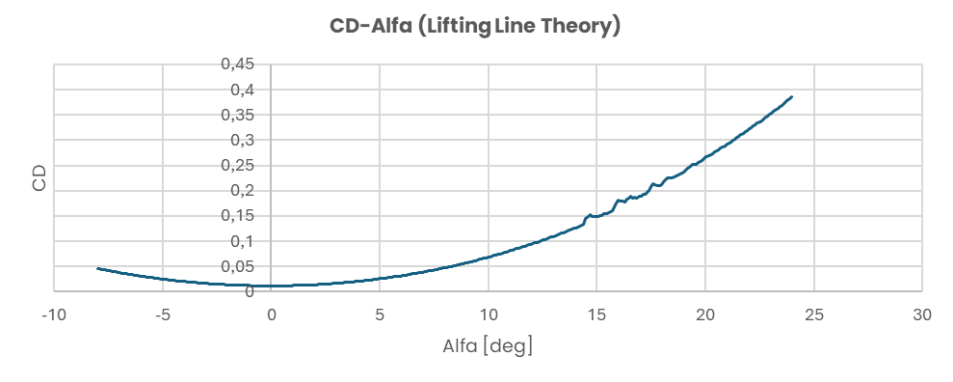

Figure 4.4: Result for drag coefficient as a function of angle of attack from Lifting-line Theory

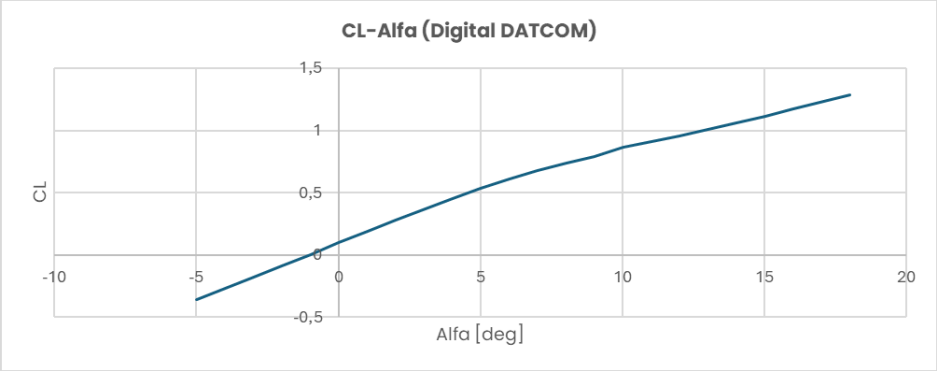

Figure 4.5: Result for lift coefficient as a function of angle of attack from Digital DATCOM

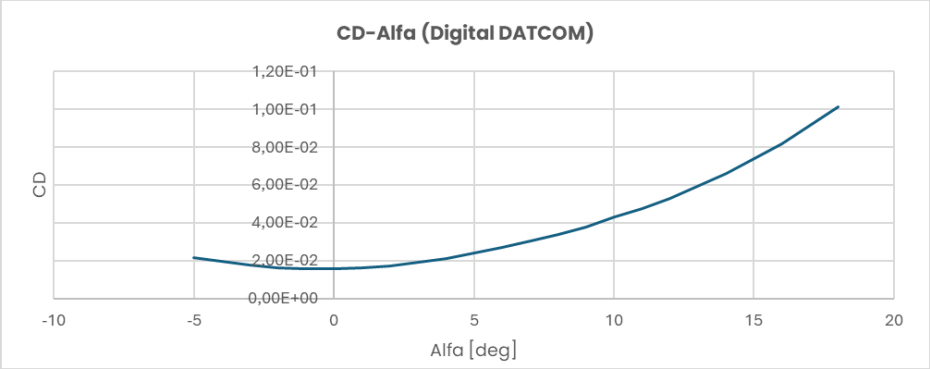

Figure 4.6: Result for drag coefficient as a function of angle of attack from Digital DATCOM

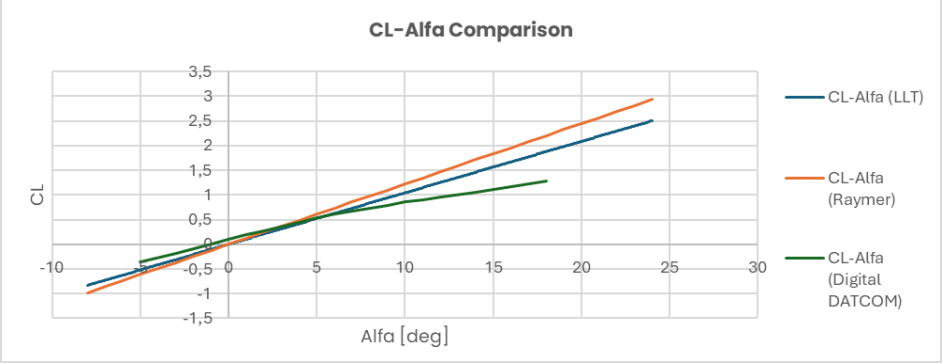

Figure 4.7: Comparison of $C_L - \alpha$ curves obtained with the three aerodynamic models for Mach 0.64 and altitude of 13 km

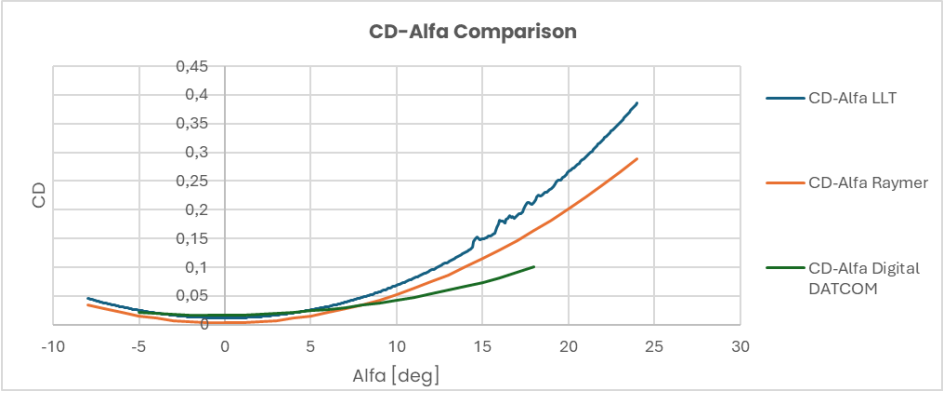

Figure 4.8: Comparison of $C_D - \alpha$ curves obtained with the three aerodynamic models for Mach 0.64 and altitude of 13 km

4.2.2 SpaceShipTwo un-feathered Configuration result

The second configuration for which aerodynamic characterisation was carried out is the un-feathered SpaceShipTwo. Figures (4.9), (4.10), (4.11) and (4.12) show the results of the analysis performed with the Raymer model. This model was chosen because the range of speeds at which SpaceShipTwo flies in the un-feathered configuration is wide, from Mach 0.2 to Mach 3.5, and the Raymer model is capable of covering all these flight regimes.

Figures (4.9) and (4.11) show the lift and drag coefficient results for the subsonic and initial transonic flight regimes, while figures (4.10) and (4.12) show the results for the transonic and supersonic flight regimes. This subdivision of the graphs by flight regime has been made to facilitate comparison with the results of the aerodynamic analyses for the HOPE-X aircraft shown in Chapter 3.2 Figures (3.4) and (3.5).

The comparison between the results obtained and the data found in literature showed that the Raymer model concerning the lift coefficient:

- Overestimates the results in the transonic regime (from Mach 0.9 to Mach 1.5);
- Returns acceptable results in the subsonic and supersonic regime.

As far as the drag coefficient is concerned, we have that Raymer's model:

- Underestimates the results in the subsonic regime;
- Overestimates the results in the transonic regime;
- Returns acceptable results in the cruise regime.

4.2.3 SpaceShipTwo feathered Configuration result

The results obtained for the SpaceShipTwo feathered configuration are displayed in Figures (4.13), (4.14), (4.15) and (4.16). Furthermore, the results were obtained using Raymer's method, as flight conditions ranging from subsonic to supersonic are also applied to this configuration. It should be noted that the same considerations apply as for Raymer's model applied to the un-feathered configuration of the SpaceShipTwo.

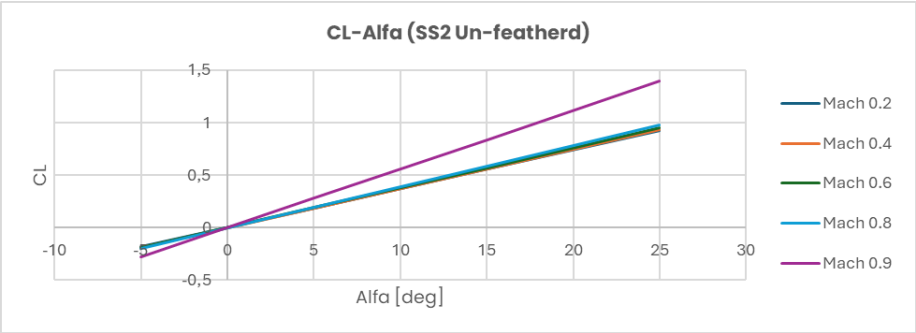

Figure 4.9: Result for lift coefficient as a function of Mach number and angle of attack in subsonic and transonic regime with Raymer model

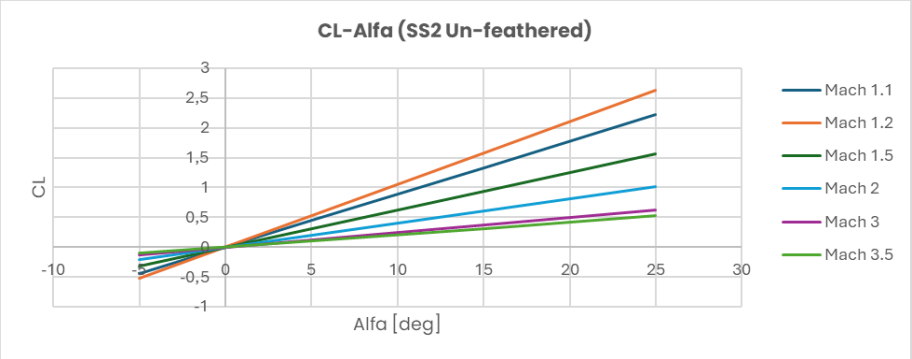

Figure 1.10: Result for lift coefficient as a function of Mach number and angle of attack in transonic and supersonic regime with Raymer model

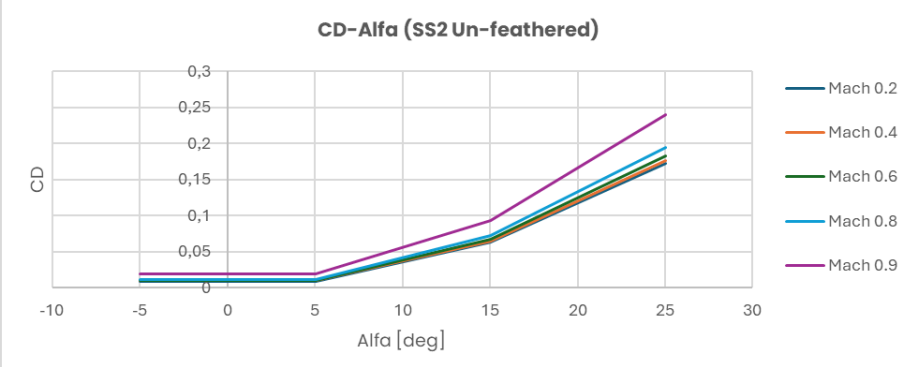

Figure 4.11: Result for drag coefficient as a function of Mach number and angle of attack in subsonic and transonic regime with Raymer model

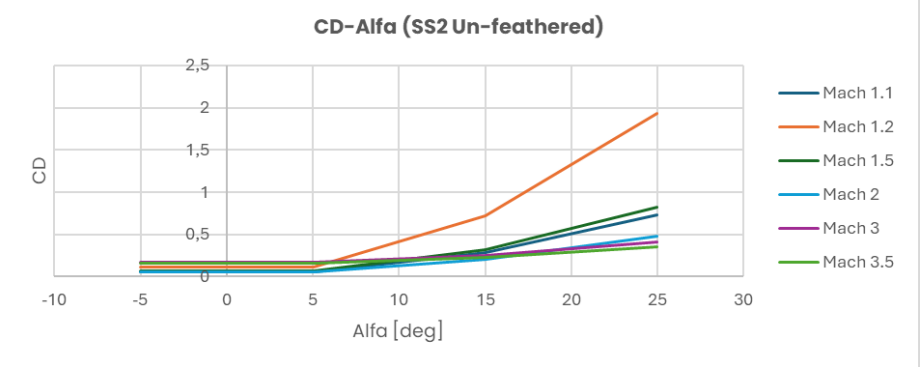

Figure 4.12: Result for drag coefficient as a function of Mach number and angle of attack in transonic and supersonic regime with Raymer model

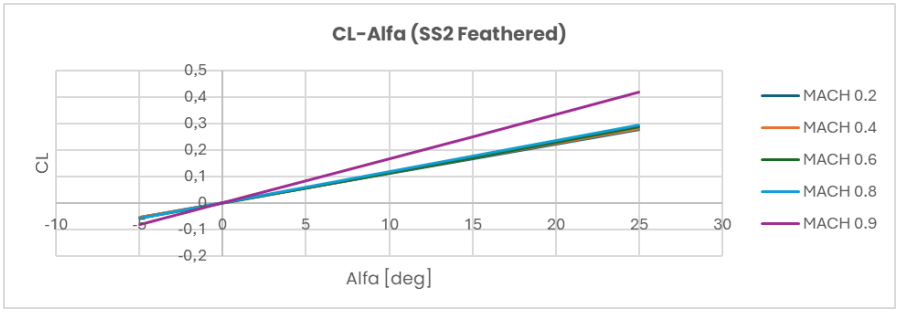

Figure 4.13: Result for lift coefficient as a function of Mach number and angle of attack in subsonic and transonic regime with Raymer model

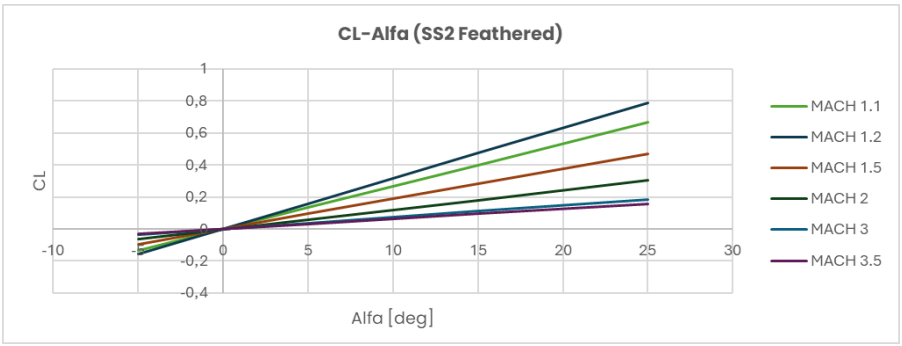

Figure 4.14: Result for lift coefficient as a function of Mach number and angle of attack in transonic and supersonic regime with Raymer model

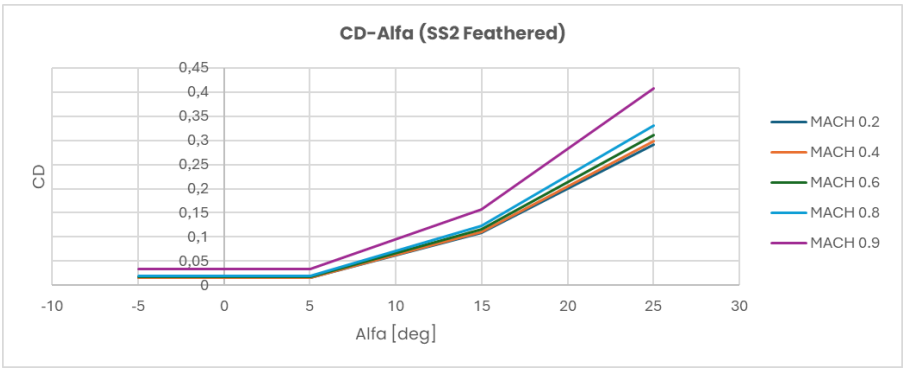

Figure 4.15: Result for drag coefficient as a function of Mach number and angle of attack in subsonic and transonic regime with Raymer model

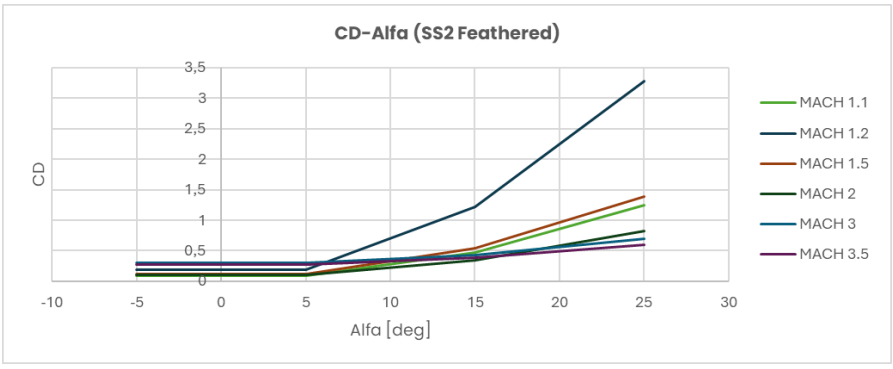

Figure 4.16: Result for drag coefficient as a function of Mach number and angle of attack in transonic and supersonic regime with Raymer model

4.2.4 Carrier Standalone Configuration result

The Figures (4.17) and (4.18) illustrate the findings of the aerodynamic analyses conducted using the Raymer model for the WhiteKnightTwo aircraft in the standalone configuration. A comparison of the graphs obtained using Raymer's method with the mated configuration reveals that, while the lift coefficient remains approximately unchanged, the drag coefficient is lower than in the mated case, due to the absence of the drag contribution resulting from the presence of the SpaceShipTwo.

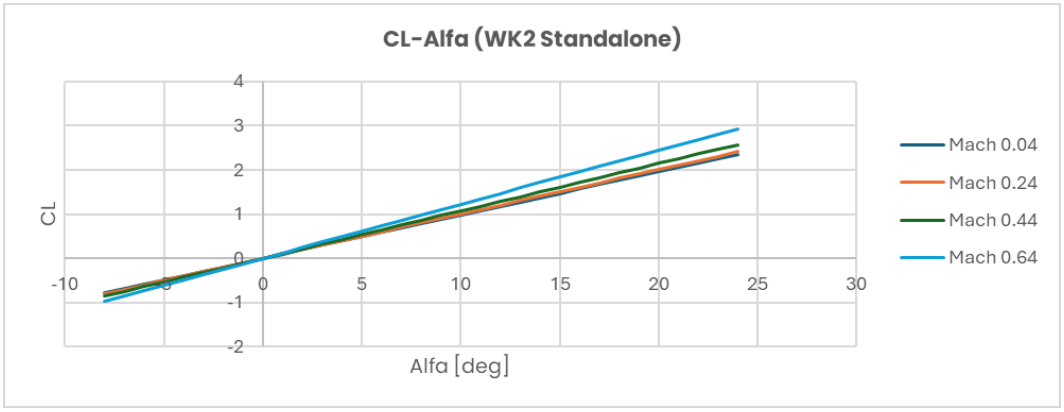

Figure 4.17: Result for lift coefficient as a function of Mach number and angle of attack from Raymer Model

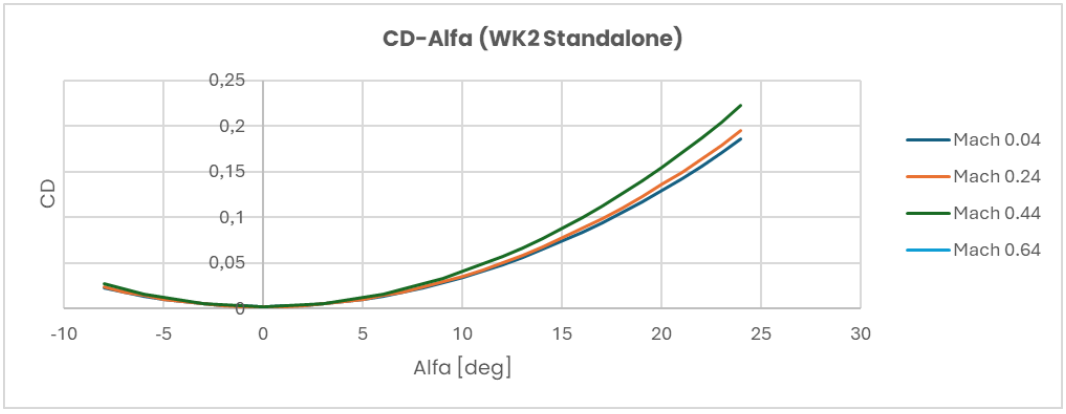

Figure 4.18: Result for drag coefficient as a function of Mach number and angle of attack from Raymer Model

4.3 Propulsive results

Regarding the propulsive characterisation of the separate-flow turbofan engine mounted on the WhiteKnightTwo, preliminary databases on thrust and specific thrust consumption as a function of flight altitude, flight Mach number and throttle were obtained. The Figures (4.19) and (4.20) illustrate the trend of the thrust value and the specific thrust fuel consumption (TSFC) for a given value of Mach number as the flight altitude varies. The curves are parameterised with the throttle setting. Table [4.2] illustrates the principal characteristics of the RocketMotorTwo in its configuration on the SpaceShipTwo. In this instance, generating a propulsive database was not a requisite step, as this is not a requirement of the programme for trajectory simulations.

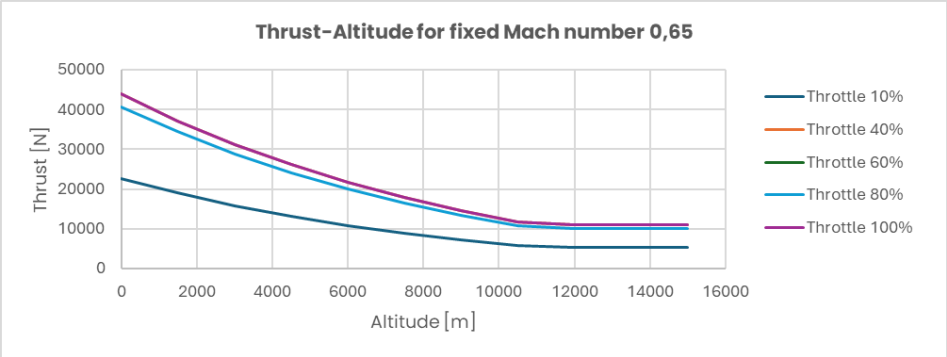

Figure 4.19: Preliminary results for the thrust at different throttle settings and at different altitudes for a fixed value of the Mach number for PW308A engine

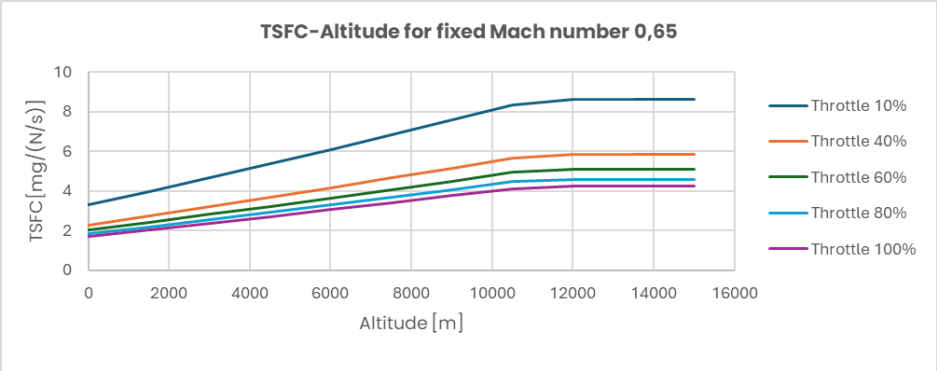

Figure 4.20: Preliminary results for the TSFC at different throttle settings and at different altitudes for a fixed value of the Mach number for PW308A engine

Parameter	Value	M.U.
Rocket thrust	50000 to 85000	pounds
Specific impulse	250	s
Burn time	60	s
Max Launch weight	13154	Kg
Max fuel capacity	7031	kg

Table 4.2: Main characteristics of the RocketMotorTwo

4.4 Mission Profile results

4.4.1 ASTOS simulations results

4.4.1.1 Nominal scenario with release in the direction of Taranto

The initial route implemented on the ASTOS software is that relative to a nominal scenario for SpaceShipTwo mission, which anticipates the release phase occurring in the direction of Taranto. Figure (4.21) shows the two-dimensional georeferenced trajectory pertaining to the SpaceShipTwo mission. Additionally, the georeferenced trajectory is represented on the three-dimensional plane in Figure (4.22), and the flight Mach, altitude, and angle of attack trends over time are illustrated in Figure (4.23). As outlined in Chapter 3.4, this trajectory option was modelled to validate aircraft data in glide phases up to landing. Its similarity in phase duration and distance travelled by SpaceShipTwo renders it a useful case study.

Figures (4.24) and (4.25) illustrate the comparison between the altitude profile and Mach number over time obtained from the ASTOS simulation and the data for the VGX2 and VGX3 flights. From the comparison of the curves, it can be observed that:

- The simulated flight profile has a slightly shorter duration (68.52 minutes) than the real profile followed during the mission (71.41 minutes);
- The peak altitude reached with the simulation is 87.3 km compared to the 88 km reached during the aircraft's mission;
- In the early stages of flight until release, the speed profile obtained with ASTOS follows higher speeds than those obtained by FlightAware but never exceeds the maximum Mach at which the carrier aircraft can fly.

Given these clarifications, the flight profile obtained with ASTOS can be considered valid.
Figures (4.26), (4.27) and (4.28) pertain to the mission undertaken by the WhiteKnightTwo aircraft in a standalone configuration immediately following the release of the SpaceShipTwo. The images do not illustrate the initial phase of the mission, which occurs when the aircraft is in a mated configuration. This is because the simulation for the preceding phases, up to and including the release, is identical to that which has just been observed for SpaceShipTwo. As illustrated, the carrier aircraft initiates a turn immediately following the release of the spaceplane, thereby maintaining the requisite distance between the two aircraft in the subsequent phases. A review of the aircraft's previous missions revealed that a mean interval of 50 minutes elapsed between the release phase and the landing of the carrier aircraft. This data was employed in the simulations.

Figures (4.29) and (4.30) illustrate the comparison between the flight profile of WhiteKnightTwo obtained through simulations and that of the flight conducted on 26 January 2024. From the comparison, it can be seen that in terms of altitude, the trend obtained with the ASTOS simulations is similar to that of the VGX2 flight. However, in terms of Mach number, there is a different trend, as during the mission carried out by the aircraft during the descent phases, there is a strong oscillation in speed. This is due to the type of trajectory adopted. Indeed, the ASTOS simulations considered a trajectory analogous to that depicted in Figure (4.26), given the spatial constraints of the mission and the demographic analysis of the surrounding area. Conversely, the actual mission saw the aircraft descend in a spiral trajectory, with a series of turns until landing.

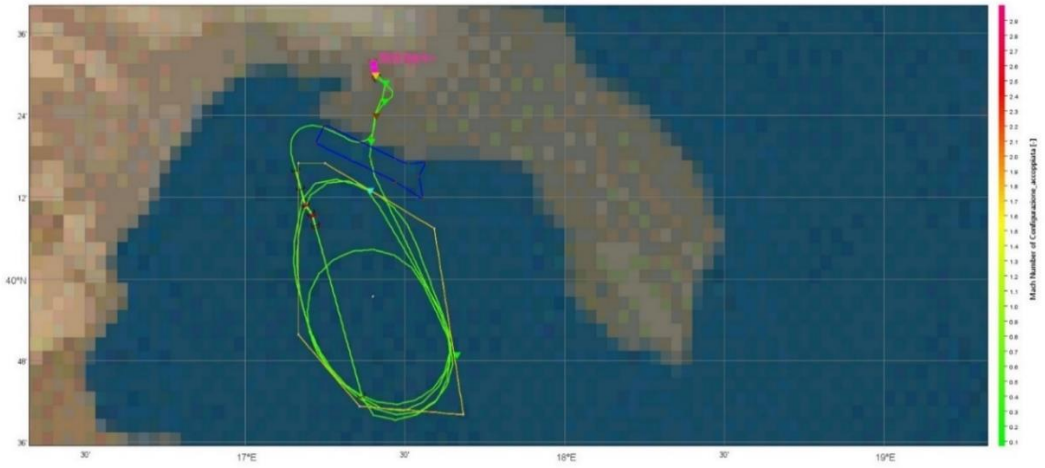

Figure 4.21: ASTOS result for complete trajectory for SpaceShipTwo on the 2D map for the mission scenario with release phase directed towards Taranto

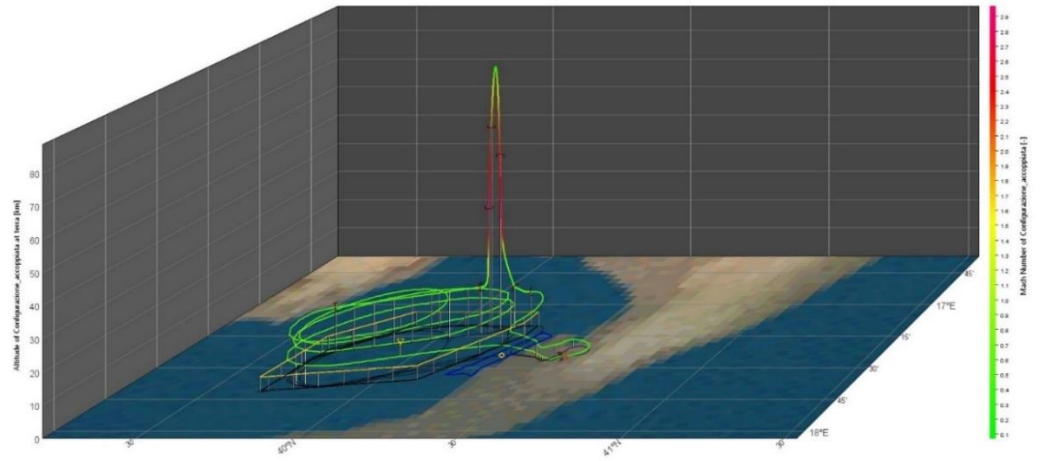

Figure 4.22: ASTOS result for complete trajectory for SpaceShipTwo on the 3D map for the mission scenario with release phase directed towards Taranto

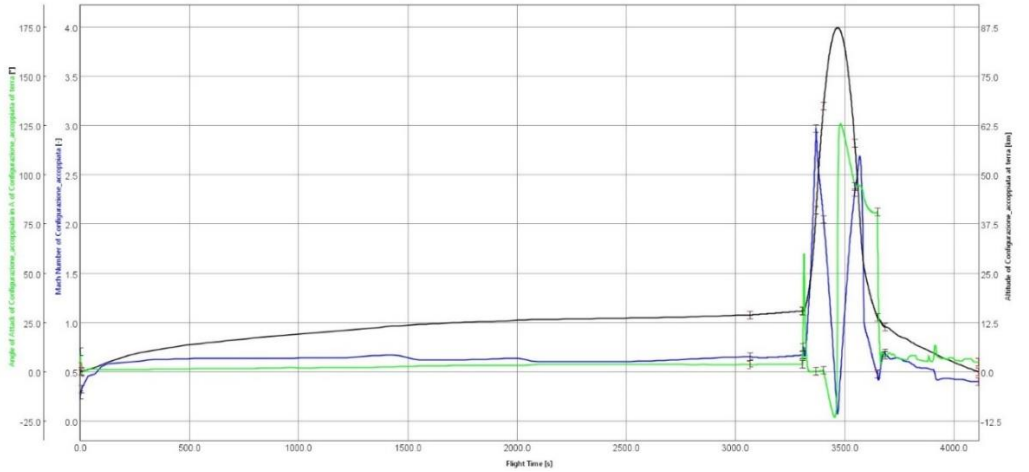

Figure 4.23: ASTOS output for Mach, altitude and angle of attack profiles over time for the SpaceShipTwo mission scenario, with the release phase directed towards Taranto

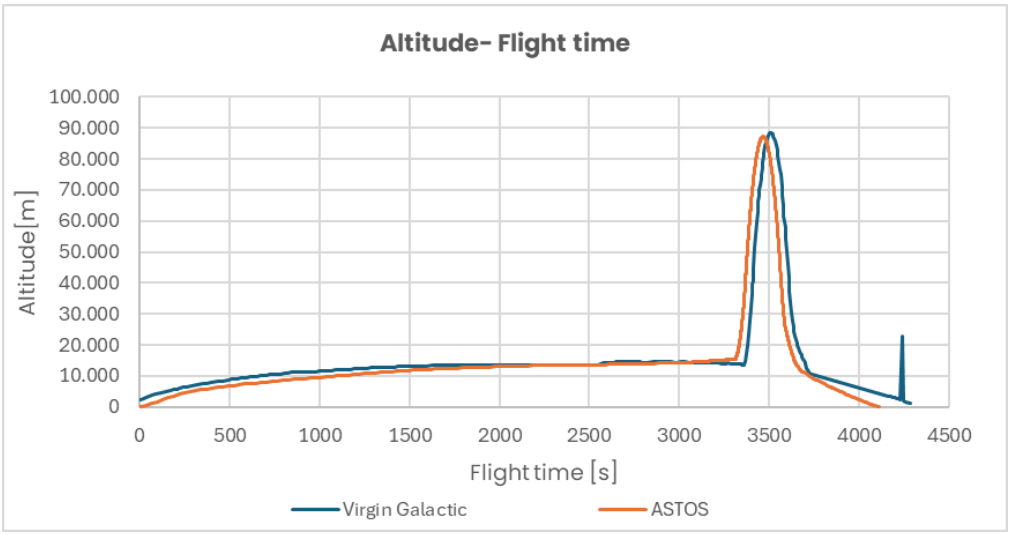

Figure 4.24: Altitude profile comparison between the ASTOS simulation result for the nominal SpaceShipTwo scenario with release phase in the Taranto direction and data from literature [21] [22]

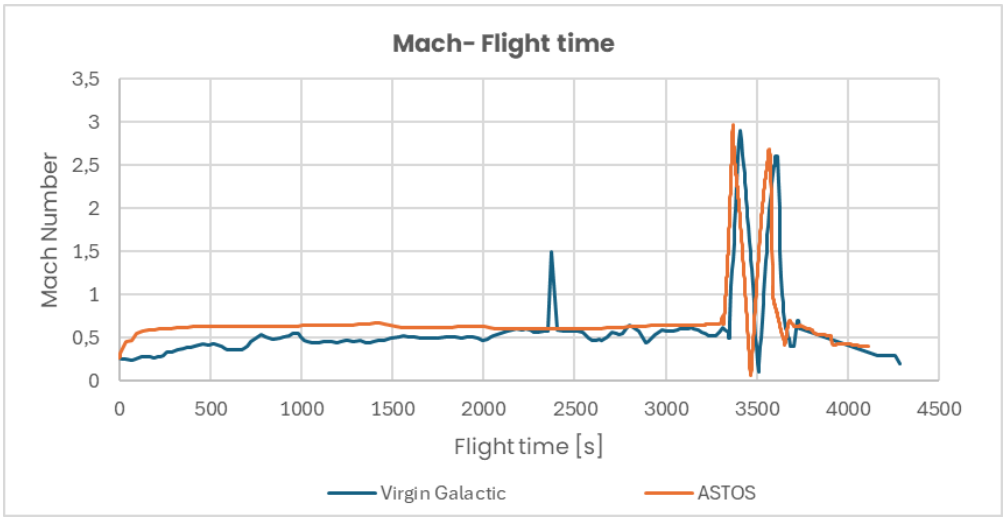

Figure 4.25: Mach profile comparison between the ASTOS simulation result for the nominal SpaceShipTwo scenario with release phase in the Taranto direction and data from literature [21] [22]

Figure 4.26: ASTOS output for the trajectory related to the descent and landing phases of WhiteKnightTwo depicted on the 2D map for the mission scenario with the release phase directed towards Taranto

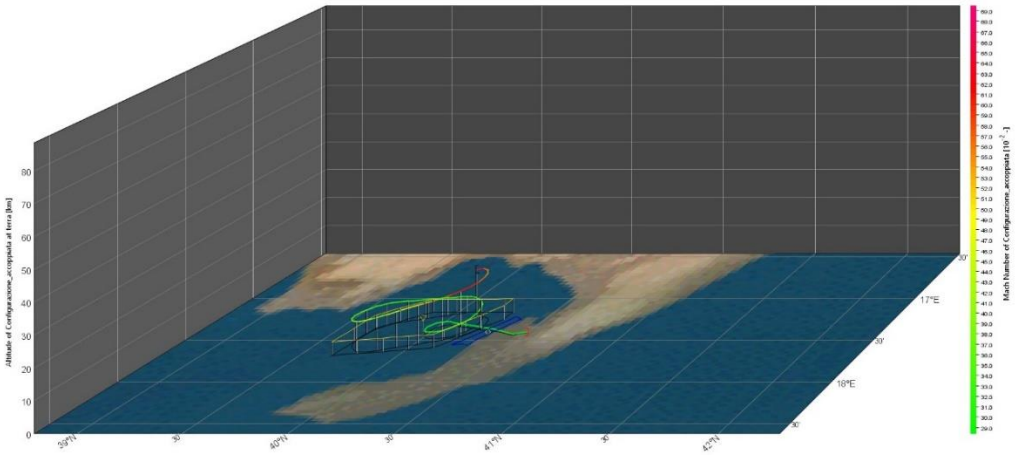

Figure 4.27: ASTOS output for the trajectory related to the descent and landing phases of WhiteKnightTwo depicted on the 3D map for the mission scenario with the release phase directed towards Taranto

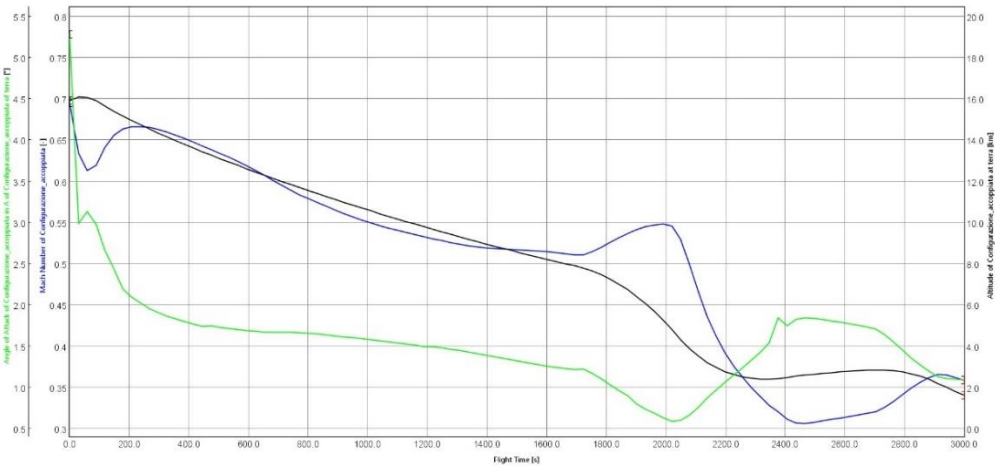

Figure 4.28: ASTOS output for Mach, altitude and angle of attack profiles over time for the WhiteKnightTwo descent and landing phases in the mission scenario with the release phase directed towards Taranto

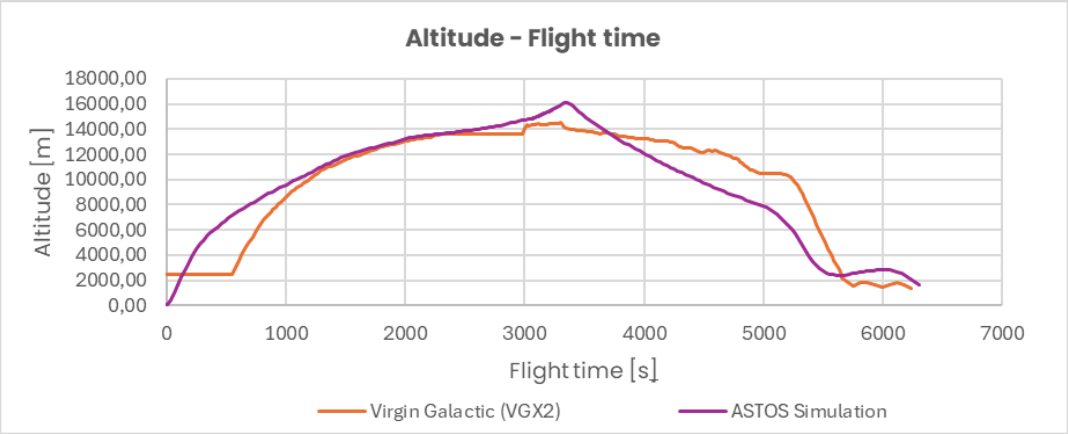

Figure 4.29: Altitude profile comparison between the ASTOS simulation result for the nominal WhiteKnightTwo scenario with release phase in the Taranto direction and data from literature [20]

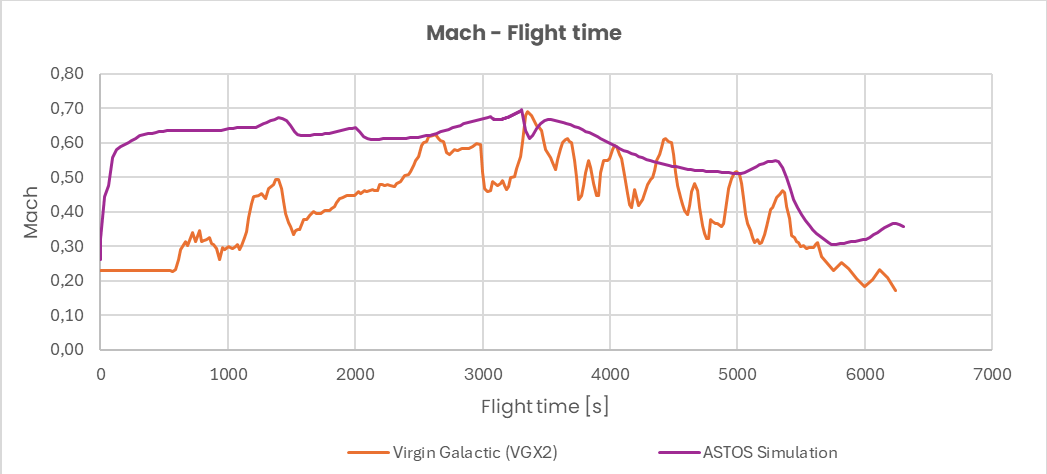

Figure 4.30: Mach profile comparison between the ASTOS simulation result for the nominal WhiteKnightTwo scenario with release phase in the Taranto direction and data from literature [20]

4.4.1.2 Nominal scenario with release in the direction of Ionian Sea

The second nominal scenario, simulated on ASTOS for the two aircraft, depicts a spaceplane release phase occurring in the direction of the Ionian Sea. Figure (4.31) illustrates the georeferenced route in two dimensions, whereas Figure (4.32) depicts the same route in three dimensions and provides altitude data. Figure (4.33) illustrates the aircraft's performance throughout the mission, showcasing altitude, flight Mach, and angle of attack data. As illustrated in Figures (4.34) and (4.35), the glide phase of the mission lasts approximately four minutes longer than the recent real-world mission. This temporal discrepancy is also evident in the comparison between the two simulations, one in the direction of Taranto and the other in the direction of the Ionian Sea. This is attributed to the differing positions of the points within the R405 zone where the spaceplane is situated.

Figures (4.34) and (4.35), illustrate that while the altitude and speed profiles over time remain similar, they are not identical to those provided by FlightAware data. In this instance, the initial phases of the mission exhibit comparable characteristics to those observed in the simulation of the trajectory with release in the direction of Taranto. The principal discrepancy between the two simulations is evident in the glide phase, whereby the aircraft is required to undertake a distinct and extended trajectory in order to return to the departure airport.

In addition, the trajectory to be followed by the carrier aircraft following the release of the spaceplane was also simulated for this mission. The georeferenced route in a 2D and 3D map, respectively, that the WhiteKnightTwo will have to follow during its descent is illustrated in Figures (4.36) and (4.37). Figure (4.38) illustrates the aircraft's performance throughout the mission, showcasing altitude, flight Mach, and angle of attack data. As in the preceding nominal scenario, the carrier aircraft following the release of the SpaceShipTwo makes a turn that allows it to deviate from the trajectory followed by the spaceplane.

A comparative analysis of the data in Figures (4.39) and (4.40) about the mission involving the WhiteKnightTwo reveals that the aircraft exhibits a greater descent rate during the initial phase of the descent than that observed in the VGX2 mission.

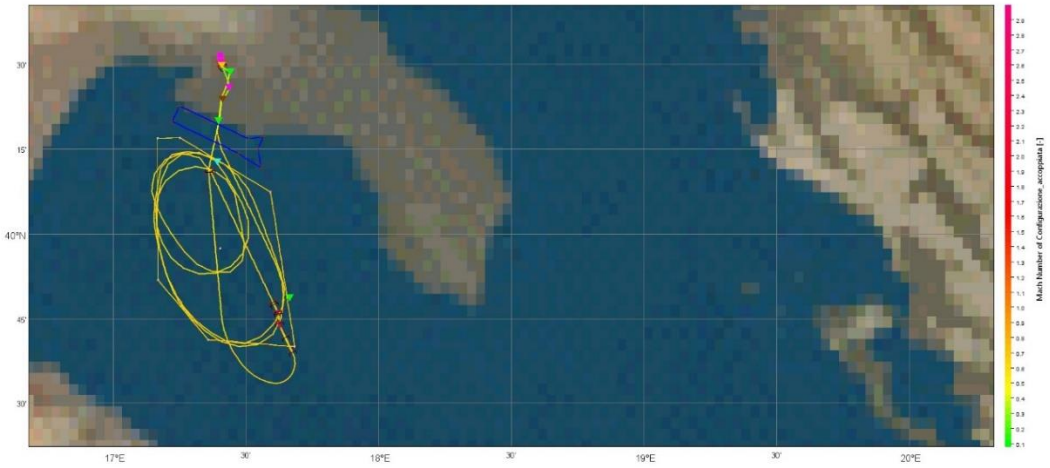

Figure 4.31: ASTOS result for complete trajectory for SpaceShipTwo on the 2D map for the mission scenario with release phase directed towards Ionian Sea

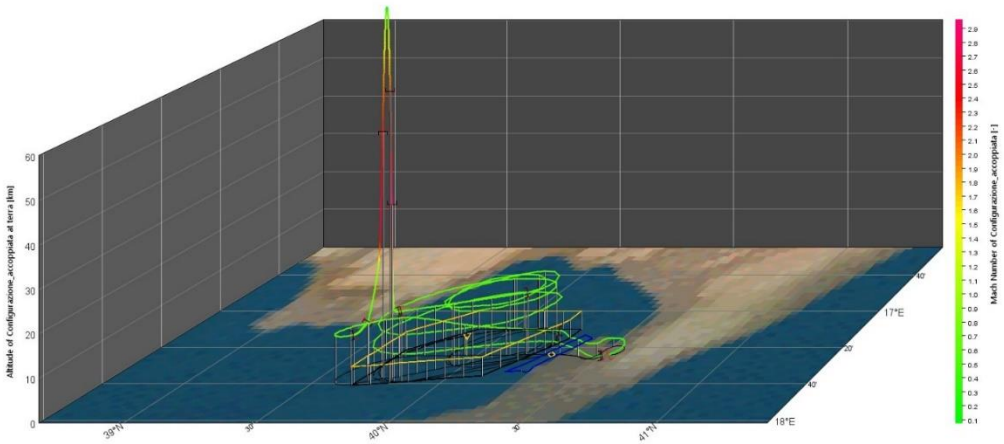

Figure 4.32: ASTOS result for complete trajectory for SpaceShipTwo on the 3D map for the mission scenario with release phase directed towards Ionian Sea

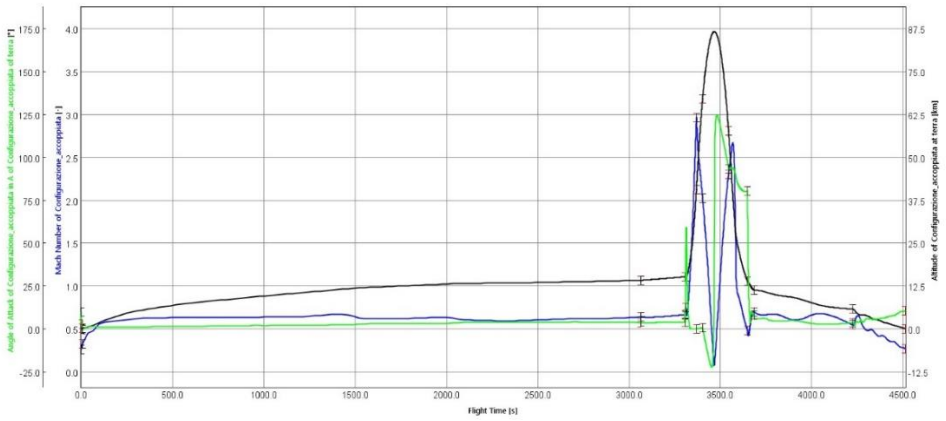

Figure 4.33: ASTOS output for Mach, altitude and angle of attack profiles over time for the SpaceShipTwo mission scenario, with the release phase directed towards Ionian Sea

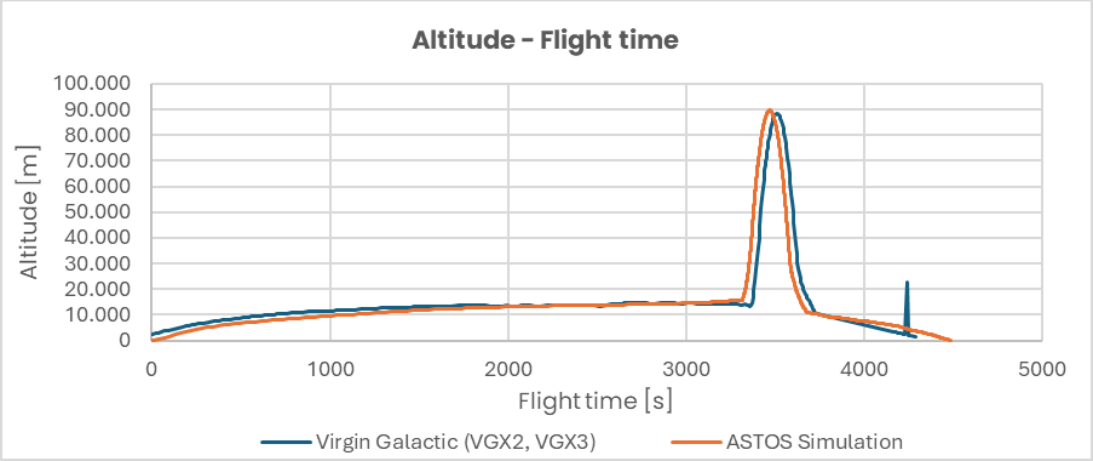

Figure 4.34: Altitude profile comparison between the ASTOS simulation result for the nominal SpaceShipTwo scenario with release phase in the Ionian Sea direction and data from literature [21] [22]

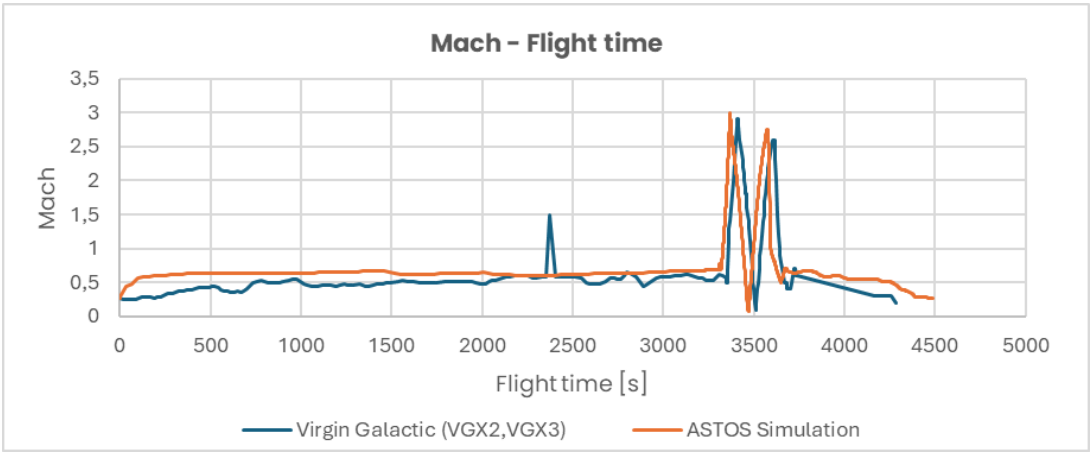

Figure 4.35: Mach profile comparison between the ASTOS simulation result for the nominal SpaceShipTwo scenario with release phase in the Ionian Sea direction and data from literature [21] [22]

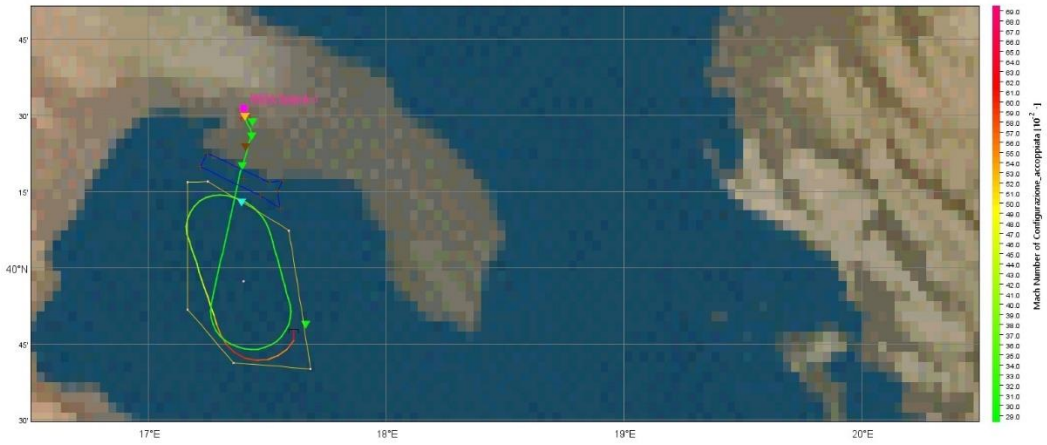

Figure 4.36: ASTOS output for the trajectory related to the descent and landing phases of WhiteKnightTwo depicted on the 2D map for the mission scenario with the release phase directed towards Ionian Sea

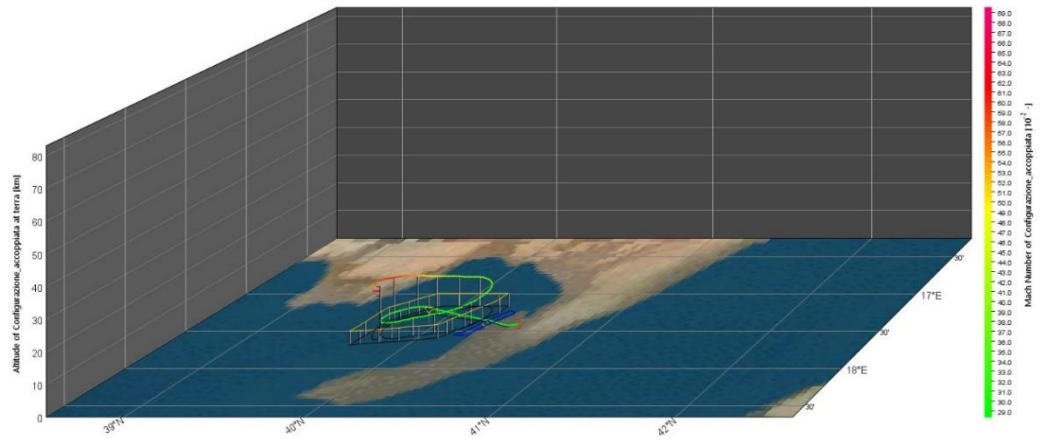

Figure 4.37: ASTOS output for the trajectory related to the descent and landing phases of WhiteKnightTwo depicted on the 3D map for the mission scenario with the release phase directed towards Ionian Sea

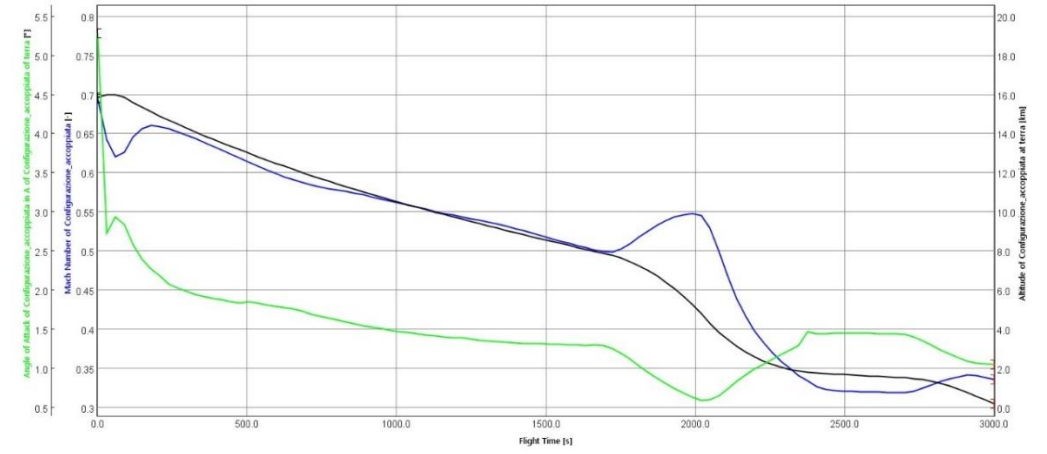

Figure 4.38: ASTOS output for Mach, altitude and angle of attack profiles over time for the WhiteKnightTwo descent and landing phases in the mission scenario with the release phase directed towards Ionian Sea

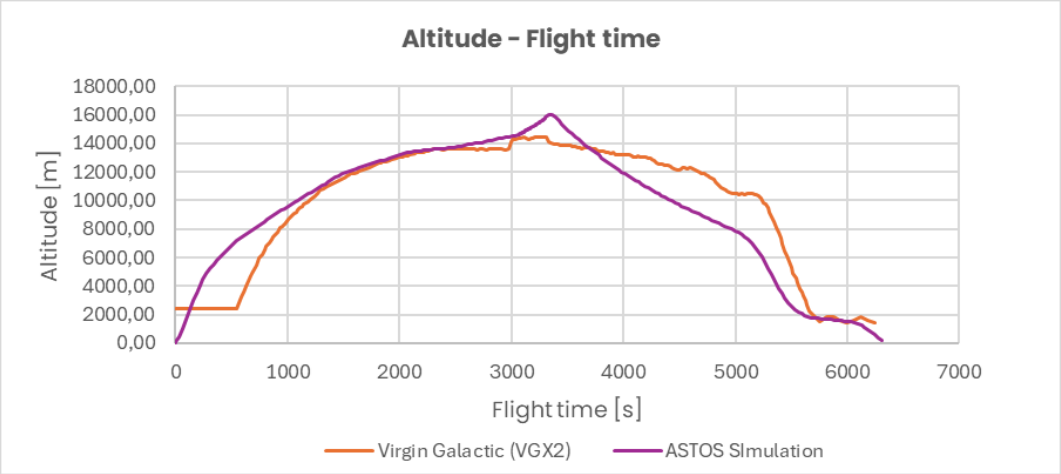

Figure 4.39: Altitude profile comparison between the ASTOS simulation result for the nominal WhiteKnightTwo scenario with release phase in the Ionia Sea direction and data from literature [20]

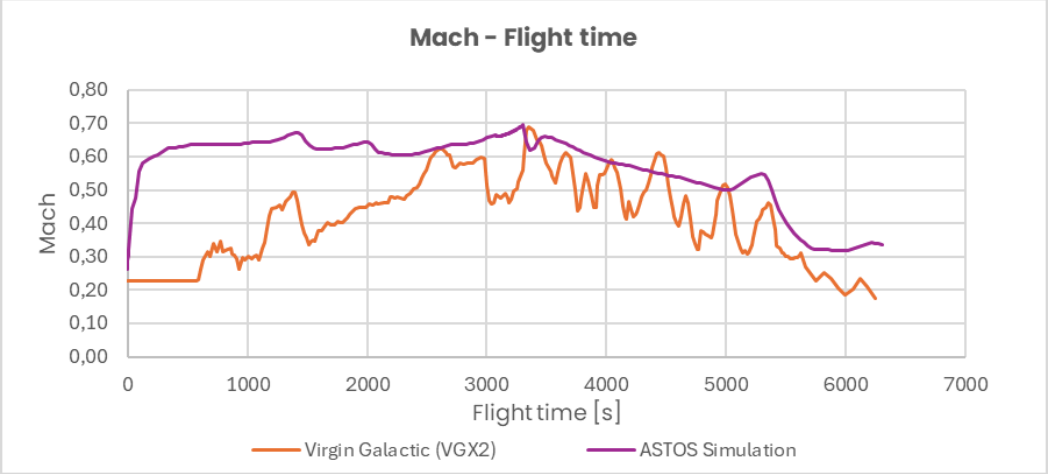

Figure 4.40: Mach profile comparison between the ASTOS simulation result for the nominal WhiteKnightTwo scenario with release phase in the Ionia Sea direction and data from literature [20]

4.4.2 QGIS Visualizations

The results of the simulations performed on ASTOS were imported into the QGIS software as geographical coordinates (latitude and longitude) to verify that, during the nominal mission scenario, the two aircraft do not fly over densely populated areas.

4.4.2.1 Mission with release in the direction of Taranto

Figure (4.41) illustrates the take-off and the initial stages of the aircraft's climb in a mated configuration. Figure (4.42) illustrates the concluding phase of the descent trajectory undertaken by the SpaceShipTwo in its un-feathered configuration. Figure (4.43) illustrates the concluding phase of the descent trajectory undertaken by the carrier aircraft when operating in a standalone configuration. It is evident that throughout all three phases of the mission, there is no overflying of densely populated areas.

4.4.2.2 Mission with release in the direction of the Ionian Sea

Figure (4.44) illustrates the take-off and the initial stages of the aircraft's climb in a mated configuration. Figure (4.45) illustrates the concluding phase of the descent trajectory undertaken by the SpaceShipTwo in its un-feathered configuration. Figure (4.46) illustrates the concluding phase of the descent trajectory undertaken by the carrier aircraft when operating in a standalone configuration. It is evident that throughout all three phases of the mission, there is no overflying of densely populated areas.

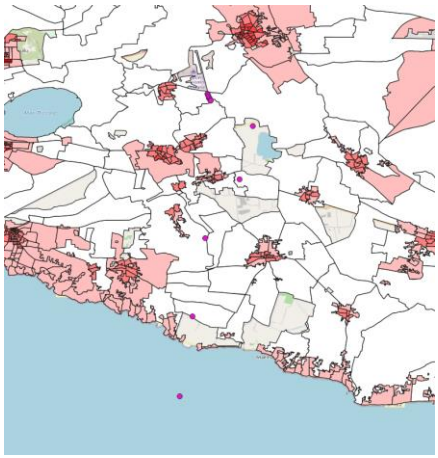

Figure 4.41: Magnified view of the corridor followed by the aircraft in mated configuration after take-off for the mission with release phase in the direction of Taranto depicted on a map showing population density distribution in Puglia

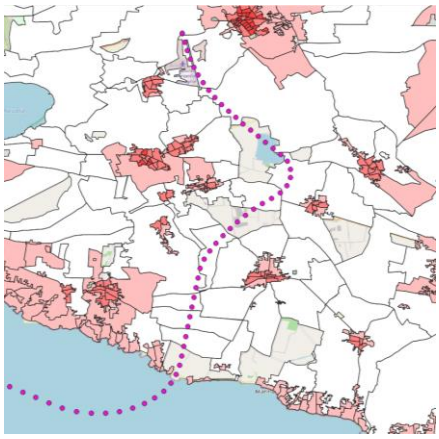

Figure 4.42: Magnified view of the corridor followed by the SpaceShipTwo in un-feathered configuration before land for the mission with release phase in the direction of Taranto depicted on a map showing population density distribution in Puglia

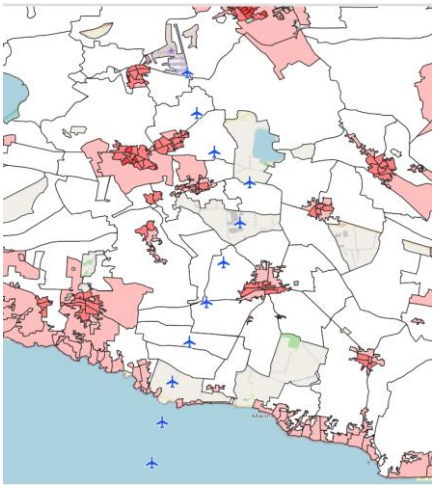

Figure 4.43: Magnified view of the corridor followed by the carrier Standalone configuration before land for the mission with release phase in the direction of Taranto depicted on a map showing population density distribution in Puglia

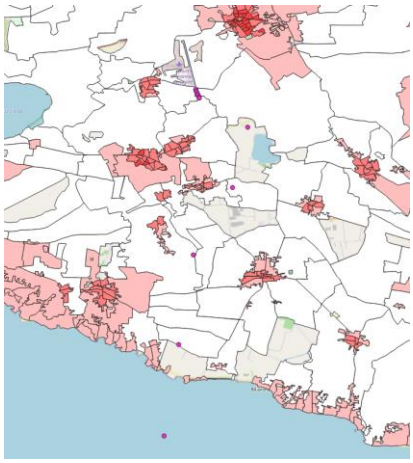

Figure 4.44: Magnified view of the corridor followed by the aircraft in mated configuration after take-off for the mission with release phase in the direction of Ionian Sea depicted on a map showing population density distribution in Puglia

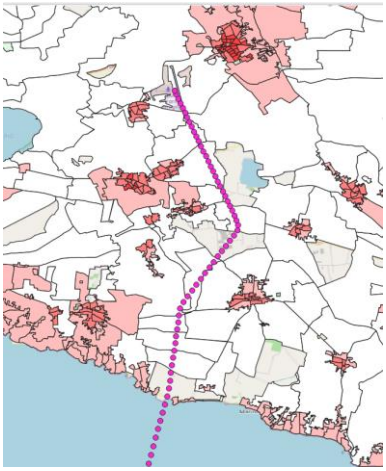

Figure 4.45: Magnified view of the corridor followed by the SpaceShipTwo in un-feathered configuration before land for the mission with release phase in the direction of Ionian Sea depicted on a map showing population density distribution in Puglia

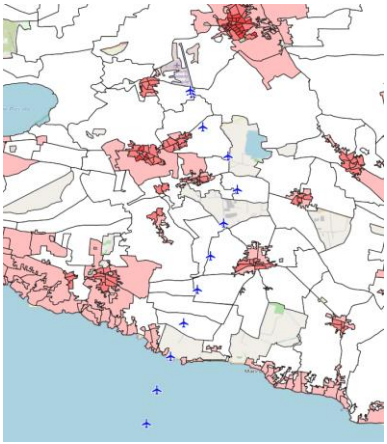

Figure 4.46: Magnified view of the corridor followed by the carrier Standalone configuration before land for the mission with release phase in the direction of Ionian Sea depicted on a map showing population density distribution in Puglia

Chapter 5

Conclusions

This study aims to conduct a preliminary investigation into the potential for future suborbital vehicle system operations on Italian territory. The Grottaglie Airport in Puglia was selected as a case study.

Trajectory simulations using ASTOS software were necessary to define a potential flight path for the A-to-A mission for a suborbital vehicle system. The results of these simulations may support ENAC's assessment and research activities.

A study of the mission and the aircraft involved, specifically the WhiteKnightTwo and the SpaceShipTwo, revealed four configurations the aircraft would adopt throughout the mission. These were i) mated configuration; ii) standalone configuration; iii) un-feathered configuration of the spaceplane; iv) and feathered configuration.

Once the configurations were known and the geometric data for each was found and calculated, an aerodynamic analysis was carried out using the Raymer model. This provided the preliminary aerodynamic databases, expressed in terms of lift coefficient and drag as a function of flight Mach, altitude and angle of attack, for the four configurations. A preliminary propulsive characterisation was conducted for the engines powering the WhiteKnightTwo, specifically the separate-flow turbofan, PW308A, and the RocketMotorTwo mounted on the SpaceShipTwo. As previously stated, the databases obtained through semi-empirical mathematical models do not accurately represent reality. Indeed, these databases were employed in the initial simulations and yielded satisfactory results. However, in subsequent simulations, they will be supplanted by more precise data obtained through sophisticated techniques such as computational fluid dynamics (CFD) simulations and the utilisation of software for engine performance estimation.

Regarding the identification of the trajectory, in order to limit the impact on the airspace affected by the operation, only areas R315, R316, R317, R405/B, R405/D, TSA455A and TSA455B were considered in the preliminary analysis. This approach inevitably constrained the scope for trajectory development, and it was not feasible to accurately replicate the trajectory already traversed during the FlightAware mission. Indeed, an analysis was conducted on the trajectory flown during the VGX2 and VGX3 missions to gain insight into the general trend regarding altitude, speed and course followed. After these analyses, a spiral trajectory analogous to the VGX2 flight was simulated for the ascent phase in the mated configuration. Nevertheless, a notable discrepancy exists between the results mentioned above and those obtained from the mission conducted at Spaceport America in New Mexico (USA), where a considerably larger area was accessible. Consequently, the straight sections traversed during the ascent possess a markedly greater length than that available within the R405 area utilized for the simulations.

The initial simulations were conducted using the ASTOS software and the aforementioned databases. The initial scenario, which postulates the deployment of a spaceplane in the direction of Taranto, provided crucial validation of the results. In this case, the suborbital mission conducted by SpaceShipTwo ends in an un-feathered re-entry phase in the proximity of the Grottaglie Airport. Consequently, at the outset of the glide phase, the temporal and spatial distances from the airport are approximately equivalent to those observed during the VGX3 mission. In contrast, the descent and landing phase of the WhiteKnightTwo aircraft yielded results regarding flight speed that were similar to those of the VGX2 mission. However, this is because, during the descent, the aircraft makes a series of consecutive turns near the airport. This is possible

given the geographical positioning of Spaceport America. In the simulations, a different trajectory was assumed, following the analyses carried out on the population density near the Grottaglie Airport. The second simulated mission scenario entails the deployment of the spaceplane in a directional trajectory towards the Ionian Sea. In this instance, the considerations mentioned above about the ascent phase in mated configuration and the descent phase of WhiteKnightTwo remain applicable. In contrast to the mission scenario involving a release in the direction of Taranto, the release and subsequent phases relating to SpaceShipTwo are conducted at a suitable distance from the Earth and in the opposite direction. For these reasons, this trajectory is expected to be a possible better choice in terms of safety, as it better allows for the continued protection of individuals on the ground in the event of an emergency or catastrophic occurrence.

The results obtained from the simulations were then entered into the QGIS software to verify that the flight corridors traversed by the aircraft after take-off and before landing do not traverse densely populated areas.

The results obtained through this study can be considered preliminary and, as such, may require further improvement in order to increase their reliability and accuracy.

Chapter 6

Future work

The study, which formed part of my thesis work, requires further improvement to enhance the accuracy and reliability of the results.

In particular, the aerodynamic and propulsive characterisation of the aircraft must be considered initially, with the aerodynamic databases obtained for the four configurations to be verified and possibly improved. This may be achieved by developing a CAD model of the two aircraft, which will then be employed to conduct aerodynamic analyses utilising computational fluid dynamics (CFD) simulation. A comparison of the results obtained with the Raymer model and those obtained with CFD simulations will facilitate the improvement of the aerodynamic databases.

Regarding the propulsive aspect, it will be essential to conduct a more comprehensive analysis of the preliminary results obtained through the Mattingly theory. These data will then be enhanced by comparing them with the results that can be derived from more sophisticated engine analysis software, such as GSP.

Regarding the mission profile additional areas may be designated for the mission to be conducted. These areas must be situated over the sea and be of sufficient size to emulate a trajectory more analogous to that previously traversed by the aircraft during previous missions.

Once the preliminary nominal scenario has been enhanced in accuracy and reliability, analyses can be conducted on out-of-nominal mission scenarios. In such cases, an alternative trajectory can be defined for the two aircraft to follow, and an alternative airport may also be identified based on the planar space's performance and the ground infrastructure's characteristics.

Acknowledgements

I would like to thank Professors Nicole Viola and Roberta Fusaro for giving me the opportunity to start and develop a thesis project that reflects my personal interests and for the trust they have shown in me along the way.

I would like to extend my gratitude to Ing. Giovanni di Antonio Innovation Technology Director at ENAC, Ing. Fabrizio Arru, and Ing. Alessandro Bucci for offering me the invaluable opportunity to undertake my thesis in collaboration with ENAC and their continued support throughout this research work.

Furthermore, I would like to express my gratitude to Oscar Gori, PhD student in the Department of Mechanical and Aerospace Engineering, for his helpfulness, close cooperation and commitment to the success of this research.

Bibliography

[1] ENAC, *Suborbital and Access to Space Operations (SASO) Regulation,* 2023.

[2] NTSB, «Investigation of Scaled Composites, LLC's SpaceShipTwo, N339SS, Rocket-Powered Flight Test, Koehn Dry Lake, California, October 31, 2014,» 2015.

[3] FAA, «Final Environmental Assessment for the Launch and Reentry of SpaceShipTwo Reusable Suborbital Rockets at the Mojave Air and Space Port,» 2012.

[4] A. ". A. d. T. Grottaglie, «Piano di Sviluppo Aeroportuale 2030,» 2017.

[5] «Lo spazioporto nascerà in Puglia,» *ASI-Agenzia Spaziale Italiana,* 2018.

[6] ENAC, *Regolamento per la costruzione e l'esercizio degli spazioporti,* 2023.

[7] D. P. Raymer, Aircraft Design: A Conceptual Approach, Sixth Edition.

[8] J. John D. Anderson, Aircraft Performance and Design.

[9] «Public Domain Aeronautical Software (PDAS),» 2022. [Online]. Available: https://www.pdas.com/datcomDescription.html.

[10] «Astos Solutions,» [Online]. Available: https://www.astos.de/products/astos.

[11] «QGIS,» [Online]. Available: https://qgis.org/project/overview/.

[12] «Istituto Nazionale di Statistica,» [Online]. Available: https://www.istat.it/.

[13] V. Galactic, «Spaceport America,» 2020. [Online]. Available: https://spaceportamerica.com/wp-content/uploads/2020/10/WK2-Data-Brochure-VG.pdf.

[14] V. Galactic, «Virgin Galactic Space Vehicles Fact Sheet,» 2011.

[15] E. (. U. A. S. Agency), «Type-Certificate Data Sheet, EASA.IM.E.057 for PW308 Series engines,» 2023.

[16] A. Deng, *Aerodynamic Performance Prediction of SpaceShipTwo,* 2012.

[17] C. Weiland, Aerodynamic Data of Space Vehicles, 2014.

[18] ICAO, «ICAO Aircraft Engine Emission Databank,» [Online]. Available: https://www.easa.europa.eu/en/domains/environment/icao-aircraft-engine-emissions-databank.

[19] «FlightAware,» [Online]. Available: https://www.flightaware.com/.

[20] «FlightAware, Virgin Galactic 2,» [Online]. Available: https://it.flightaware.com/live/flight/VGX2.

[21] «FlightAware, Virgin Galactic 3,» [Online]. Available: https://it.flightaware.com/live/flight/VGX3.

[22] V. Galactic, *LIVE: Watch the #Galactic02 Spaceflight.*

[23] A. d. Puglia, «AEROPORTO CIVILE DI TARANTO/Grottaglie».

[24] ENAC, «Regole dell'aria Italia,» 2021.